

@ 2021

SEYED AMIN NABAVIZADEH

ALL RIGHTS RESERVED

EFFECT OF MARANGONI CONVECTION ON DENDRITIC SOLIDIFICATION

A Dissertation

Presented to

The Graduate Faculty of The University of Akron

In Partial Fulfillment

of the Requirements for the Degree

Doctor of Philosophy

Department of Mechanical Engineering

Seyed Amin Nabavizadeh

December 2021

EFFECT OF MARANGONI CONVECTION ON DENDRITIC SOLIDIFICATION

Seyed Amin Nabavizadeh

Dissertation

Approved:

Accepted:

Advisor
Dr. Sergio D. Felicelli

Department Chair
Dr. Sergio D. Felicelli

Committee Member
Dr. Mohsen Eshraghi

Interim Dean of the College
Dr. Craig Menzemer

Committee Member
Dr. Minel Braun

Interim Director, Graduate School
Dr. Marnie Sanders

Committee Member
Dr. Craig Menzemer

Date

Committee Member
Dr. Lingxing Yao

ABSTRACT

It has been amply shown that porosity defects can degrade the mechanical properties of solidified alloys. In particular, the presence of large pores or bubbles in the melt during solidification can cause fluid flow along the bubble-melt interface due to surface tension gradients. This flow can distort the direction of dendrite growth and produce defects such as microsegregation between grain boundaries. In addition, the flow is responsible for the fragmentation of dendrite side-arms and their rotation, creating nuclei for spurious grain formation. Therefore, understanding the consequences of the presence of bubbles on microstructural evolution during alloy solidification can provide helpful information to enhance the microstructure and properties of solidified materials.

In this dissertation, computational models are developed to study various phenomena during the solidification of binary alloys under microgravity conditions focusing on Marangoni convection. The problem is tackled by solving continuity, fluid flow, energy, and solute transport equations, and implementing models to simulate the interface between solid and liquid and gas. The cellular automaton (CA) and Allen-Cahn Phase Field (PF) models were utilized to track the solid/liquid interface while lattice Boltzmann (LB) and finite difference (FD) models were applied for solute transport equation. FD method and frozen temperature approximation were implemented for energy equation. Different types of the lattice Boltzmann multiphase flow models were tested to recover continuity and fluid flow equations. The models include Shan-Chen

based, and Cahn–Hilliard (CH)-PF based LB. To increase the computational speed of these models for large-scale simulations, Message Passing Interface (MPI), CUDA GPU (graphics processing unit), as well as parallel computing algorithms were utilized. The results extracted from the microgravity experiments conducted on the International Space Station were employed to validate several aspects of the models.

ACKNOWLEDGEMENT

My sincere gratitude to my advisor, Dr. Felicelli, whose great support made this possible. I am thankful to have had him as an advisor and a mentor. Working for him has given me experience I will take to every facet of my career in the future. Moreover, my special thanks to my co-advisor Dr. Mohsen Eshraghi for his wonderful guidance, assistance, and support.

I also would like to thank my committee members for their valuable comments and suggestions. Dr. Braun has been a great mentor throughout graduate school, and for that I am extremely grateful. My special thanks go to my family. I would like to express my sincere thanks to my parents for their endless love and support. I would like to thank my brother Ali for his kindness and good wishes.

This work was funded by the National Aeronautics and Space Administration (NASA) through Grant Number NNX16AT75G and 80NSSC20K0736. In addition, I would like to acknowledge the University of Akron and California State University, Los Angeles, for their sponsorship.

TABLE OF CONTENTS

	Page
LIST OF FIGURES	ix
LIST OF TABLES	xv
CHAPTER	
I. INTRODUCTION	1
1.1. Motivation	1
1.2. Literature Review	3
1.3. Research Objectives	9
1.4. Intellectual Merit	10
1.5. Broader Impact	11
1.6. Dissertation Structure	11
II. MICROGRAVITY EXPERIMENTS	12
2.1. PFMI Microgravity Experiment	12
2.2. MICAST Microgravity Experiment	20
III. Methodology	27
3.1. Finite Difference Method for Energy Equation.....	27
3.2. Lattice Boltzmann Model for Fluid Flow and Solute Transport	28
3.3. The Original Shan-Chen Model for Multiphase Flow.....	31
3.4. Improvements to the Original Shan-Chen Model.....	33
3.4.1. Realistic Equation of State	33

3.4.2. Force with a Higher Order of Isotropy (E8 Force Scheme) and Middle-Range Repulsion Force	34
3.5. Multiphase Lattice Boltzmann Phase Field Method.....	37
3.5.1. Solving the Cahn-Hilliard Equation for Interface Capturing with the WENO Scheme	37
3.5.2. Phase Field Lattice Boltzmann Method for Flow Field	40
3.6. Cellular Automaton Model for Dendritic Growth.....	42
3.7. Allen-Cahn Phase Field Model for Dendritic Growth.....	44
IV. MODEL VALIDATION	47
4.1. Validation of Shan-Chen Based Model with Phase Separation	47
4.2. Validation of Cahn-Hilliard Phase Field Model with Contact Angle.....	50
4.3. Validation of Cahn-Hilliard Phase Field Model with Rayleigh Instability	52
4.4. Validation of Cahn-Hilliard Phase Field Model with Marangoni Convection Around a Bubble	56
4.5. Validation of Cellular Automaton Model with Free Dendrite Growth	59
4.6. Validation of Dendritic Growth of PFMI Experiment with Phase Field and Cellular Automaton Using Scalable GPU Programming	61
V. RESULTS	68
5.1. Columnar Dendritic Growth with Original Shan-Chen Model	68
5.2. Dendritic Growth with the Enhanced Shan-Chen Model.....	71
5.3. Columnar Dendrite Growth with Phase field	72
5.4. Fully Coupled Modeling of Bubble Dynamics during Solidification	77
5.5. Effect of Bubble Size on Dendrite Growth	81
5.6. Spurious Grain Formation due to Marangoni convection during Directional Solidification of Alloys in μ -g Environment of International Space Station	97
5.7. Three-Dimensional Phase Field Modeling of Columnar to Equiaxed Transition	107

VI. CONCLUSION129

VII. POTENTIAL CONTINUATIONS133

 7.1. Adaptive Grid Refinement Method133

 7.2. Effect of Marangoni Convection on Microstructure Formation During Additive
 Manufacturing133

 7.3. Hybrid MPI-CUDA Approach134

BIBLIOGRAPHY135

LIST OF FIGURES

Figure	Page
1:	(a) Photograph of the Succinonitrile–0.24 wt% water sample tube for Pore Formation and Mobility Investigation. The spring and piston system as well as the thermocouples (thermocouples #5 and 6 on the left) are visible. The ring heater was placed over thermocouple #3, which is also visible at the center of the sample. (b) Another view of the sample tube. Thermocouples #5 and #6 can be seen in about 30 cm distance. Thermocouples #4 and #3 are in 27 cm and 24 cm distances, respectively.....13
2:	(a) Pore Formation and Mobility Investigation processing unit, (b) Schematic of the Pore Formation and Mobility Investigation processing unit section [1,85].....14
3:	PFMI 15 experiment showing the heater moving towards the left, leading to solidification of the melt from the right.15
4:	The arrow shows the typical bubble path. (Courtesy of Grugel, R.N [3]).....16
5:	Rotation of fragmented dendrites (marked by inclined red lines) in 19 seconds of PFMI 15 experiment during sample remelting stage. The location of the bubble is marked by the blue circle. The times in the left and right images are 21:14:25 and 21:14:44, respectively.17
6:	Progression of columnar dendrite growth into the molten zone seen in a SCN-0.24 wt% water alloy over a 22 second period18
7:	Dendrite tip speed vs. time for overall six dendrites growing from the left (red) and right sides (cyan) of the PFMI experiment tube. The reference time (t=0) was set at 21:25:31. The solid line represents the mean velocity averaged over 10 seconds for the right and left dendrites19
8:	The effects of bubble on dendritic growth: (a) initial condition, without the presence of any bubble and (b) after one minute, the bubble disturbs the growth and results in bending of the dendritic array.....20
9:	Schematic presentation of partial melting of [100] oriented dendritic Al-7 wt% Si MICAST seed samples and their subsequent directional solidification in the absence of natural convection on the International Space Station.....22

10:	Comparison of primary dendrite alignments in the seed portion (a), and in the portion which was directionally solidified on the Space Station (MICAST-7, Al-7 wt% Si, $10 \mu\text{ms}^{-1}$) (c). (b) and (d) are the corresponding Electron Back Scattered Diffraction images based on the orientation map shown in the inset. Several grains can be seen in (c) and (d), where the primary dendrites are orientated very differently from those preexisting in the seed portion which are all aligned along [100]. The sample diameter is 7.8 mm.	23
11:	X-ray radiograph of directionally solidified MICAST2-12 samples (32Kcm^{-1} , $40 \mu\text{ms}^{-1}$ within its alumina crucible. Two surface shrinkages where the melt was detached from the crucible wall appear as dark voids (marked by white arrows) near 20 and 26 cm locations.....	24
12:	Misoriented grains in the vicinity of surface-voids in the Al-7 wt% Si sample directionally solidified in μ -g on ISS (MICAST2-12). The distances in the white marker at the bottom of these figures are with respect to the eutectic temperature (T_E) at the onset of DS. The misoriented grains (dendrites) are shown within the black circle. The 11-mm long surface void in (a) is located immediately ahead of the mushy-zone at the onset of DS, and the 2.5 mm long surface void in Figure (b) is located at 52.5 mm from T_E	26
13:	Discrete velocity direction for (a) D_2Q_9 and (b) D_3Q_{15} [69].....	28
14:	Definition of directions for e_γ in the two-belt lattice.	35
15:	Results after 30,000 iterations for different values of G_1 and G_2 based on the values in Table 3 at $T = 0.9T_{cr}$. (a) case 1, (b) case 2, (c) case 3, (d) case 4, (e) case 5, (f) case 6. (Blue: gas, red: liquid).....	48
16:	Contact angle validation for PF model for initially semi-circle droplet. Different contact angles were simulated by changing the order parameter, ϕ_w 0.7, 0.4, and 0.3 for top and bottom walls as a boundary condition, resulting in the contact angles 40° , 105° , and 130° , after 20000 iterations.....	51
17:	The contact angle as a function of ϕ_w . The simulation results are shown with blue circles, while the solid line connects $(0, 180^\circ)$ and $(1, 0^\circ)$ as a guide.	52
18:	Interface evolution during simulation for $At=0.5$ and $Re=256$ at (a) $t=0$, (b) $t=2$, (c) $t=3$, (d) $t=4$, and (e) $t=5$	54
19:	Comparison of spike and bubble position in (a) $At = 0.5$ and $Re=256$ with He et al. (1999) results, (b) $At = 0.999$ and $Re=256$ with Shao et al. [72] results. All of the parameters are non-dimensional.	55
20:	Interface evolution for density ratio of 1,000 ($At=0.999$) and $Re=256$ at (a) $t=0$, (b) $t=0.5$, (c) $t=1$, and (d) $t=1.25$	55

21:	Steady state velocity (a) and temperature (b) distribution around the bubble.	58
22:	Bubble migration velocity normalized by analytical velocity versus normalized time. The time is non-dimensionalized by R/U	59
23:	Comparison between the present model and LGK analytical model for (a) Peclet number, (b) interface velocity, and (c) tip radius at different undercoolings	60
24:	Schematics of the simulation domains: (a) 2D with the domain size of $1.1 \times 2 \text{ mm}^2$ (b) 3D with the domain size of $1.0 \times 1.1 \times 0.6 \text{ mm}^3$.	
25:	2D simulation of dendritic morphologies at different times with cellular automata (a-d), and phase field (e-h) methods. The average growth rate for cellular automata and phase field methods at $t=18 \text{ s}$ were $71.46 \text{ } \mu\text{m/s}$ and $68.95 \text{ } \mu\text{m/s}$, respectively.	64
26:	Evolution of 3D dendrites at different times simulated by cellular automata method (a-d) and phase field method (e-h). The average tip velocity was calculated to be $93.1 \text{ } \mu\text{m/s}$ for cellular automata model and $121.4 \text{ } \mu\text{m/s}$ for phase field model.	66
27:	Initial condition for simulation of dendrite-bubble interaction (Yellow: solid, red: liquid, blue: gas).....	69
28:	Results of original Shan-Chen model at time: (a) 0.0013, (b) 0.0026, (c) 0.00387, and (d) 0.0052 s for a density ratio of 4. (Yellow: solid, red: liquid, blue: gas)....	70
29:	Results of the enhanced model at time (a) 0.0013, (b) 0.0026, (c) 0.00387, and (d) 0.0052 s for $T=0.7T_{cr}$, which corresponds to a density ratio of 40. (Yellow: solid, red: liquid, blue: gas).	71
30:	Results of the phase field model at time (a) 0.0013, (b) 0.0026, (c) 0.00387, and (d) 0.0052 s for a density ratio of 40. (Yellow: solid, red: liquid, blue: gas).	73
31:	Velocity magnitude along the centerline in the width and height direction (a) $X^*=1/2$ Shan-Chen model, (b) $Y^*=1/2$ Shan-Chen model, (c) $X^*=1/2$ phase field, (d) $Y^*=1/2$ phase field, at $t = 0.0013 \text{ s}$	74
32:	The arrow shows the typical bubble path. (Courtesy of Grugel, R.N [3]).....	75
33:	Gas porosity evolution in a directionally solidified Al-30 wt% Cu alloy. (Courtesy of R. Mathiesen, Sintef,[124]).	76
34:	Simulation of bubble-dendrite interactions for $Ma=0.515$ at (a) $t=0$, (b) $t=0.072$, (c) $t=0.144$, (d) $t=0.216$, (e) $t=0.288$, and (f) $t=0.36 \text{ s}$. (Red: solid, light blue: bubble, blue: liquid).....	79

35:	Concentration field around dendrites (a) without any convection (b) with Marangoni convection. Both results are presented at $t= 0.36$ s	80
36:	Streamline and concentration distribution around the dendrites growing under $Ma=0.515$ at $t=0.144$ s	81
37:	Simulation of dendrite growth in presence of two small bubbles for $Ma=0.025$ at (a) $t=0$, (b) $t= 0.072$ and (c) 0.144 s (Red: solid, light blue: bubble, blue: liquid) 81	
38:	Effect of Marangoni Convection on dendrite growth at (a) $Ma=0.5$, (b) $Ma=5$, (c) 10, (d) 20, (e) 50, (f) 60.5 related to bubble radius (a) $R=0.03$, (b) 0.187, (c) 0.264, (d) 0.3736, (e) 0.59 and (f) 0.65 mm respectively. All of the results are presented for $t= 11.2$ s. (Red: solid, light blue: bubble, blue: liquid)	83
39:	Effect of Marangoni convection on temperature contour and fluid flow at (a) $Ma=0.5$, (b) $Ma=5$, (c) 10, (d) 20, (e) 50, (f) 60.5 related to bubble radius (a) $R=0.03$, (b) 0.187, (c) 0.264, (d) 0.3736, (e) 0.59 and (f) 0.65 mm respectively. .84	
40:	Fluid velocity magnitude at the midsection of the domain ($y=2.5$ mm) for different Ma numbers.	85
41:	Simulation results of induced Marangoni convection during remelting. Here streamlines are colored with Velocity Magnitude. The domain size is $3.5 \times 3.5 \times 6$ mm ³ and flow direction is clockwise.	88
42:	Fluid velocity along a specific path line: comparison between PFMI experiment and the current dissertation.	88
43:	Schematic of the initial condition for the simulation. The temperature gradient is imposed on the vertical direction ($G=716$ K/m). The domain size is $3.5 \times 3.5 \times 6$ mm ³ . Eighty-one seeds were placed on the bottom wall, all with the same crystallographic direction [001]. A bubble with a diameter between 0.5 mm to 1.5 mm was in front of the solid front.	89
44:	Simulation results for bubble-dendrite interactions at $t=2.97$ s for different bubble sizes: (a) $d=1.5$ mm and (b) $d=0.5$ mm. All dimensions are in mm and streamlines are colored with temperature. The domain size is $3.5 \times 3.5 \times 6$ mm ³	91
45:	Effect of bubble size on dendrite velocity (a) $d=0.5$ mm, (b) $d=1.0$ mm, (c) $d=1.3$ and (d) $d=1.5$ mm. The dendrites were grouped based on their distance from the bubble. The horizontal dashed line is the PFMI average dendrite growth speed. The black line corresponds to the mean velocity of all dendrites from simulations.	92
46:	Effects of bubble size (corresponding to Ma number 9,35.8, 60.5 and 80.6) on average dendrite speed during the simulation for (a) far, (b) moderate distance and (c) near distance from the bubble.....	93

47:	(a) Solute concentration, and (b) temperature fields around the bubble at $t=2.97$ s ($d=1.5$ mm).	95
48:	Velocity Magnitude along the A-B line in Figure 47 for different bubble sizes at $t=2.97$ s.....	95
49:	2D sections of dendritic morphologies at the plane $y=3.75$ mm at $t=2.97$ s for different bubble sizes.	96
50:	Morphology of dendrite array when the heater was moved away, and the dendrites grew and solidified (21:26:44). The mushy-zone schematic used in (c) for simulation were imported from (b) shown above. (c) Schematic of the initial conditions for the simulation. The temperature gradient is imposed on the horizontal direction ($G = 716$ K/ m). The domain size is 2×4 mm ² . The 1.3 mm diameter bubble is located within the mushy-zone close to the array-tips.	98
51:	Schematics of the domain dimensions and initial conditions for COMSOL simulations considering two void lengths (a) 11 mm, and (b) 2.5 mm. The temperature gradient was 3200 K/m. The voids were located in the melt ahead of the solidifying mushy zone.	99
52:	Simulation of the temperature field and streamlines for PFMI 15 experiment (bubble diameter= 1.3 mm, $Ma= 312$, and $G = 716$ K/ m) at (a) $t=0.0$ s, (b) $t= 6.6$ s, (c) $t=13.3$ s, and (d) $t=20.0$ s.	101
53:	Rotation and velocity components of fragmented dendrite during 20 s of simulation (a) rotation of fragmented dendrites, (b) the angular velocity, (c) and (d) velocity components in horizontal (u) and vertical (v) directions, respectively. The mean rotation speed of the side-branch fragment observed during the PFMI experiment was 1.66 deg/s compared to 1.3 deg/s for simulation.	102
54:	Simulation of the temperature field and streamlines for MICAST2-12 experiment (bubble diameter= 2.5 mm, $Ma= 104$ and $G = 3200$ K/ m) at (a) $t=0.0$ s, (b) $t= 0.66$ s, (c) $t=1.33$ s, and (d) $t=2.0$ s. The fragmented dendrite is seen as the small white rectangle in the domain.	103
55:	Rotation and velocity components of fragmented dendrite caused by Marangoni convection during 2 seconds of simulation for MICAST in the presence of 2.5 mm diameter bubble (a) rotation of fragmented dendrites, (b) the angular velocity, (c), and (d) velocity component in x and y direction respectively.....	104
56:	Simulation of the temperature field and streamlines for MICAST2-12 experiment (void length= 11 mm, $Ma= 2016$ and $G = 3200$ K/ m) at (a) $t=0.0$ s, (b) $t= 0.66$ s, (c) $t=1.33$ s, and (d) $t=2.0$ s. The fragmented dendrite is shown with white rectangle.	105

57:	Rotation and velocity components of fragmented dendrite caused by Marangoni convection during 2 seconds of simulation for MICAST in presence of the 11 mm long void (a) rotation of fragmented dendrites, (b) the angular velocity, (c) and (d) velocity component in x and y direction respectively.	106
58:	The simulated solidification map for Inconel 718 alloy. The solid lines show the predictions based on Equations (76) and (77).....	116
59:	Evolution of dendrites with time for different solidification regimes: (a-c) columnar: $G=106$ K/m and $V_p=10^{-3}$ m/s, (d-f) <i>mixed</i> : $G=104$ K/m and $V_p=10^{-2}$ m/s, (g-i) <i>equiaxed</i> : $G=103$ K/m and $V_p=0.1$ m/s when initial grain seeds distance equals to $12\ \mu\text{m}$	118
60:	Grain orientation and solute maps for a cross-sectional plane passing through the middle Y-axis, (a) final grain structure at $t=0.3215$ s and (b) solute field at $t=0.1862$ s for $G=106$ K/m and $V_p=0.001$ m/s, (c) final grain structure at $t=0.5801$ s and (d) solute field at $t=0.2795$ s for $G=104$ K/m and $V_p=10^{-2}$ m/s, (e) final grain structure at $t=1.1867$ s and (f) solute field at $t=0.7801$ s for $G=102$ K/m and $V_p=0.1$ m/s when initial grain seeds distance equals to $12\ \mu\text{m}$	120
61:	Solution map for columnar (a to c) at $t=0.3215$ and equiaxed growth (d to e) at $t=1.1867$ s at different heights of the sample. (a) and (d) correspond to $Z=0.1$ mm, (b) and (e) correspond to $Z=0.2$ mm and (c) and (f) correspond to $Z=0.3$ mm ...	121
62:	Maximum solute concentration for different growth regime at different vertical distances when the solid fraction in the whole domain is 0.9.....	123
63:	Columnar grain structure for a) $GV_p=100$ K/s, b) $GV_p=1000$ K/s, c) $GV_p=10000$ K/s when initial grain seeds distance equals to $12\ \mu\text{m}$	124
64:	Equiaxed grain structure for a) $GV_p=10$ K/s, b) $GV_p=100$ K/s, c) $GV_p=1000$ K/s when initial grain seeds distance equals to $12\ \mu\text{m}$	125

LIST OF TABLES

Table	Page
1: Physical properties for SCN-0.24 wt% water alloy.....	12
2: Physical properties for Al-7 wt% Si Alloy. [90].....	21
3: Parameters used in the simulation.....	49
4: The spurious current magnitude and normalized total time in the original Shan-Chen and the enhanced model.	49
5: Parameters used for simulation of the Marangoni benchmark problem. All values are listed in lattice units.	57
6: Grid size, time step and calculated tip velocity for 2D and 3D simulations for cellular automata and phase field models	65
7: Parameters used for dendritic growth with the original Shan-Chen Model [104,121].....	69
8: Comparison between different parameters among different LB models.	74
9: the PFMI experiment parameter for SCN-0.24 wt% water alloy.	78
10: Simulation conditions and final grain structures predicted by the present model for directional solidification of Inconel 718 alloy.	115
11: Comparison of analytical PDAS $\lambda_1(\mu\text{m})$ predictions to the present model.	126
12: Effect of different initial grain size on PDAS for columnar growth at different cooling rates.	127
13: Correlation matrix showing pairwise correlation Pearson's coefficient between variables.	127
14: Effects of initial grain size on the final grain size for equiaxed growth at different cooling rates.	128

CHAPTER I

INTRODUCTION

1.1. Motivation

During a solidification process under suitable conditions, once the solid is nucleated from the supercooled liquid, the subsequent growth of the spherical seed becomes unstable, which leads to the formation of dendrites in most cases. Two types of dendrites are observed during solidification. When the undercooling is constant through the sample, the forming dendrites are mostly equiaxed such as snowflakes. The columnar dendrite growth is observed when there is a temperature gradient in the sample. Some industrial applications prefer equiaxed grains, such as casting for car engines, and some require columnar grains due to its superiority in creep properties, such as gas turbine blades.

Producing a uniformly aligned microstructure can improve material properties of products such as turbine blades. The aligned microstructure can be obtained under a controlled condition of imposing a constant temperature gradient and carefully maintaining the solid front velocity along one axis [1]. However, variable solute concentrations and temperature differences within the sample can induce fluid flow, which causes defects such as severe microsegregation, freckles and misoriented grains that can compromise the material properties such as fatigue life [2–4]. Under normal

gravity conditions, the flow in the melt is considered as either forced or natural convection. The latter is produced by the density or solute concentration difference within the melt. It is expected that the effect of convection can be minimized if solidification takes place in microgravity. Therefore, understanding of the underlying physics can be enhanced by studying dendrite growth under microgravity conditions. The results of microgravity experiments can be considered as a benchmark for developing solidification theories [1,5–8] and microstructural homogeneity has shown significant enhancement when compared to earth experiments [9]. However, traces of convection were observed in PFMI (Pore Formation and Mobility Investigation) and MICAST (Microstructure formation in casting of technical alloys under a diffusive and magnetically controlled convection conditions) microgravity experiments. The details of these experiments will be covered in Chapter 2.

Since the effect of gravity is minimized in the microgravity experiments, we should look for other mechanisms responsible for convection. Shrinkage flow can be induced by the difference of solid and liquid densities and Marangoni convection is observed when there is a gradient of surface tension [10]. For both pore formation mobility investigation (PFMI) and microstructure formation in casting (MICAST) microgravity experiments, a comparatively large motion and rotation of fragmented dendrites were observed. The effects of the shrinkage flow are quite clearly detected when there is a cross-section change in the domain [11]. However, in case of PFMI and MICAST experiments, the cross-section of the samples remains constant. Although the shrinkage effects were observed in isothermal solidification [12] or the directional solidification case [13,14] in microgravity conditions, the motion and rotation were

minimal with orders of magnitude smaller than the Marangoni convection [15]. In addition, in the directional solidification case [13,14], the small movement was observed towards the cold region. However, a relatively fast motion of fragmented dendrites toward the hot region cannot be explained by the shrinkage effect. The only other explanation is the existence of Marangoni convection. We believe that the flow in both microgravity experiments is caused by Marangoni convection because of the large bubble adhered to the ampoule in a positive thermal gradient.

1.2. Literature Review

During solidification, the temperature and solute concentration gradients can induce fluid flow. The melt flow affects the transport processes at the solid-liquid interface and results in defects - such as microsegregation, and freckles [2,4]. Effect of forced convection or natural convection induced by temperature or solute gradients on dendrite growth were widely studied experimentally for terrestrial conditions [16–23]. Studying dendrite growth under microgravity conditions can improve our fundamental understanding of the underlying physics. Since there is no natural convection involved during the process, the microgravity experiment can provide a benchmark to develop more accurate solidification theories [3,5–7]. On earth, due to the density difference between the liquid and gas, the bubbles can rise through the melt and eventually burst back to the atmosphere. However, in microgravity conditions, gas porosity formation can be a significant issue, since the bubbles are more likely to get trapped during solidification [24]. Presence of the bubbles during solidification processes affects the mechanical properties of solidified components [25–28]. Furthermore, it creates

Marangoni convection (also called thermocapillary convection), influencing the growth of dendrites and their orientation [8,29].

Bubble nucleation, motion, and microstructural evolution during solidification on earth have been studied experimentally [30–33]. Kim et al. [34,35] investigated the bubble dynamics at the S/L (solid/liquid) interface for an Al-Si binary alloy in different solidification orientations (i.e., solid front moves downward or upward with respect to gravity). It was observed that bubbles in the melt rise due to buoyancy and eventually reach a constant terminal velocity where the buoyancy and drag forces are in equilibrium. Based on the S/L interface velocity and the pore terminal velocity, three scenarios are observed. If the interface velocity is smaller than pore terminal velocity, the bubble could escape from the S/L interface and rise through the melt. However, the bubble can be pushed along or get entrapped at higher interface velocities. It should be noted that when solidification starts from the top and moves downward, the gas bubble cannot rise through the liquid anymore and only get trapped or pushed away by the growing S/L interface. The same observation of bubbles being entrapped or being repelled by the advancing S/L interface was reported by Jamgotchian et al. for SCN-acetone alloys [31].

In the microgravity experiments, the presence of bubbles becomes a severe problem due to the absence of buoyancy which negates bubbles floating away from the S/L interface. Therefore, a large number of bubbles have been observed in microgravity samples when compared to their terrestrial counterparts [1,9,36]. Under microgravity conditions, Marangoni convection is responsible for bubble transport. Surface tension gradients induce Marangoni convection at the free surface of the bubbles due to the imposed temperature gradient. For most materials, the variation of surface tension with

temperature (temperature coefficient of surface tension) is negative, which means the melt has a lower surface tension at higher temperatures. This variation in the surface tension at the bubble interface induces a Marangoni force on the melt that moves the fluid from lower surface tension region (hot) to the higher surface tension region (cold). The reaction force on the bubble causes a free bubble to move from the cold to the hot region. The magnitude of the induced Marangoni convection is proportional to the bubble size [37,38].

During solidification, solubility of the gas phase in the melt is reduced. This reduction happens because the solid has a higher density than the melt; therefore, the melt pressure decreases during solidification. As a result, some dissolved gas is essentially rejected and reappears as bubbles. The probability of bubble nucleation near the solid front is higher than in the melt as it is heterogeneous in nature, whereas nucleation in the melt is homogeneous [24].

In one scenario, gas accumulates at the solidification front to form bubbles. Based on the rate of bubble nucleation and the solid front velocity again, three possible scenarios were reported. First, the bubbles can be trapped by the solid interface, which leaves a spherical or distorted bubble entrapped between the dendrites. In the second case, if the bubble is big enough, the induced Marangoni convection is strong enough to disengage the bubble from the interface, which then drifts away to the warmer region. In the third case, the bubble is trapped at the interface but continues to grow at the front by absorbing gas from the liquid through diffusion. This phenomenon leaves an elongated-shaped bubble, or rat tail, in the solid and a spherical cap extending into the melt. These observations can be verified either by direct observation during solidification or

microscopic examination of areal sample sections after solidification is completed [1,3,24,39].

The bubbles are also observed to reside at the crucible wall [3]. The bubbles in contact with the wall might remain in place as the Marangoni convection is not strong enough. These bubbles can grow by absorbing gas in the melt through diffusion, which then increases the Marangoni force exerted on them. Later in the experiment, detachment from the wall can be observed for some of these bubbles. Since it is not clear when a detachment from the wall takes place, it is reasonable to observe how residing bubbles at the crucible can affect the microstructure through induced convection [8,40]. Li et al. [10] pointed out that the nucleation position of the surface pore is most likely close to the dendritic front. They identified two distinct fluid flows caused by the presence of the bubble. The flow can be caused by the expansion of the surface bubble via diffusion in the melt or by Marangoni convection.

Numerical simulations offer an alternative for investigating the mechanism behind bubble formation and their interactions during the solidification of metallic alloys. The problem consists of different physics that need to be solved simultaneously. Mathematically the dendritic growth solidification problem requires appropriate tracking of the moving boundary interface, separating the Solid and Liquid. Consequently, one can split the whole system into three sub-domains: liquid region, solid region, and the Solid/Liquid interface.

Many researchers studied different aspects of dendrite growth numerically using phase field (PF), level set, cellular automation (CA) or front tracking methods [34,41–44]. There is a relatively limited number of studies attempting to model the convection

effects during the dendritic solidification. Beckerman et al. [45] proposed a 2D PF model to simulate a uniform flow over a stationary immersed dendrite. Al-Rawahi and Tryggvason [46] presented a 2D front tracking method for the simulation of dendritic growth considering the effects of convection and latent heat. Chatterjee and Chakraborty [47] adopted a 2D hybrid enthalpy-porosity technique with a thermal LB method to simulate convection-diffusion transport during solidification. Lu et al. [48] proposed a 3D PF model to study the effects of fluid flow on free dendritic growth. Using PF method, Do-Quang and Amberg [49] modeled growth of a single dendrite, moving due to the gravity.

Modeling Marangoni convection in the dendrite scale is a challenging and computationally demanding task; discretization errors in the calculation of interfacial forces may generate spurious currents. The methods used to simulate multiphase flows (liquid/gas) include interface tracking, and interface capturing methods. In the interface tracking methods, the interface location is marked with a separate grid or set of surface meshes. The interface location is calculated explicitly during the simulation. The boundary integral method [50], the Arbitrary Lagrangian-Eulerian (ALE) method [51], and all front tracking methods [52–57] belong to this category. In the interface capturing methods, instead of tracking a sharp interface, a function represents the thin (but non-zero width) interface between the phases. Thus, fluid properties continuously change from one fluid to another across the interface. The volume of fluid (VOF), phase field, and level set methods belong to this category [58–60].

The lattice Boltzmann (LB) method is an effective alternative, for simulation of multiphase flows, especially for transient no-slip boundary conditions. In the LB method,

instead of solving the Navier-Stokes (NS) equation, particle distribution functions are defined for discrete kinetic equations. By solving these kinetic equations in both spatial and velocity spaces, the NS equation can be recovered. Due to its simplicity, local structure, ease in dealing with complex geometries, explicit nature, and suitability for parallel computing, it has been applied to simulate various physical phenomena [61–63].

There are many LB models proposed for solving multiphase flow, including color gradient model based on Rothman and Keller lattice gas model, Shan-Chen (pseudopotential) model [64], free energy model [65,66], and LB-PF method [67,68].

It is known that PF is the most accurate multiphase method amongst LB models. It can be applied in problems with high-density contrast successfully; the generated spurious current is the least among all LB multiphase models [61,69]. In the PF method, in addition to the fluid flow equation, another equation is solved to determine the interface location. The fluid flow distribution function for the local density and momentum is approximated using mean values of density and momentum to improve stability, and then a cohesion force is introduced to the mean field flow. The He-Chen-Zhang (HCZ) model is a variation of the PF-based multiphase method in which two sets of distribution functions are used to recover the NS and Cahn–Hilliard (CH) equations [66,67,70–72].

The LB-PF model has been successfully used to simulate many problems of multiphase flow [73–76]. Most of the researchers solved the CH equation using a separate set of LB distribution functions. However, solving the CH equation by LB technique has several disadvantages that may compromise the results. First, selecting the relaxation parameter for the CH equation is not trivial. Many researchers used the same

relaxation parameter for the CH equation as for the fluid flow equation. This selection is not physically acceptable since different values of relaxation time might lead to different results. Next, the LB model cannot entirely recover the CH equation, because the recovered CH equation always has higher-order terms which do not exist in the CH equation. It is also hard to discretize the convection term of the CH equation in using LB method. Finally, it is hard to use higher-order explicit time stepping for LB method because LB models usually use second order explicit time-stepping, which makes the time step size significantly small for the CH equation [62,72,77]. In this dissertation, the CH equation was solved by a “Weighted Essentially Non-Oscillatory” (WENO) [78] scheme for the convection term along with a third-order Runge Kutta time stepping scheme.

There are few studies available on the numerical simulation of the bubble dynamic during dendrite growth using CA and original Shan-Chen LB model [79,80]. It is known that the original Shan-Chen model generates a high spurious current and can only handle limited density and viscosity ratios [81]. A more elaborate numerical model should be used to overcome these problems associated with the Shan-Chen model.

1.3. Research Objectives

This dissertation tries to look for new mechanisms responsible for observing non-homogeneity in the microstructure of microgravity directional solidification experiment caused by Marangoni convection in the melt when the melt gets detached from the crucible wall. The existence of such bubbles or voids creates a free liquid-vapor interface existing under a thermal gradient responsible for the Marangoni convection [10,82,83].

Specifically, we are trying to answer whether the induced Marangoni convection during solidification is strong enough to cause primary dendritic arms to lean away from the original direction or cause the rotation of broken-off sidearms. Large-scale models are developed and tested against several microgravity experiments to address these complex phenomena.

Another key aim is to perform feasibility studies of different models for simulating phenomena in the microscale, such as Marangoni convection and microstructure growth, to find highly accurate methods suitable for large-scale computer models. We utilized Message Passing Interface (MPI) and CUDA GPU (Graphics Processing Unit) to speed up the large-scale simulations.

1.4. Intellectual Merit

The outcome of this research is a unique, high-performance, multiphysics computational platform to perform precise and efficient solidification process simulations that improve real-world manufacturing applications in the automotive and aerospace industries.

The research results can help better understand the complex physics behind the bubble-dendrite interaction. The developed model can predict the effects of bubbles on microstructure which would help eventually enhance the microstructure and properties of solidified components.

1.5. Broader Impact

The results of this dissertation will impact the research for multi-physics problems, especially in fluid dynamics, heat transfer, phase transition, and material science with application to casting, welding, and additive manufacturing. Most of the software simulating alloy solidification does not consider the effects of Marangoni convection on microstructure. This research makes a significant contribution to these ends.

1.6. Dissertation Structure

In Chapter 1, a survey of relevant literature and the motivation of this dissertation is presented.

In Chapter 2, the PFMI experiment is introduced and discussed in detail.

In Chapter 3, the LB, CA and PF methods are introduced. The enhancement of Shan-Chen based multiphase LB method is discussed in detail.

Chapter 4 focuses on validation of the developed model against the experimental and theoretical results.

Chapter 5 presents the results of induced bubble on microstructure in two and three dimensions.

Chapter 6 contains the summary and conclusions of the work.

Chapter 7 covers recommendations for future research work in this area.

CHAPTER II
MICROGRAVITY EXPERIMENTS

2.1. PFMI Microgravity Experiment

The Pore Formation and Mobility Investigation (PFMI) was a series of experiments conducted in the glovebox facility aboard the International Space Station (ISS) to investigate the morphological evolution of SCN-water binary alloys in a diffusive growth regime under controlled directional solidification conditions. The material properties of the alloy are well known [1].

Table 1. Physical properties for SCN-0.24 wt% water alloy.

Gibbs Thomson coefficient (Γ) [84]	6.4×10^{-8} mK
Kinematic viscosity of fluid (ν) [1]	2.67×10^{-6} m ² /s
Thermal diffusivity (α_T) [1]	1.16×10^{-7} m ² /s
Solute diffusivity (α_C) [1]	1.5×10^{-9} m ² /s
Liquidus slope (m_L) [1]	-8.8 (K/wt%)
Partitioning coefficient (k) [1]	0.03
Density of solid ρ_s [1]	1016 kg/m ³
Density of liquid ρ_l [1]	907 kg/m ³
Melting Point (T_M)	331.39 K
Specific Heat (C_P)	2000 J/kg/K
Surface Tension (σ_0)	0.042 N/m
anisotropy (ϵ)	0.01

The experiment ampoule was a 12mm OD, 10mm ID, 30 cm long cylindrical glass ampoule filled with approximately 23 cm of the SCN-0.24 wt% water “alloy.” The spring and piston system (as shown in Figure 1) allowed expansion and contraction of the

sample material during heating and cooling, thus preventing voids that could induce thermocapillary convection. Temperatures along the sample length were recorded by six in-situ k-type, 0.5 mm diameter, thermocouples which were separated by 3 cm; thermocouples #5 and 6 occupied the same position. The nitrogen bubbles were intentionally injected into the sample tube to ensure the existence of the bubble during the experiment. The experiment began after the sample tube was inserted to the processing unit, which had translational and temperature control (max 130° C). Two Cohu 3812 cameras mounted 90° apart moved on a separate translation system that allowed for viewing and recording of the sample.

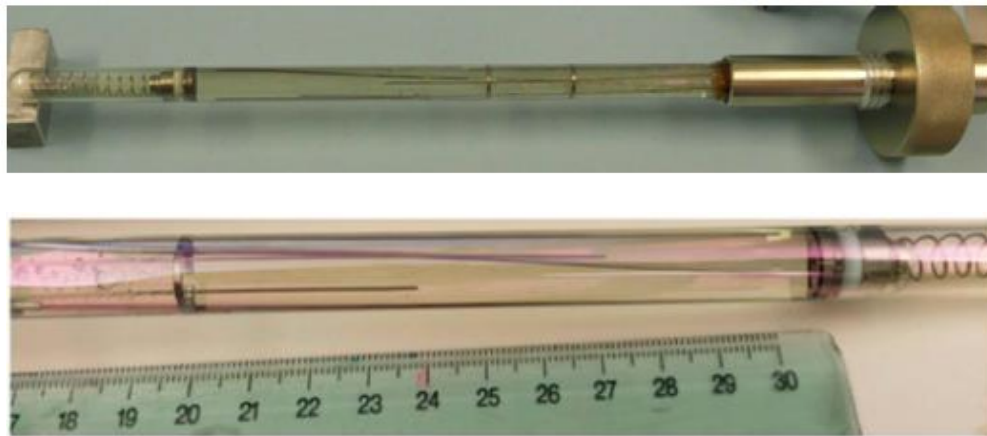
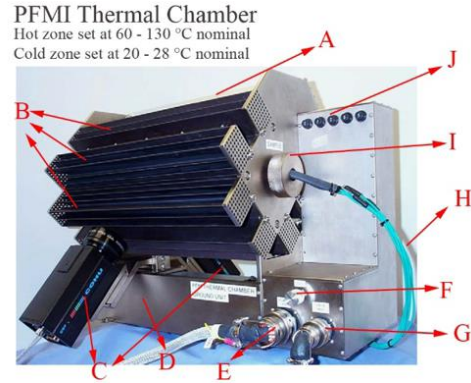


Figure 1. (a) Photograph of the Succinonitrile–0.24 wt% water sample tube for Pore Formation and Mobility Investigation. The spring and piston system as well as the thermocouples (thermocouples #5 and 6 on the left) are visible. The ring heater was placed over thermocouple #3, which is also visible at the center of the sample. (b) Another view of the sample tube. Thermocouples #5 and #6 can be seen in about 30 cm distance. Thermocouples #4 and #3 are in 27 cm and 24 cm distances, respectively.

Figure 2 shows the details of the processing unit with the main zone, booster zone, and cold zone.

A: Lintec translational stage for gradient zone
 B: Aluminium Heat exchangers (6 total)
 C: Two Cohu 3812 video cameras
 D: Lintec translational stage for camera is underneath camera mount bracket
 E: Power J606
 F: Rheostat to adjust backlight intensity inside chamber
 G: Data J603
 H: six Sample ampoule assembly thermocouples wires
 I: Sample ampoule assembly inserted into right side of the thermal chamber
 J: Five airplane-style pop-out circuit breakers



A: Watchdog control and thermocouple on hot side of Thermal Electric Device
 B: Circuit Breakers protect ringheater, main heater, Thermal Electric Device's, two motors, LED's and encoder
 C: Main heater Control & Watchdog Thermocouples
 D: Main Heater Thermostat
 E: Ring Heater Watchdog & control TC and Thermostat

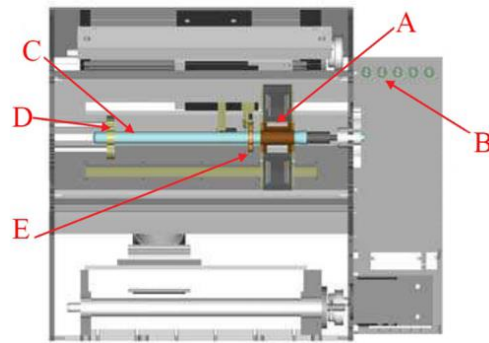


Figure 2. (a) Pore Formation and Mobility Investigation processing unit, (b) Schematic of the Pore Formation and Mobility Investigation processing unit section [1,85].

Images from PFMI-15 I experiment were extracted using Video to Picture: A Photo Digital Studio software and image analysis were done using ImageJ. For these experiments, a translational ring heater was moved to a center portion, over a thermocouple, of the still solid sample. The ring heater was then turned on which effectively initiated a liquid zone and left primary SCN dendrites present on both sides [86]. This section of the experiment is identified as remelting part.

Once the desired temperature was reached, the ring heater was turned off and quickly removed from the viewing area; solidification then initiated at both sides of the liquid zone from pre-existing grains. Figure 3 shows a portion of the experiment, where a ring-heater was present in the view, keeping the middle portion of the sample melted. The

heater was then translated to the left at 21:23:31 (Greenwich time) leading to cooling of the melt and solidification started both sides of preexisting grains. More details about the design, configuration, and data acquisition in PFMI experiments can be found in Refs. [1,3].

A: Thermocouples
 B: Heater
 C: Solid/Liquid Interface



Figure 3. PFMI 15 experiment showing the heater moving towards the left, leading to solidification of the melt from the right.

During remelting, the gas trapped in the solid forms bubble. Furthermore, some nitrogen bubbles are intentionally inserted during the initial filing of the sample to guarantee the presence of bubbles during the experiment. Bubbles may stay in their place during the remelting or may push away to the warmer region during the remelting process. However, it was observed that larger bubbles tend to stick to the walls, whereas the smaller bubbles were more likely to get stuck between the dendrites. The larger bubbles induce a Marangoni convection which disrupts the dendrite arrays due to melting at the primary root region by the influx of warmer melt. No Marangoni convection was

observed around the smaller bubbles. The strength of induced Marangoni convection has a direct relation to the bubble size [3,24].

The thermocapillary flow field associated with a bubble trapped between dendrites is presented in Figure 4. This figure shows a 1.3 mm diameter bubble adhered to the wall in the bottom of the picture near the solid/liquid interface which initiated a circulatory flow. The flow path was tracked by following tiny bubbles which are schematically shown in Figure 4-a by arrows. By following the tiny bubbles in their path, it is observed that the fluid velocity decreases as the tracers move from point A near the interface to Point B. The returning tracers accelerate as they approach the solid/liquid interface. Figure 4-b shows a tracer after it has made a circuitous route through the liquid and is now approaching the dendritic interface. Figure 4-c shows the same tracer just before it enters the mushy zone. After moving about 1 mm deep it into the mushy zone, it reemerges 5 seconds later at the location shown in Figure 4-d. The distance traveled was ~ 3.1 mm resulting in an average flow velocity of ~ 0.62 mm/s.

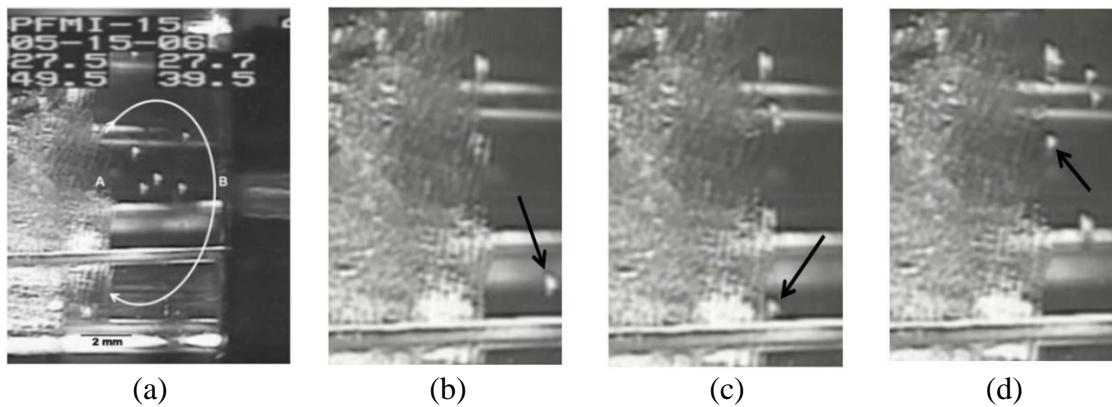


Figure 4. The arrow shows the typical bubble path. (Courtesy of Grugel, R.N [3])

During another time segment which involved remelting of a previously directionally solidified sample the side fragmented side-arms of the primary dendrites

were observed to rotate as if they are falling side-ways from their vertical orientation. Figure 5 contains two typical time-lapse images from the PFMI-15 experiment to demonstrate this observation. The location of the 1.3 mm diameter nitrogen bubble adhered to the crucible within the yet unbelted mushy zone on the left is marked within blue circles. The red line marks one of the side arms whose location and orientation can be seen in the left and the right images of Figure 5 corresponding to 21:14:25 and 21:14:44 GST, respectively. The 800 μm long side-branch rotated about 31.5 degrees in 19 seconds.

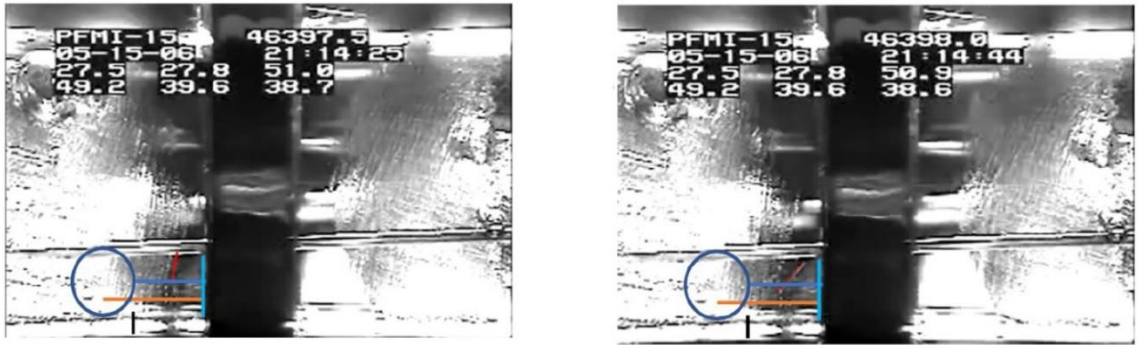


Figure 5. Rotation of fragmented dendrites (marked by inclined red lines) in 19 seconds of PFMI 15 experiment during sample remelting stage. The location of the bubble is marked by the blue circle. The times in the left and right images are 21:14:25 and 21:14:44, respectively.

The subsequent resolidification of the molten sample would provide information on microstructural development as a function of the key processing parameters in microgravity conditions. The series of photographs seen in Figure 6 were taken during the PFMI-15 experiment over a 22-second time period after subsequent resolidification of the molten sample. The photographs show the evolution of dendrite growth under diffusive conditions. Imprinted on the photographs (from the top, left to right) are the

sample name, position, date, time, and the six thermocouple readings. Note that thermocouple #3 has the highest temperature.

The average primary dendrite arm spacing is around 350 μm . The cylindrical object in the middle of photographs is one of the thermocouples. Progression of the dendrites growing in from both sides can be seen.



(a)



(b)



(c)



(d)

Figure 6. Progression of columnar dendrite growth into the molten zone seen in a SCN-0.24 wt% water alloy over a 22 second period.

The area of interest shown in Figure 6 was located over thermocouple #3, which is not visible. The width of the picture shown in Figure 6 is 7 mm. Considering the

constant temperature gradient, and assuming the highest temperature located in the previous location of the heater, undercooling ahead of the advancing front was determined to be from 0.5 to 1.0 K. The temperature gradient G was also calculated to be approximately 716 K/m. By analyzing the temperature time series recorded by thermocouples 3 and 4, the average cooling rate was calculated to be 0.1 K/s during the experiment.

The tip velocities for three dendrites in both right and left side were measured and plotted against time in Figure 7 for a 90-second time period (21:25:35 through 21:27:05). For simplicity, the reference time ($t=0$) was set at 21:25:31 (Greenwich time). The reported average results were an average value over 10 seconds. Since the ring heater moved to the left side during its removal, the right side of the sample was cooler compared to the left side, which leads to higher tip velocities for the dendrites growing on the right side.

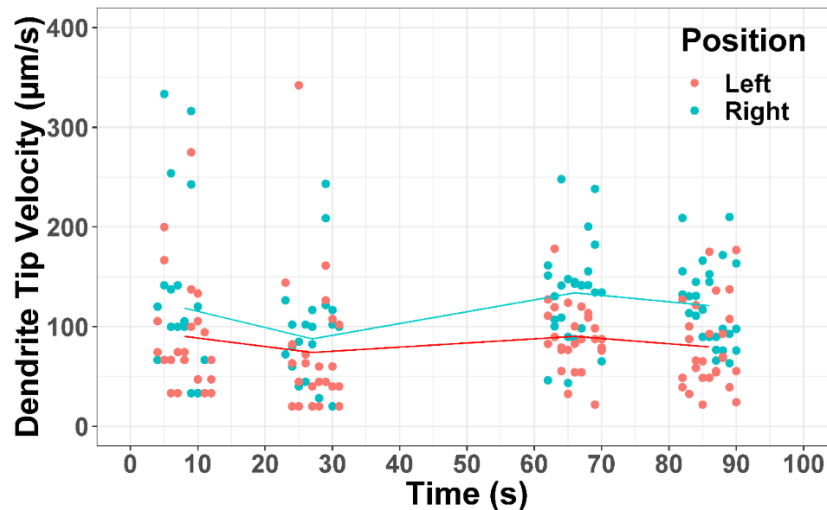


Figure 7. Dendrite tip speed vs. time for overall six dendrites growing from the left (red) and right sides (cyan) of the PFMI experiment tube. The reference time ($t=0$) was set at 21:25:31. The solid line represents the mean velocity averaged over 10 seconds for the right and left dendrites.

The average tip velocity for the left and right dendrites during the experiment was calculated as $84 \pm 52 \mu\text{s/s}$ and $103.52 \pm 52 \mu\text{s/s}$, respectively. The variability of the results (for instance $\pm 52 \mu\text{s/s}$ for the left side) is reported based on standard deviation. The overall average can be considered as $94 \mu\text{s/s}$.

During solidification in Figure 8 (a)-(b), a bubble on the order of 1 mm diameter traversed through the dendritic array and remained at the solid-liquid interface. Figure 8 (b), which was taken one minute after Figure 8 (a), suggests that the dendrites away from the bubble are longer and bending sideways toward the bubble, while the bubble decreases the solidification rate of adjacent dendrites. The simulation results provide more information about the effects of the bubble on dendrite growth.

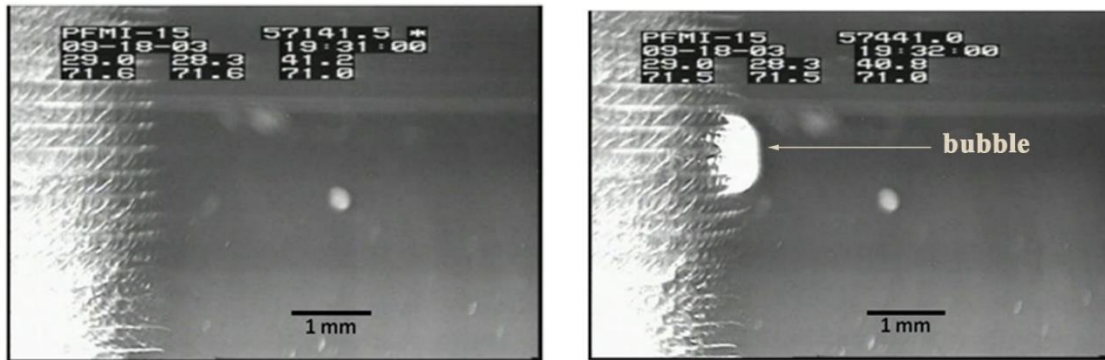


Figure 8. The effects of bubble on dendritic growth: (a) initial condition, without the presence of any bubble and (b) after one minute, the bubble disturbs the growth and results in bending of the dendritic array.

2.2. MICAST Microgravity Experiment

The purpose of the MICAST experiment is to conduct directional solidification experiments in diffusive growth regimes for Al-7 wt% Si in the microgravity environment aboard the International Space Station. Detailed descriptions of the

MICAST experiment, samples, and operation are given in references [87–89]. The material properties of the alloy are listed in Table 2.

Table 2. Physical properties for Al-7 wt% Si Alloy. [90]

Temperature coefficient of surface tension (γ)	$-0.18 \times 10^{-3} \text{ N/(mK)}$
Density (ρ)	2408 kg/m^3
Thermal diffusivity (α_T)	$2.97 \times 10^{-5} \text{ m}^2/\text{s}$
Dynamic viscosity (μ)	$1.16 \times 10^{-3} \text{ Pa}\cdot\text{s}$
Melting point (T_m)	933.45 K

Briefly a 7.8 mm diameter cylinders machined from the terrestrial grown [100] oriented Al-7 wt% Si dendritic bars were inserted in an alumina crucible housed in the European Space Agency (ESA) Sample Cartridge Assembly (SCA) inserts. The SCAs were held stationary and the Low Gradient Furnace (LGF) or Sample Quench Furnace (SQF) was translated towards or away from the sample to achieve the remelting of solid sample and its subsequent directional solidification in the low gravity environment of International Space Station [88,89].

As shown schematically in Figure 9, remelting of a single crystal dendritic array seed having [100] alignment and its subsequent directional solidification (DS) in the absence of convection should result in maintaining the same [100] dendrite alignment along the entire sample length. It should also not produce any radial or longitudinal microsegregation which are caused mainly by the gravity driven thermosolutal convection.

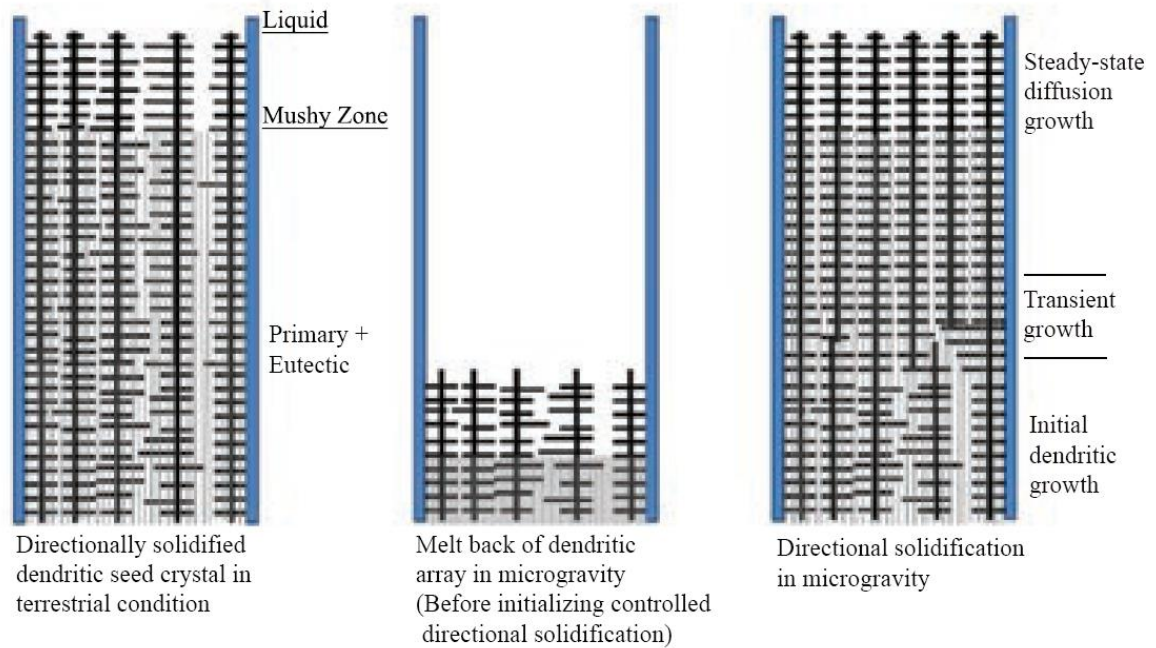


Figure 9. Schematic presentation of partial melting of [100] oriented dendritic Al-7 wt% Si MICAST seed samples and their subsequent directional solidification in the absence of natural convection on the International Space Station.

But, as indicated in Figure 10, a comparison of the microstructures from the directionally solidified portion of the MICAST samples with those from their un-melted [100] seed portion shows that spurious grains did form during DS on the Space Station. The Electron Back Scattered Diffraction (EBSD) images, Figure 10(b) and (d), correspond respectively to Figure 10 (a), the seed portion of MICAST-7, and Figure 10 (c), the portion solidified at $10 \mu\text{m s}^{-1}$ on ISS. The colors in the inset figure represent various crystallographic orientations. In the un-melted seed portion of the sample, the primary dendrites are all aligned along [100], whereas in the portion that was grown on the Space Station there are several grains with very different orientations.

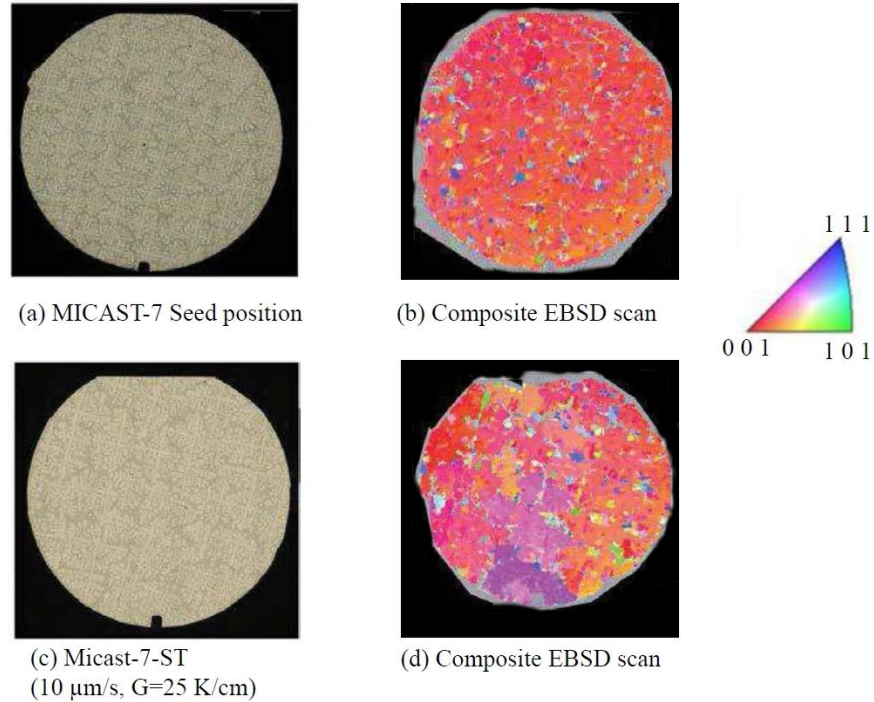


Figure 10. Comparison of primary dendrite alignments in the seed portion (a), and in the portion which was directionally solidified on the Space Station (MICAST-7, Al-7 wt% Si, $10 \mu\text{ms}^{-1}$) (c). (b) and (d) are the corresponding Electron Back Scattered Diffraction images based on the orientation map shown in the inset. Several grains can be seen in (c) and (d), where the primary dendrites are orientated very differently from those preexisting in the seed portion which are all aligned along [100]. The sample diameter is 7.8 mm.

Melt undercooling which can cause nucleation of new solid crystals ahead of the solidifying mushy-zone is not possible during DS of alloys in a constant diameter mold in the microgravity environment because of the positive thermal gradient in the melt ahead of the liquid-solid interface. In the absence of any cross-section change during DS the shrinkage flow towards the liquid-solid interface because of the difference between the solid and liquid densities would be expected to be about 10% of the alloy growth speed and cannot account for the significant rotation speeds of fragmented side arms observed in this experiment.

A closer look at the MICAST samples shows the presence of voids on their surfaces where the melt had apparently detached from the crucible wall. Figure 11 shows an X-ray radiograph of the MICAST2-12 sample in its alumina crucible after it was directionally solidified on the ISS. The cold end of the directionally solidified sample is on the left and its hot end is on the right in this image. The long thin white cylinders are the thermocouples which were attached to the crucible surface to record the thermal history during its DS. The arrows point to two typical locations where the cavity associated with the detached liquid column during DS can be clearly seen at about 20 and 26 cm. It is not clear, what caused these voids to form. However, every sample processed in these SCAs under the joint ESA-NASA MICAST research program, including more than 12 from the European investigators [91], showed such surface voids.

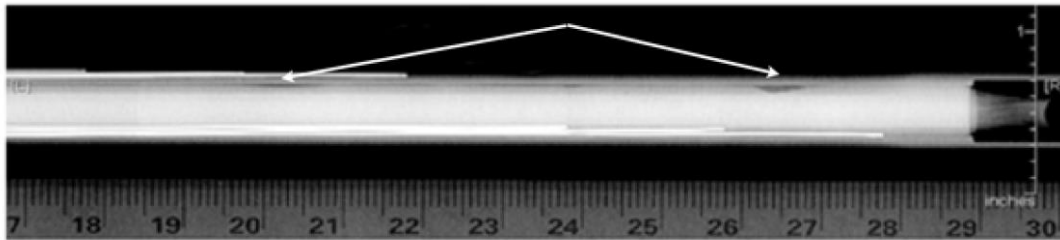
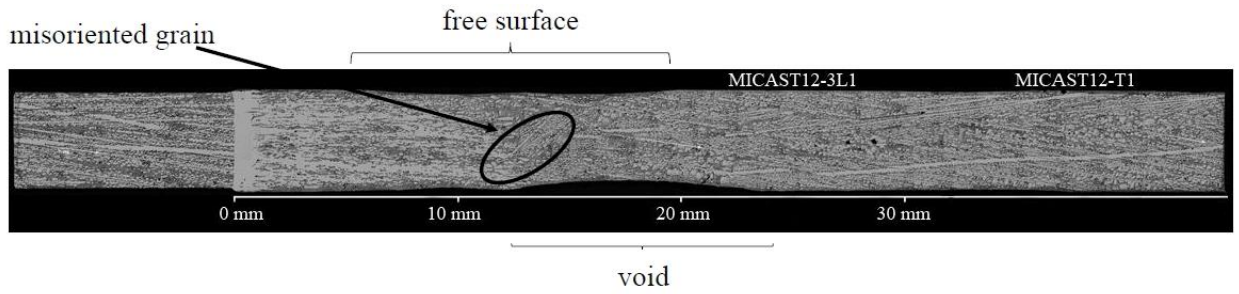


Figure 11. X-ray radiograph of directionally solidified MICAST2-12 samples (32 Kcm^{-1} , $40 \mu\text{ms}^{-1}$) within its alumina crucible. Two surface shrinkages where the melt was detached from the crucible wall appear as dark voids (marked by white arrows) near 20 and 26 cm locations.

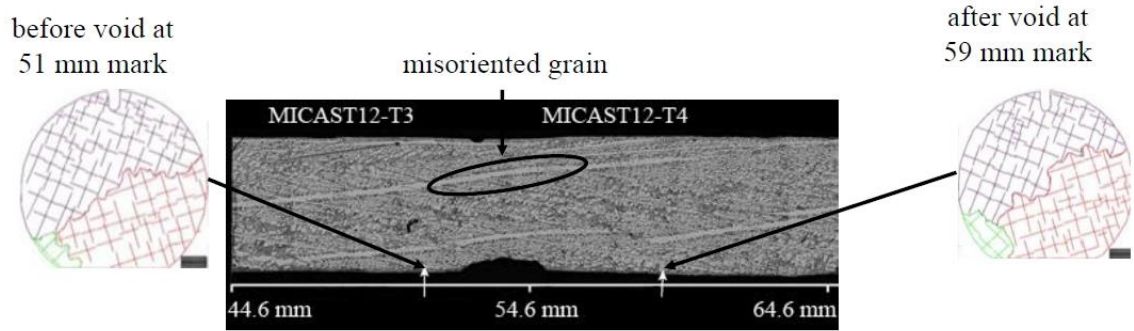
We believe that the spurious grains in the MICAST samples formed by the dendrite side-branch fragmentation and rotation phenomenon, except that it was the Marangoni convection arising from the voids present on the surface of the liquid column in regions where the melt got detached from the ampoule wall that was responsible for the solutal remelting of the dendrite side arms and their rotation.

Transverse and longitudinal sections from the Al-7 wt% Si alloy samples directionally solidified in the space under the MICAST-program (MICAST-6, 7 and 2-12) [88,89] were metallographically examined in the vicinity of surface pores. The precise locations where the spurious grains formed were determined by serial sectioning and metallography at appropriate locations along the sample length. The geometry and location of the surface pore with respect to the location of the spurious grains was also determined. The angles between the primary dendrite array in the seed portion and those within the misaligned grains were measured from the longitudinal images typically shown in Figure 12 for the directionally solidified MICAST2-12 sample. The distances indicated in the white marker at the bottom of these figures are with respect to the eutectic temperature (TE) at the onset of DS. The misoriented grains (dendrites) are shown within the black circle. The initial mushy-zone length is 12.5 mm for this sample [88] (Figure 12 (a)). The 11-mm long surface void in Figure 12(a) is the same void which was seen at 20-cm location in the X-ray radiograph presented earlier in Figure 11. It is located immediately ahead of the mushy zone at the onset of DS. The 2.5 mm long surface void in Figure 12(b) is located between 52.5 and 55 mm from TE. The misoriented dendrite has formed immediately ahead of this pore.

As opposed to the PFMI experiments, in MICAST samples, it is impossible to physically observe the rotation of dendrite fragments associated with Marangoni convection driven by the surface voids generated by the melt getting detached from the crucible walls. However, it is possible to assume that rotation of fragmented side arms due to the Marangoni convection is responsible for the formation of these misoriented dendrites in the directionally solidified MICAST2-12 sample also (Figure 12).



(a)



(b)

Figure 12. Misoriented grains in the vicinity of surface-voids in the Al-7 wt% Si sample directionally solidified in μ -g on ISS (MICAST2-12). The distances in the white marker at the bottom of these figures are with respect to the eutectic temperature (T_E) at the onset of DS. The misoriented grains (dendrites) are shown within the black circle. The 11-mm long surface void in (a) is located immediately ahead of the mushy-zone at the onset of DS, and the 2.5 mm long surface void in Figure (b) is located at 52.5 mm from T_E . [92]

CHAPTER III

Methodology

A description of the equations and methods applied for the simulations is discussed in this chapter. The problem is governed by solving continuity, fluid flow, energy, and solute transport equations. A lattice Boltzmann (LB) model was developed to simulate the fluid flow and transport field while a cellular automaton (CA) or Allen–Cahn PF algorithm was applied to track the dendrite growth.

3.1. Finite Difference Method for Energy Equation

The governing equation for heat transfer in an incompressible fluid is expressed as:

$$\frac{\partial T}{\partial t} + \mathbf{u} \cdot \nabla T = \alpha_T \nabla^2 T + \dot{Q} \quad (1)$$

α_T is the thermal diffusivity and \dot{Q} is the overall cooling rate (K/s) in the domain.

The cooling rate is the average temperature drop during the experiment measured by thermocouples. The explicit discretization in time with the upwind finite difference method was utilized to solve for heat transfer. For details about the discretization scheme in finite difference, see Ref. [93].

3.2. Lattice Boltzmann Model for Fluid Flow and Solute Transport

In this dissertation, the LB model was employed for solving both fluid flow and solute transport equations. In the LB method, the macroscopic fluid properties are described by sets of distribution functions in a D-dimensional lattice by Q fixed discrete velocity vectors. In this work, D_2Q_9 and D_3Q_{15} lattice is used in two and three dimensions respectively. In D_3Q_{15} lattice for instance, which is used in this dissertation for fluid flow calculations, each node at position x has a probability distribution function $f_\alpha(x, t)$ in each of the 15 discrete velocity vectors, e_α . The structure of D_2Q_9 and D_3Q_{15} is demonstrated in Figure 13.

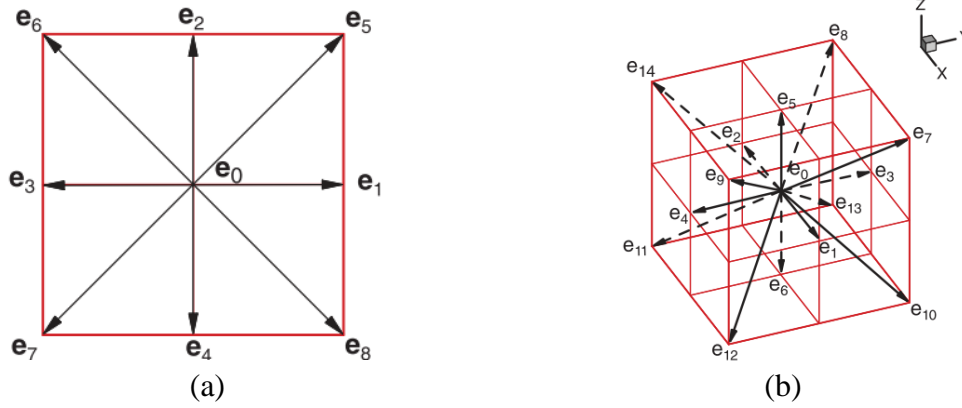


Figure 13. Discrete velocity direction for (a) D_2Q_9 and (b) D_3Q_{15} [69].

The distribution functions are evolved during explicit streaming and collision steps. The discrete velocity, e_α for D_2Q_9 is defined as:

$$\begin{cases} e_\alpha = c(0,0) & \text{for } \alpha = 0 \\ e_\alpha = c(\pm 1,0) & \text{for } \alpha = 1,3 \\ e_\alpha = c(0,\pm 1) & \text{for } \alpha = 2,4 \\ e_\alpha = c(\pm 1,\pm 1) & \text{for } \alpha = 5 - 8 \end{cases} \quad (2)$$

While for D_3Q_{15} it is defined as:

$$\begin{cases} \mathbf{e}_\alpha = c(0, 0, 0) & \text{for } \alpha = 0 \\ \mathbf{e}_\alpha = c(\pm 1, 0, 0), (0, \pm 1, 0), (0, 0, \pm 1) & \text{for } \alpha = 1 - 6 \\ \mathbf{e}_\alpha = c(\pm 1, \pm 1, \pm 1) & \text{for } \alpha = 7 - 14 \end{cases} \quad (3)$$

$c = \Delta x / \Delta t$ is defined as a lattice constant, where Δx and Δt are lattice grid size and time step, respectively. The LB equation with the Bhatnagar–Gross–Krook (BGK) approximation [94] is written as:

$$\begin{aligned} & f_\alpha(\mathbf{x} + \mathbf{e}_\alpha \Delta t, t + \Delta t) - f_\alpha(\mathbf{x}, t) \\ &= -\frac{1}{\tau_v} \left(f_\alpha(\mathbf{x}, t) - f_\alpha^{eq}(\mathbf{x}, t) \right) + \mathbf{F}_\alpha(\mathbf{x}, t) \Delta t \end{aligned} \quad (4)$$

All the parameters are defined in the lattice units. In Equation (4), $\mathbf{F}_\alpha(\mathbf{x}, t)$ is the Marangoni induced force acting in the free surface of the bubble, while τ_v is the non-dimensional relaxation time related to local kinetic viscosity ν_{lb} as $\nu_{lb} = c_s^2(\tau_v - 0.5)$. The difference in surface tension along the free surface of the bubble produces a force that induces Marangoni convection:

$$F = \mu A \frac{\partial u}{\partial n} = \gamma A \frac{\partial T}{\partial s} \quad (5)$$

s and n denote the direction tangential and normal to the free surface of the bubble and γ is the temperature coefficient of the surface tension, u is the velocity in the tangential direction, A is the free surface area of the bubble and μ is the dynamic viscosity of the fluid. The induced force is added to each discrete velocity direction during the collision step as [95].

$$\mathbf{F}_\alpha = -\frac{3\omega_\alpha\rho\mathbf{e}_\alpha \cdot \mathbf{F}}{c^2} \quad (6)$$

The weight coefficient, ω_α , in D_2Q_9 is determined as:

$$\omega_\alpha = \begin{cases} \frac{4}{9} & \alpha = 0 \\ \frac{1}{9} & \alpha = 1,2,3,4 \\ \frac{1}{36} & \alpha = 5,6,7,8 \end{cases} \quad (7)$$

In D_3Q_{15} it is defined as:

$$\omega_\alpha = \begin{cases} \frac{16}{72} & \alpha = 0 \\ \frac{8}{72} & \alpha = 1 - 6 \\ \frac{1}{72} & \alpha = 7 - 14 \end{cases} \quad (8)$$

f_α^{eq} in Equation (4) is the equilibrium distribution function defined as:

$$f_\alpha^{eq} = \omega_\alpha\rho\left[1 + \frac{3(\mathbf{e}_\alpha \cdot \mathbf{u})}{c^2} + \frac{2(\mathbf{e}_\alpha \cdot \mathbf{u})^2}{2c^4} - \frac{3\mathbf{u}^2}{2c^2}\right] \quad (9)$$

The macroscopic density and velocity at each node are recovered as:

$$\rho(\mathbf{x}, t) = \sum_{\alpha=0}^{8 \text{ or } 14} f_\alpha(\mathbf{x}, t) \quad (10)$$

$$\rho(\mathbf{x}, t)\mathbf{u}(\mathbf{x}, t) = \sum_{\alpha=0}^{8 \text{ or } 14} f_\alpha(\mathbf{x}, t)\mathbf{e}_\alpha \quad (11)$$

The following macroscopic equations can be recovered by using the Chapman-Enskog expansion [96]:

$$\frac{\partial \rho}{\partial t} + \rho \nabla \cdot \mathbf{u} = 0 \quad (12)$$

$$\rho\left(\frac{\partial \mathbf{u}}{\partial t} + \mathbf{u} \cdot \nabla \cdot \mathbf{u}\right) = -\nabla P + \nabla \cdot (\mu \nabla \mathbf{u}) + \mathbf{F} \quad (13)$$

The same computational domain with a uniform grid size and time step, was used to solve the solute transport equation. The solute transport equation considering diffusion and advection is defined as:

$$\frac{\partial C_l}{\partial t} + \mathbf{u} \cdot \nabla C_l = \alpha_c \nabla^2 C_l \quad (14)$$

α_c is solute diffusivity and $C_l(\mathbf{x}, t)$ is macroscopic solute concentration. The LB for transport equation is written as:

$$g_\alpha(\mathbf{x} + \mathbf{e}_\alpha \Delta t, t + \Delta t) - g_\alpha(\mathbf{x}, t) = -\frac{1}{\tau_c} \left(g_\alpha(\mathbf{x}, t) - g_\alpha^{eq}(\mathbf{x}, t) \right) \quad (15)$$

Where the relation between solute diffusivity in lattice unit α_{LB} and non-dimensional relaxation time, τ_c , is defined as: $\alpha_{LB} = c_s^2(\tau_c - 0.5)$, based on the Chapman-Enskog expansion [97]. The equilibrium distribution function in the LB model is defined as [98]:

$$g_\alpha^{eq} = \omega_\alpha C_l \left[1 + \frac{3(\mathbf{e}_\alpha \cdot \mathbf{u})}{c^2} \right] \quad (16)$$

Finally, the macroscopic concentration is calculated as:

$$C_l(\mathbf{x}, t) = \sum_{\alpha=0}^{8 \text{ or } 14} g_\alpha(\mathbf{x}, t) \quad (17)$$

3.3. The Original Shan-Chen Model for Multiphase Flow

The original Shan-Chen model [64] introduces a cohesion force term, $\mathbf{F}(\mathbf{x}, t)$, responsible for phase separation. This cohesion force satisfies the non-ideal equation of

state. Based on the pressure difference, the phase separation between different phases takes place:

$$\mathbf{F}(\mathbf{x}, t) = -G_1 \psi(\mathbf{x}, t) \sum_{\alpha} \omega_{\alpha} \psi(\mathbf{x} + \mathbf{e}_{\alpha} \Delta t, t) \mathbf{e}_{\alpha} \quad (18)$$

The parameter, ψ , is called the effective mass and is related to the equation of state. Here, G_1 controls the force exerted at each node by surrounding particles, with a positive (negative) value leading to a repulsive (attractive) force between particles. In this model, the phase separation occurs when G_1 is higher than a critical value. Using this scheme, only eight neighbor nodes are considered for calculating the cohesion force in the D_2Q_9 lattice. Shan and Chen [64] proposed the following equation for the effective mass:

$$\psi(\rho) = \psi_0 \left(- \exp \left(\frac{-\rho_0}{\rho} \right) \right) \quad (19)$$

Other researchers [80] have suggested different equations for effective mass as: $\psi(\rho) = \rho_0 \left(1 - \exp \left(\frac{-\rho_0}{\rho} \right) \right)$, or even as $\psi(\rho) = \rho_0$. In this dissertation, Equation (19) was used for calculating effective mass, where ψ_0 and ρ_0 are constant. The pressure term in this model has an extra term compared to the ideal gas equation of state. The pressure term is defined as:

$$P = c_s^2 \rho + \frac{c_s^2 G_1}{2} \psi^2(\rho) \quad (20)$$

To model the contact angle, the scheme developed by Benzi et al. [99] was employed. They suggested that adhesion force can be implemented in a similar way to cohesion force as follows:

$$F(\mathbf{x}, t) = -G_1 \psi(\mathbf{x}, t) \sum_{\alpha} \omega_{\alpha} \psi(\rho_w) s(\mathbf{x} + \mathbf{e}_{\alpha} \Delta t, t) \mathbf{e}_{\alpha} \quad (21)$$

Here, $s(\mathbf{x} + \mathbf{e}_{\alpha} \Delta t, t)$ is an indication parameter and has the value of 0 or 1 for fluid or solid nodes, respectively. $\psi(\rho_w)$ is the effective mass at the wall; by changing $\psi(\rho_w)$, different contact angles can be achieved.

Depending on the node type (solid or liquid), Equation (18) or (21) was used to simulate the interaction between nodes.

3.4. Improvements to the Original Shan-Chen Model

3.4.1. Realistic Equation of State

Based on Yuan and Schaefer [100], to model a higher density ratio and reduce the spurious current at the same time, a different equation of state (EOS) is utilized. Here, we use the Carnahan-Starling (C-S) EOS since it is stable, easy to implement, and generates a lower spurious current compared to another EOS [100]. No matter what EOS is used, the effective mass is expressed as:

$$\psi = \sqrt{\frac{(P - \rho c_s^2)}{G_1 c_s^2}} \quad (22)$$

The C-S EOS is expressed as:

$$P = \rho RT \frac{1 + \frac{b\rho}{4} + \left(\frac{b\rho}{4}\right)^2 - \left(\frac{b\rho}{4}\right)^3}{\left(1 - \frac{b\rho}{4}\right)^3} - a\rho^2 \quad (23)$$

Where $a = 0.4963(RT_{cr})^2/P_{cr}$, $b = 0.1873RT_{cr}/P_{cr}$. P_{cr} and T_{cr} are the critical pressure and temperature, respectively. Without losing the generality of the model, we assume $a = 1$, $b = 4$, $R = 1$ and by reducing the temperature in this equation, a higher density ratio is achieved [69,81].

3.4.2. Force with a Higher Order of Isotropy (E8 Force Scheme) and Middle-Range Repulsion Force

In the original Shan-Chen method, to compute the cohesion force, only eight neighbor nodes are considered. However, the cohesion force can include any number of neighbor nodes. By communicating only with the eight neighboring nodes in the D_2Q_9 lattice, the highest isotropy order that can be achieved is four (E4 force scheme). By considering the second layer (24 neighbor nodes), tensors of the eighth order can be produced (E8 force scheme) [81,101].

So, for the E8 force scheme, instead of using Equation (18), the force term in the D2Q9 lattice is expressed by:

$$\mathbf{F}(\mathbf{x}, t) = -G_2\psi(\mathbf{x}, t) \sum_{\gamma=1}^{24} \omega_\gamma \psi(\mathbf{x} + \mathbf{e}_\gamma \Delta t, t) \mathbf{e}_\gamma \quad (24)$$

where G_2 is a negative coefficient representing the attractive force, and ω_γ is the weighting coefficient. The direction of \mathbf{e}_γ is shown in Figure 14 and values for the weighting coefficients for the E8 force scheme are provided in Equation (25).

$$\omega_\gamma = \begin{cases} \frac{4}{21} & \gamma = 1,2,3,4 \\ \frac{4}{45} & \gamma = 5,6,7,8 \\ \frac{1}{30} & \gamma = 9,10,11,12 \\ \frac{4}{315} & \gamma = 13,14,15,16,17,18,19,20 \\ \frac{1}{2520} & \gamma = 21,22,23,24 \end{cases} \quad (25)$$

Chibbaro et al. [102] introduced a mid-range repulsion force between fluid particles. In the original Shan-Chen model, the attractive force causes the phase separation. Without adding any repulsive force, after some iterations, only one big bubble (drop) remains in the domain.

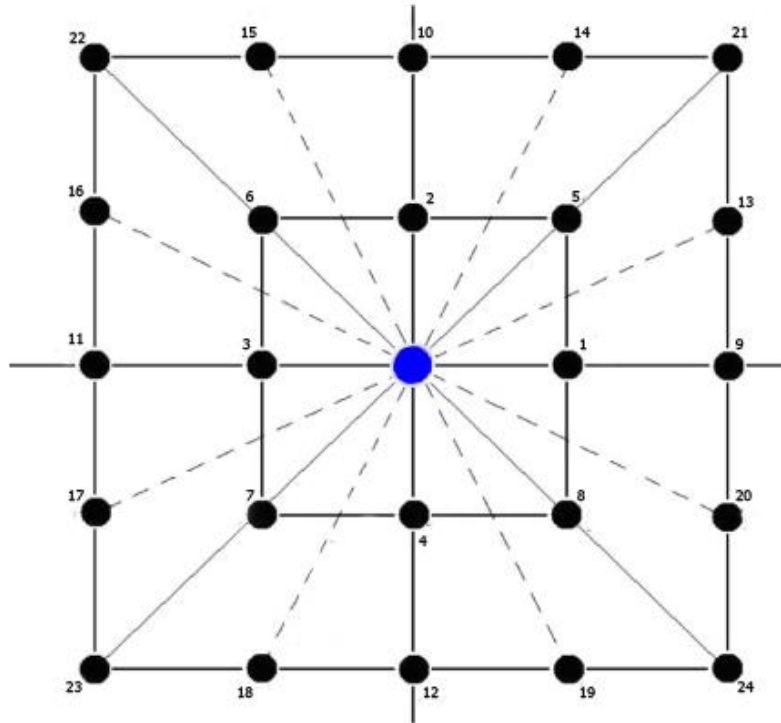


Figure 14. Definition of directions for e_γ in the two-belt lattice.

Basically, in Ref.[101], the authors introduced G_1 and G_2 parameters to model cohesion force. The G_1 is negative and represents the attractive force of the first belt of neighboring nodes, while G_2 is positive and represents the repulsive force of the second belt of neighboring nodes. The negative or positive signs here are, respectively, corresponding to attractive and repulsive forces between fluids.

Therefore, Equation (18) is modified as:

$$F(\mathbf{x}, t) = -G_1\psi(\mathbf{x}, t) \sum_{\alpha=1}^8 \omega_{\alpha}\psi(\mathbf{x} + \mathbf{e}_{\alpha}\Delta t, t)\mathbf{e}_{\alpha} - G_2\psi(\mathbf{x}, t) \sum_{\gamma=1}^{24} \omega_{\gamma}\psi(\mathbf{x} + \mathbf{e}_{\gamma}\Delta t, t)\mathbf{e}_{\gamma} \quad (26)$$

The pressure and effective mass for both cases are defined as:

$$P = c_s^2\rho + \frac{c_s^2(G_1 + G_2)}{2}\psi^2(\rho) \quad (27)$$

And

$$\psi = \sqrt{\frac{(P - \rho c_s^2)}{(G_1 + G_2)c_s^2}} \quad (28)$$

Note that in the case of the E8 force scheme without mid-range repulsion, $G_1 = 0$ and $G_2 < 0$. The weighting coefficient and the direction definitions are identical to Equation (25) and Figure 14. By introducing this midrange repulsive force, phenomena, such as spray formation, and the soft-glassy system can be modeled, which is impossible to model by short-range attraction force alone as it is mentioned in Ref [102].

In this dissertation, the realistic EOS and E8 force scheme with midrange repulsion force were implemented to improve the Shan-Chen model for bubble-dendrite

interactions during alloy solidification. To be succinct, this model will be referred to as “the enhanced model”.

3.5. Multiphase Lattice Boltzmann Phase Field Method

The hybrid LB-PF model along with the WENO scheme are explained here. The mean density of the two phases is used in the LB distribution functions, as suggested by Shao et al. [76]. This improves the computational efficiency while maintaining the ability to capture the local density.

3.5.1. Solving the Cahn-Hilliard Equation for Interface Capturing with the WENO Scheme

In the PF method, there is no need to track the interface. Instead, an order parameter, ϕ , is defined that gradually varies along the interface to distinguish between the liquid and bubble phases ($\phi=1$ represents fluid or melt, and $\phi=0$ represents bubble or gas). Based on the CH equation, the evolution of the interface can be computed by:

$$\frac{\partial \phi}{\partial t} + (\mathbf{u} \cdot \nabla) \phi = \nabla \cdot (\lambda \nabla \mu_\phi) \quad (29)$$

λ is a diffusion coefficient called mobility. μ_ϕ is the chemical potential, which is defined as the derivative of the free energy (Ψ'_ϕ) with respect to the order parameter:

$\mu_\phi = \Psi'_\phi(\phi) - \kappa \nabla^2 \phi$. If the free energy takes the double well form, $\Psi_\phi = \beta(\phi)^2(\phi - 1)^2$, then the chemical potential becomes $\mu_\phi = 4\beta\phi(\phi - 0.5)(\phi - 1) - \kappa \nabla^2 \phi$, where κ and β are related to the interface width and surface tension, σ [76].

Simulating multiphase flows with large density ratios is challenging since the high gradient of properties across the interface results in discontinuity of order parameter and numerical instability. Using upwind condition for the advection term along with calculating the derivatives with higher order accuracy would mitigate the discontinuity problem. The upwind WENO scheme with third order Runge Kutta Total Variation Diminishing (TVD) method was implemented to discretize the convection and temporal terms, respectively. Accordingly, Equation (29) can be rewritten as:

$$\frac{\partial \phi}{\partial t} = R(\phi) \quad R(\phi) = -\nabla \cdot (l) + \nabla \cdot (\lambda \nabla \mu_\phi) \quad (30)$$

The term $\mathbf{u}\phi$ is labeled as l for simplification. The discretization of the first term in the right-hand side of Equation (30) can be achieved in a variety of ways. In this work, the Lax-Friedrichs flux splitting was employed, which uses three stencils, formed by five points [78]. The convection term was calculated by flux terms determined by:

$$\nabla \cdot (\mathbf{u}\phi) = \nabla \cdot (l) = \frac{1}{\Delta x} \left(\tilde{l}_{i+\frac{1}{2}}^+ - \tilde{l}_{i+\frac{1}{2}}^- \right) + \frac{1}{\Delta x} \left(\tilde{l}_{i-\frac{1}{2}}^+ - \tilde{l}_{i-\frac{1}{2}}^- \right) \quad (31)$$

Where $\tilde{l}_{i+\frac{1}{2}}^+$ and $\tilde{l}_{i-\frac{1}{2}}^+$ are approximated by five points as:

$$\begin{aligned} \tilde{l}_{i+\frac{1}{2}}^+ = & \omega_0^+ \left(\frac{2}{6} l_{i-2}^+ - \frac{7}{6} l_{i-1}^+ + \frac{11}{6} l_i^+ \right) + \omega_1^+ \left(-\frac{1}{6} l_{i-1}^+ - \frac{5}{6} l_i^+ + \frac{2}{6} l_{i+1}^+ \right) \\ & + \omega_2^+ \left(\frac{2}{6} l_i^+ + \frac{5}{6} l_{i+1}^+ - \frac{1}{6} l_{i+2}^+ \right) \end{aligned} \quad (32)$$

And:

$$\begin{aligned}
\tilde{l}_{i+\frac{1}{2}}^- &= \omega_2^- \left(-\frac{1}{6} l_{i-1}^- + \frac{5}{6} l_i^- + \frac{2}{6} l_{i+1}^- \right) + \omega_1^- \left(\frac{2}{6} l_i^- + \frac{5}{6} l_{i+1}^- - \frac{1}{6} l_{i+2}^- \right) \\
&+ \omega_0^- \left(\frac{11}{6} l_{i+1}^- - \frac{7}{6} l_{i+2}^- + \frac{2}{6} l_{i+3}^- \right)
\end{aligned} \tag{33}$$

The stencil weights can be calculated as:

$$\begin{aligned}
\omega_0^\pm &= \frac{\alpha_0^\pm}{\alpha_0^\pm + \alpha_1^\pm + \alpha_2^\pm} & \omega_1^\pm &= \frac{\alpha_1^\pm}{\alpha_0^\pm + \alpha_1^\pm + \alpha_2^\pm} & \omega_2^\pm &= \\
&= \frac{\alpha_2^\pm}{\alpha_0^\pm + \alpha_1^\pm + \alpha_2^\pm}
\end{aligned} \tag{34}$$

Where:

$$\alpha_0^\pm = \frac{1}{10} \left(\frac{1}{\epsilon + IS_0^\pm} \right) \quad \alpha_1^\pm = \frac{6}{10} \left(\frac{1}{\epsilon + IS_1^\pm} \right) \quad \alpha_2^\pm = \frac{3}{10} \left(\frac{1}{\epsilon + IS_2^\pm} \right) \tag{35}$$

The parameter IS_k are defined as:

$$\begin{aligned}
IS_0^+ &= \frac{13}{12} (l_{i-2}^+ - 2l_{i-1}^+ + l_i^+)^2 + \frac{1}{4} (l_{i-2}^+ - 4l_{i-1}^+ + 3l_i^+)^2 \\
IS_1^+ &= \frac{13}{12} (l_{i-1}^+ - 2l_i^+ + l_{i+1}^+)^2 + \frac{1}{4} (l_{i-1}^+ - l_{i+1}^+)^2 \\
IS_2^+ &= \frac{13}{12} (l_i^+ - 2l_{i+1}^+ + l_{i+2}^+)^2 + \frac{1}{4} (3l_i^+ - 4l_{i+1}^+ + l_{i+2}^+)^2
\end{aligned} \tag{36}$$

And

$$\begin{aligned}
IS_0^- &= \frac{13}{12} \left(l_{i+1}^- - \frac{7}{6} l_{i+2}^- + \frac{11}{6} l_{i+3}^- \right)^2 + \frac{1}{4} (l_{i+1}^- - 4l_{i+2}^- + 3l_{i+3}^-)^2 \\
IS_1^- &= \frac{13}{12} (l_i^- - 2l_{i+1}^- + l_{i+2}^-)^2 + \frac{1}{4} (l_i^- + l_{i+2}^-)^2 \\
IS_2^- &= \frac{13}{12} (l_{i-1}^- - 2l_i^- + l_{i+1}^-)^2 + \frac{1}{4} (l_{i-1}^- - 4l_i^- + 3l_{i+1}^-)^2
\end{aligned} \tag{37}$$

In this way, $\tilde{l}_{i+\frac{1}{2}}^+$ in Equation (32) can be calculated. The value of $\tilde{l}_{i-\frac{1}{2}}^-$ can be calculated in the same way. Assuming constant mobility, the diffusion term in Equation (29) can be rewritten as:

$$\nabla^2 \mu_\phi = \frac{\left[\begin{array}{l} \mu_\phi(i+1, j+1) + \mu_\phi(i-1, j+1) + \mu_\phi(i+1, j-1) + \mu_\phi(i-1, j-1) \\ +4\mu_\phi(i+1, j) + 4\mu_\phi(i-1, j) + 4\mu_\phi(i, j+1) + 4\mu_\phi(i, j-1) - 20\mu_\phi(i, j) \end{array} \right]}{6\Delta x^2} \quad (38)$$

For marching in time, the third order TDV Runge Kutta scheme was implemented:

$$\begin{aligned} \phi^{(1)} &= \phi^t + \Delta t R(\phi^t) \\ \phi^{(2)} &= \frac{3}{4}\phi^t + \frac{1}{4}\phi^{(1)} + \frac{1}{4}\Delta t R(\phi^{(1)}) \\ \phi^{(3)} &= \frac{1}{3}\phi^t + \frac{2}{3}\phi^{(2)} + \frac{2}{3}\Delta t R(\phi^{(2)}) \end{aligned} \quad (39)$$

Where ϕ^t is ϕ value at time t , $\phi^{(1)}$ and $\phi^{(2)}$ are the transitional values in each time step. With a stable spatial and temporal discretization of the CH equation, the evolution of the interface for multiphase flow can be determined for large density ratios [72].

3.5.2. Phase Field Lattice Boltzmann Method for Flow Field

The fluid flow part of the model is based on the method introduced by Zheng et al. [103]. In this model, the LB equation for fluid flow is written as:

$$\begin{aligned}
& f_\alpha(\mathbf{x} + \mathbf{e}_\alpha \delta t, t + \delta t) \\
&= f_\alpha(\mathbf{x}, t) - \frac{1}{\tau} [f_\alpha(\mathbf{x}, t) - f_\alpha^{eq}(\mathbf{x}, t)] \\
&+ \left(1 - \frac{1}{2\tau}\right) \delta t (\mathbf{e}_\alpha - \mathbf{u}) [\nabla \rho c_s^2 (\Gamma_\alpha - \mathbf{e}_\alpha) + \mathbf{F}_\alpha \Gamma_\alpha]
\end{aligned} \tag{40}$$

Where \mathbf{F} is the sum of the surface tension F_s and body force F_b . $\Gamma_\alpha(\mathbf{u})$ is given as:

$$\Gamma_\alpha(\mathbf{u}) = \omega_\alpha \left[1 + \frac{3}{c^2} (\mathbf{e}_\alpha \cdot \mathbf{u}) + \frac{9}{2c^4} (\mathbf{e}_\alpha \cdot \mathbf{u})^2 - \frac{3}{2c^2} \mathbf{u}^2 \right] \tag{41}$$

The equilibrium distribution function can be expressed as:

$$f_\alpha^{eq} = \omega_\alpha [\rho_0 + \rho c_s^2 \left[\frac{3}{c^2} (\mathbf{e}_\alpha \cdot \mathbf{u}) + \frac{9}{2c^4} (\mathbf{e}_\alpha \cdot \mathbf{u})^2 - \frac{2}{3c^2} \mathbf{u}^2 \right]] \tag{42}$$

ρ_0 and ρ represent the mean and local density at each point, respectively. The mean density is initialized as $\frac{(\rho_l + \rho_g)}{2}$, where l and g indicate liquid and gas phases. The macroscopic properties can be obtained by:

$$\begin{aligned}
\rho_0 &= \sum_\alpha f_\alpha + \frac{1}{2} \mathbf{u} \cdot \nabla \rho c_s^2 \\
\rho \mathbf{u} &= \sum_\alpha \frac{f_\alpha \mathbf{e}_\alpha}{c_s^2} + \frac{1}{2} \delta t \mathbf{F}
\end{aligned} \tag{43}$$

The relationship of the local density and local relaxation parameter with the local order parameter at each point is defined as:

$$\begin{aligned}
\rho &= \rho_l + \phi (\rho_l - \rho_g) \\
\tau &= \tau_l + \phi (\tau_l - \tau_g)
\end{aligned} \tag{44}$$

Using the Chapman-Enskog expansion, the following macroscopic equations can be recovered [76]:

$$\frac{\partial \rho_0}{\partial t} + \rho \nabla \cdot \mathbf{u} = 0 \quad (45)$$

$$\frac{\partial(\rho \mathbf{u})}{\partial t} + \nabla \cdot (\rho \mathbf{u} \otimes \mathbf{u}) = -\nabla p + \nabla \{ \mu [\nabla \mathbf{u} + (\nabla \mathbf{u})^T] \} + \mathbf{F} \quad (46)$$

3.6. Cellular Automaton Model for Dendritic Growth

A CA algorithm was used to track the solid-liquid interface, as explained in Ref. [63,104–106]. In the CA model, the simulation domain is divided into quadrilateral cells. Each cell is defined by several variables, such as crystallographic orientation, temperature, solute concentration, and volume fraction of solid, f_s . The volume fraction of solid describes the state of the cell, i.e. liquid $f_s=0$, solid $f_s = 1$, or interface $0 < f_s < 1$ [53]. It is assumed that the dendritic growth is driven by the difference between local equilibrium solute concentration, C_l^* , and the local actual solute concentration, C_l [104]. C_l^* is defined as:

$$C_l^* = C_0 + \frac{T - T_l^{eq} + \Gamma K_s}{m_l} \quad (47)$$

Γ is the Gibbs–Thomson coefficient and T_l^{eq} is the equilibrium liquidus temperature at the initial solute concentration. ,

$$K_s = K [1 - 15 \varepsilon \cos[4(\xi - \theta_0)]] \quad (48)$$

ξ is growth angle and θ_0 is the preferential growth orientation with respect to the x-axis and K is the interface curvature. The growth angle ξ is defined as the angle between the normal to interface and the x-axis.

$$\xi = \left\{ \begin{array}{l} \cos^{-1} \left(\frac{\frac{\partial f_s}{\partial x}}{\left(\left(\frac{\partial f_s}{\partial x} \right)^2 + \left(\frac{\partial f_s}{\partial y} \right)^2 \right)^{\frac{1}{2}}} \right) \frac{\partial f_s}{\partial x} \geq 0 \\ 2\pi - \cos^{-1} \left(\frac{\frac{\partial f_s}{\partial x}}{\left(\left(\frac{\partial f_s}{\partial x} \right)^2 + \left(\frac{\partial f_s}{\partial y} \right)^2 \right)^{\frac{1}{2}}} \right) \frac{\partial f_s}{\partial x} < 0 \end{array} \right\} \quad (49)$$

The interface curvature, K , can be computed using the solid fraction gradients:

$$K = \left[\left(\frac{\partial f_s}{\partial x} \right)^2 + \left(\frac{\partial f_s}{\partial y} \right)^2 \right]^{-\frac{3}{2}} \times \left[2 \frac{\partial f_s}{\partial x} \frac{\partial f_s}{\partial y} \frac{\partial^2 f_s}{\partial x \partial y} - \left(\frac{\partial f_s}{\partial x} \right)^2 \frac{\partial^2 f_s}{\partial y^2} - \left(\frac{\partial f_s}{\partial y} \right)^2 \frac{\partial^2 f_s}{\partial x^2} \right] \quad (50)$$

In the 3D model, the K_s is defined as [107]:

$$K_s = (3\varepsilon - 1)(\partial_x n_x + \partial_y n_y + \partial_z n_z) - 48\varepsilon(n_x^2 \partial_x n_x + n_y^2 \partial_y n_y + n_z^2 \partial_z n_z) + 12\delta Q(\partial_x n_x + \partial_y n_y + \partial_z n_z) + 12\varepsilon(n_x \partial_x Q + n_y \partial_y Q + n_z \partial_z Q) \quad (51)$$

Here \hat{n} is a unit vector perpendicular to the solid/liquid interface with the

components $n_x = \partial_x f_s / |\nabla f_s|$, $n_y = \partial_y f_s / |\nabla f_s|$ and $n_z = \partial_z f_s / |\nabla f_s|$, where $|\nabla f_s| =$

$\sqrt{(\partial_x f_s)^2 + (\partial_y f_s)^2 + (\partial_z f_s)^2}$ and $Q = n_x^4 + n_y^4 + n_z^4$ [108].

The change in the fraction of solid at each node (Δf_s) in each timestep depends on the actual liquid concentration C_l and the local interface equilibrium solute concentration C_l^* , and can be obtained by:

$$\Delta f_s = \frac{(C_l^* - C_l)}{(C_l^*(1 - k))} \quad (52)$$

Where k is the partitioning coefficient. The amount of solute rejected from solidifying cells to interface and surrounding melt at each time step due to the difference in solubility in melt and the solid phase is defined as:

$$\nabla C_l = (1 - k)\Delta f_s \quad (53)$$

3.7. Allen-Cahn Phase Field Model for Dendritic Growth

We employed a quantitative PF model developed by Echebarria et al. [109] to simulate the microstructural pattern formation. In the PF model, a phase field variable, ϕ , is introduced to distinguish between solid ($\phi = +1$) and liquid ($\phi = -1$) at a fixed node in each time step. The dimensionless supersaturation, U , related to the solute concentration, and the additional supersaturation parameter related to temperature, U' , are defined as:

$$U = \frac{(C_l - C_l^e)}{(C_l^e - C_s^e)} \quad (54)$$

$$U' = \frac{T - T_M - m_l C_l}{m_l C_0 \left(\frac{1}{k} - 1\right)} \quad (55)$$

The ratio of the solute concentration in the solid and in the liquid is defined as the partition coefficient, $k = C_s/C_l = C_s^e/C_l^e$, where C_l is the concentration in the liquid, and C_l^e , and C_s^e are the equilibrium concentrations in the liquid and solid, respectively. C_0 is the solute concentration far from the S/L interface which is equal to the initial concentration.

The time evolution of the phase field variable, ϕ , is given as:

$$\begin{aligned}
\tau a_s^2(n) \frac{\delta \phi}{\delta t} = & \frac{\partial}{\partial x} \left(|\nabla \phi|^2 a_s(n) \frac{\partial a_s(n)}{\partial \phi_x} \right) + \frac{\partial}{\partial y} \left(|\nabla \phi|^2 a_s(n) \frac{\partial a_s(n)}{\partial \phi_y} \right) \\
& + \frac{\partial}{\partial z} \left(|\nabla \phi|^2 a_s(n) \frac{\partial a_s(n)}{\partial \phi_z} \right) + \nabla \cdot (a_s^2(n) \nabla \phi) + \phi - \phi^3 \\
& - \lambda (1 - \phi^2)^2 (U + U')
\end{aligned} \tag{56}$$

The relaxation time is constructed as:

$$\tau = \tau_0 (1 - (1 - k)(U + U')) \tag{57}$$

where τ_0 is a constant called the phase field relaxation time defined as $\tau_0 = a_2 \lambda W_0^2 / d_0$.

The coupling constant, λ , is defined as $\lambda = a_1 W_0 / d_0$, where W_0 is the interface thickness, $a_1 = 0.8839$ and $a_2 = 0.6267$ are constants, and d_0 is the chemical capillary length defined as: $d_0 = \Gamma / (|m_l|(1/k - 1)C_0)$.

Anisotropy in Equation (56) is introduced as:

$$a_s(n) = 1 - 3\epsilon_4 - 4\epsilon_4 \frac{\phi_{\bar{x}}^4 + \phi_{\bar{y}}^4 + \phi_{\bar{z}}^4}{(\phi_{\bar{x}}^2 + \phi_{\bar{y}}^2 + \phi_{\bar{z}}^2)^2} \tag{58}$$

where ϵ_4 is the strength of anisotropy and $(\bar{x}, \bar{y}, \bar{z})$ corresponds to $\langle 100 \rangle$ direction in the material coordinate system. The Ni-based superalloy solidifies into a face center cubic crystal structure (FCC), which results in an octahedral grain morphology. The diagonal of the octahedral is assigned to the material direction $\langle 100 \rangle$ [110]. However, the material coordinate system and local coordinate system are not necessarily aligned. The differentiation of ϕ with respect to $(\bar{x}, \bar{y}, \bar{z})$, $\bar{\nabla} \phi$, is obtained by the following coordinate transformation using the Euler angles $(\varphi_1, \Phi, \varphi_2)$ with three subsequent rotations. The angles are commonly denoted as φ_1 , Φ and φ_2 where $\varphi_1 \in [0, 2\pi)$, $\Phi \in [0, \pi)$ and $\varphi_2 \in [0, 2\pi)$. The final transformation is written as:

$$\begin{pmatrix} \phi_{\bar{x}} \\ \phi_{\bar{y}} \\ \phi_{\bar{z}} \end{pmatrix} \quad (59)$$

$$= \begin{bmatrix} \cos\varphi_2 & \sin\varphi_2 & 0 \\ -\sin\varphi_2 & \cos\varphi_2 & 0 \\ 0 & 0 & 1 \end{bmatrix} \begin{bmatrix} 1 & 0 & 0 \\ 0 & \cos\Phi & \sin\Phi \\ 0 & -\sin\Phi & \cos\Phi \end{bmatrix} \begin{bmatrix} \cos\varphi_1 & \sin\varphi_1 & 0 \\ -\sin\varphi_1 & \cos\varphi_1 & 0 \\ 0 & 0 & 1 \end{bmatrix} \begin{pmatrix} \phi_x \\ \phi_y \\ \phi_z \end{pmatrix}$$

The transformed $\phi_{\bar{x}}$, $\phi_{\bar{y}}$, and $\phi_{\bar{z}}$ are used in Equation (58) to calculate the anisotropy of the rotated dendrite. The phase field equation, Equation(56), is solved with the finite difference method. The temporal discretization is based on the first-order Euler method while second-order central difference method is applied for spatial discretization.

CHAPTER IV

MODEL VALIDATION

4.1. Validation of Shan-Chen Based Model with Phase Separation

The phase separation between the liquid and vapor phases of an initial mixture of both phases was studied in this section. The domain was initially at rest with an average density plus a random variation in all nodes. All boundary conditions were periodic. The system was unstable based on EOS, and phase separation occurred. The final shape of bubbles or drops was circular since the free energy of the domain tends to minimize, and a circle has the minimum surface area compared to other shapes.

The problem was simulated by the enhanced model in six different cases. In each case, the initial density of the mixture was different, and a random variation in the order of 0.01 was added to the density. The temperature was selected as $T = 0.9T_{cr}$ which corresponds to a density ratio of 6.

Based on the value of G_1 and G_2 in Table 3, different scenarios of phase separation occurred as shown in Figure 15. For larger G_2 , corresponding to a bigger repulsive force, the coalescence of the drops was prevented in some of the cases. These results are in agreement with Ref. [102], which simulated the same problem. One difference with the simulations of Ref. [102] is that they used the original Shan-Chen EOS while the more realistic C-S EOS was used in this dissertation. However, since the

density ratio was almost the same in this dissertation as the one in Ref. [102] (six here and five in Ref. [102]), the results can be compared directly. The results show that the midrange-repulsive force can be used to prevent the coalescences of drops, but not bubbles. In the case of bubbles, this method only delays the merging process, but, eventually, just one bubble remains in the domain. For case (a) and (b), one bubble was present in the domain. However, for other cases, the formation of drops was observed. The formation of bubble or drops was related to the initial density. If the initial density is larger than a critical value, after some iterations, only one bubble will result in the whole domain.

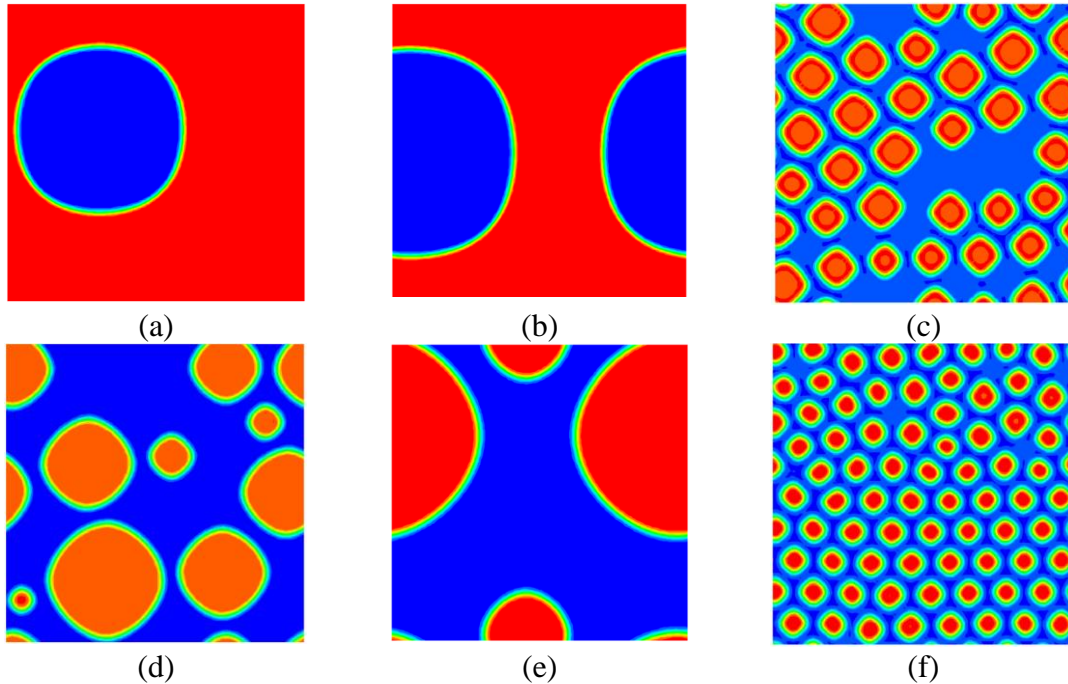


Figure 15. Results after 30,000 iterations for different values of G_1 and G_2 based on the values in Table 3 at $T=0.9T_{cr}$. (a) case 1, (b) case 2, (c) case 3, (d) case 4, (e) case 5, (f) case 6. (Blue: gas, red: liquid).

Table 3. Parameters used in the simulation.

	G_1	G_2	$\rho_{initial}$
Case1	-1.4	1.00	0.20
Case2	-1.4	1.00	0.170
Case3	-1.4	1.00	0.130
Case4	-1.4	0.95	0.130
Case5	-1.4	0.90	0.130
Case6	-1.4	1.00	0.117

As mentioned before, the enhanced model reduced the spurious current, but even this reduced amount of spurious current was too large for modeling phenomena, such as Marangoni convection, in this scale. The maximum amount of spurious current was observed in the interface between the bubbles and liquid, which is the place where the Marangoni force is exerted. The magnitude of the spurious current is presented in Table 4, showing approximately one order of magnitude reduction of the spurious current in the enhanced Shan-Chen model with respect to the original one, but still a large value at 5×10^{-3} . On the other hand, when this same problem was simulated with the phase field lattice Boltzmann method, the generated spurious current was in the order of 10^{-6} , which is acceptable for most cases of buoyancy and Marangoni flows [31].

Table 4. The spurious current magnitude and normalized total time in the original Shan-Chen and the enhanced model.

	Spurious Current	Normalized Total CPU Time
original Shan-Chen	0.03	1
The enhanced model	0.005	2.49

The total computational time of the simulation was also a critical parameter. The simulation time was non-dimensionalized with the time needed to solve the original Shan-Chen model. In Table 4, it is observed that the model enhancements make it about 250% more expensive in CPU time than the original Shan-Chen model.

4.2. Validation of Cahn-Hilliard Phase Field Model with Contact Angle

To model any desired contact angle, we follow the method proposed by Yiotis et al.[111]. In the model, it is assumed that the solid phase is made up of rigid bodies with a specific density of ρ_w . The specific density, ρ_w , is only an auxiliary parameter for modeling contact angle and is not related to the actual physical density of the solid. Based on this model, any contact angle from 0° to 180° can be simulated when ρ_w is selected in the range between ρ_g and ρ_l . The specific density, ρ_w , is corresponding to the solid local order parameter, ϕ_w , based on rearranging of Equation (44), as: $\phi_w = \frac{(\rho_w - \rho_l)}{(\rho_g - \rho_l)}$. In other words, by specifying ϕ_w in a range between 0 ($\rho_w = \rho_l$) and 1 ($\rho_w = \rho_g$), any contact angle from 0° to 180° can be modeled.

The ϕ_w for the solid phase is incorporated in the CH equation through Neumann boundary condition. In this method, there is no need to add any new term to chemical potential to consider the effects of the solid wall. The chemical potential at the wall nodes is simply calculated as $\mu_w = 4\beta \phi_w (\phi_w - 0.5)(\phi_w - 1) - \kappa \nabla^2 \phi$. Although seemingly a crude estimate to model the contact angle with only ϕ_w parameter, the model can

successfully predict both static contact angle and contact line dynamics regarding receding and advancing contact angle [112,113].

The ability of the LB-PF method to simulate different static contact angles was tested as shown in Figure 16. The domain size for all cases was 120×60 , while periodic boundary condition was applied on the left and right boundaries and no-slip boundary condition was implemented for the top and bottom boundaries. A semi-circle droplet with $R = 25 \text{ lu}$ (lattice units) was initially placed at the middle of the bottom wall. For CH equation, the boundary conditions for bottom and top walls were $\phi = \phi_w$. Initially, for the nodes inside the drop, the local order parameter is set to 1, and for other nodes inside the bubble, it is set to 0. The periodic boundary condition was applied on the left and right boundaries for the CH equation. The simulation parameters were selected as $\tau_l = 1$, $\tau_g = 1$, $\lambda = 0.1$ and $\rho_l/\rho_g = 3$. Different contact angles are achieved by changing ϕ_w for bottom and top walls. Figure 16 shows the equilibrium contact angle after 20000 iterations. The calculated contact angles were 40° , 105° and 130° corresponding to $\phi_w = 0.7, 0.4$, and 0.3 , respectively. Details of contact angle measurements can be found in [114].

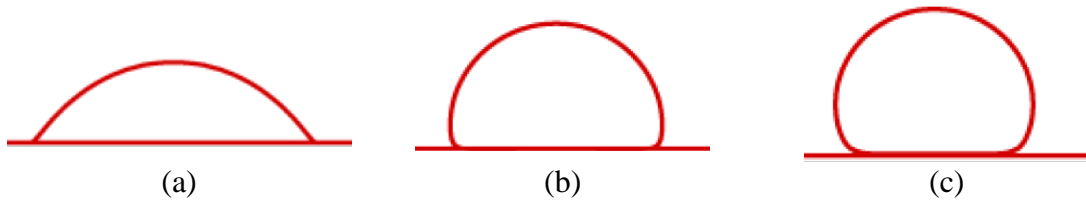


Figure 16. Contact angle validation for PF model for initially semi-circle droplet. Different contact angles were simulated by changing the order parameter, ϕ_w 0.7, 0.4, and 0.3 for top and bottom walls as a boundary condition, resulting in the contact angles 40° , 105° , and 130° , after 20000 iterations.

More cases were simulated by manipulating the order parameter, ϕ_w . The relationship between the order parameter and the equilibrium contact angle is plotted in Figure 17, which turns out to be almost linear. The figure verifies that any contact angle can be modeled by changing ϕ_w in the range 0-1.

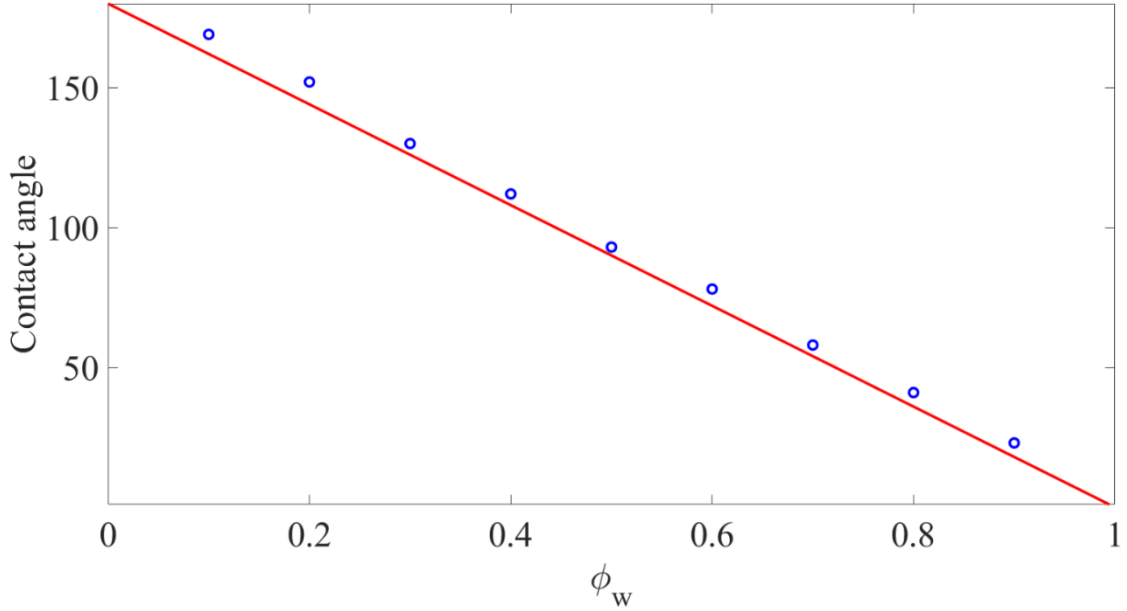


Figure 17. The contact angle as a function of ϕ_w . The simulation results are shown with blue circles, while the solid line connects $(0, 180^\circ)$ and $(1, 0^\circ)$ as a guide.

4.3. Validation of Cahn-Hilliard Phase Field Model with Rayleigh Instability

The Rayleigh instability benchmark is defined as a case when a denser fluid with density ρ_l is placed over a less dense fluid with density ρ_g . The hybrid LB-PF model was validated by simulating the Rayleigh instability problem for different density ratios.

An important dimensionless parameter for modeling this problem is At number which represents the density ratio between phases as: $At = (\rho_l - \rho_g) / (\rho_l + \rho_g)$. The problem was defined in a domain with a dimension size of $L \times 4L$, where L is the number

of nodes in x direction. Also, a 10% initial perturbation was set at the interface of lighter and heavier fluids in the middle of the domain. This perturbation can be defined as $y = 2L + 0.1L\cos\left(\frac{2\pi x}{L}\right)$ [72]. Periodic boundary conditions were imposed on the left and right boundaries while no slip boundary condition (bounce back) was applied to the bottom and top boundaries. The characteristic velocity and Reynold number were respectively defined as: $U = \sqrt{gL}$, and $Re = UL/\nu$.

For the first case, the domain size was selected as 128×512 with $Re = 256$. The At number was set to 0.5 which corresponds to a density ratio of three. A characteristic velocity $U=0.04$ in LB unit was adopted which corresponds to kinematic viscosity $\nu = 0.02$. The results are reported in non-dimensional time units, which is normalized by $\sqrt{L/g}$. Figure 18 presents the location of the interface during the simulation. The results are in good qualitative agreement with the benchmark solution reported in Ref.[76].

To validate the results quantitatively, the spike tip and bubble front locations were measured and compared with previously published studies. As shown in Figure 19(a), the location of spike and bubble tip were in good agreement with the results of He et al. [67].

The model was also validated for the same problem but with a density ratio of 1000 which corresponds to $At=0.999$. The Reynolds number is kept at $Re=256$. The characteristic velocity was set to $U=0.1$. The evolution of the interface is shown in Figure 20, which is consistent with previously published results [72]. The plume shape strongly depends on the density ratio. Comparing Figure 20 and Figure 18, one may conclude that for small density ratios, there is a bigger tendency of mixing between the two fluids.

However, a more coherent structure was observed for larger density ratios. The bubble and spike locations were also compared and presented in Figure 19(b).

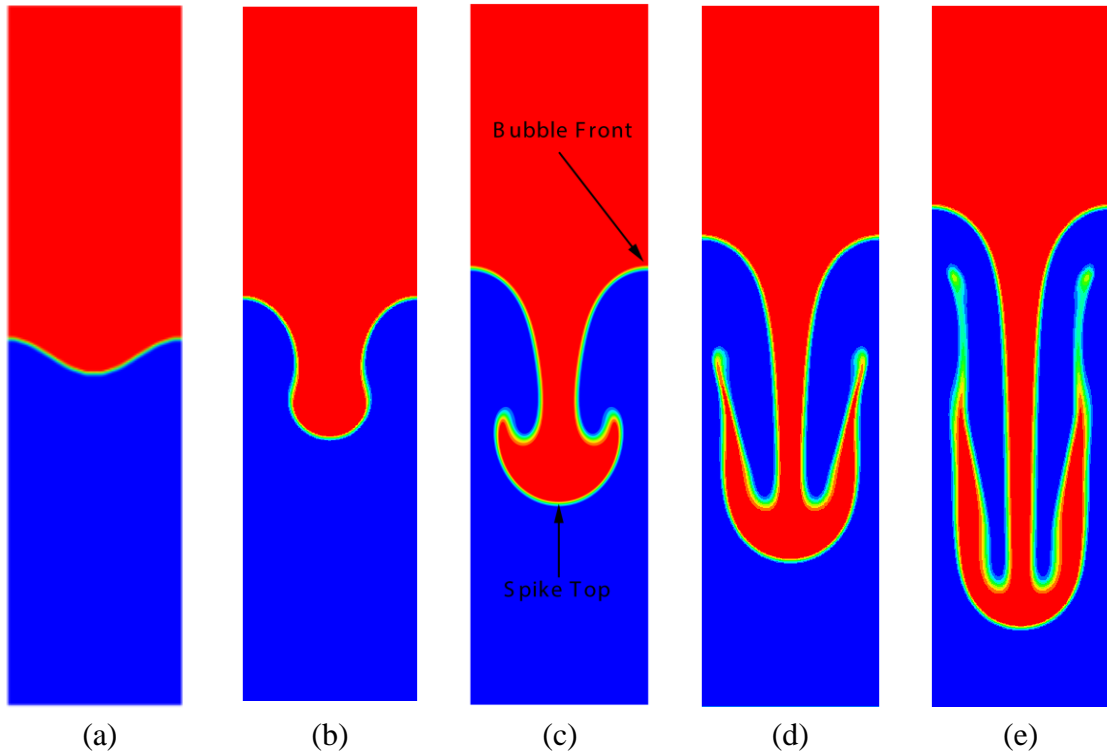


Figure 18. Interface evolution during simulation for $At=0.5$ and $Re=256$ at (a) $t=0$, (b) $t=2$, (c) $t=3$, (d) $t=4$, and (e) $t=5$.

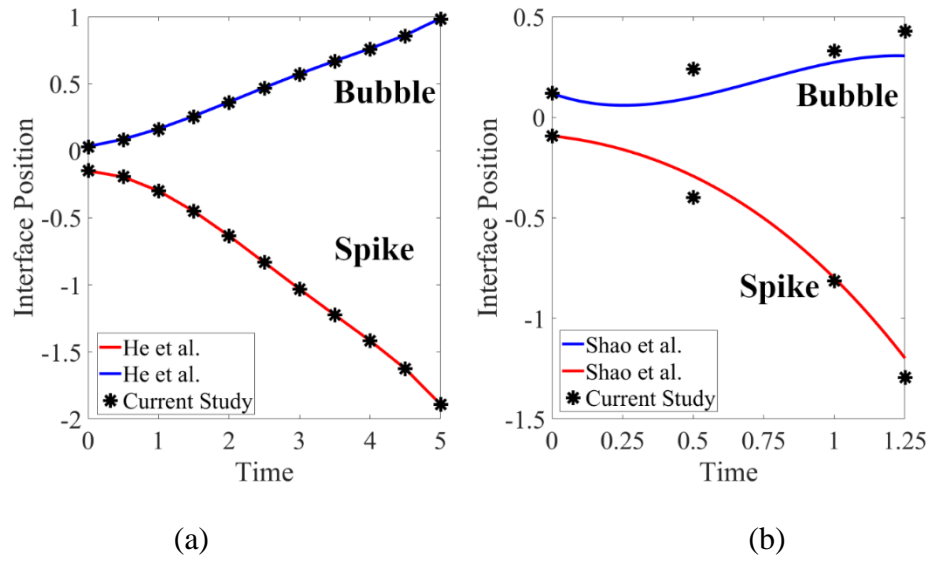


Figure 19. Comparison of spike and bubble position in (a) $At = 0.5$ and $Re = 256$ with He et al. (1999) results, (b) $At = 0.999$ and $Re = 256$ with Shao et al. [72] results. All of the parameters are non-dimensional.

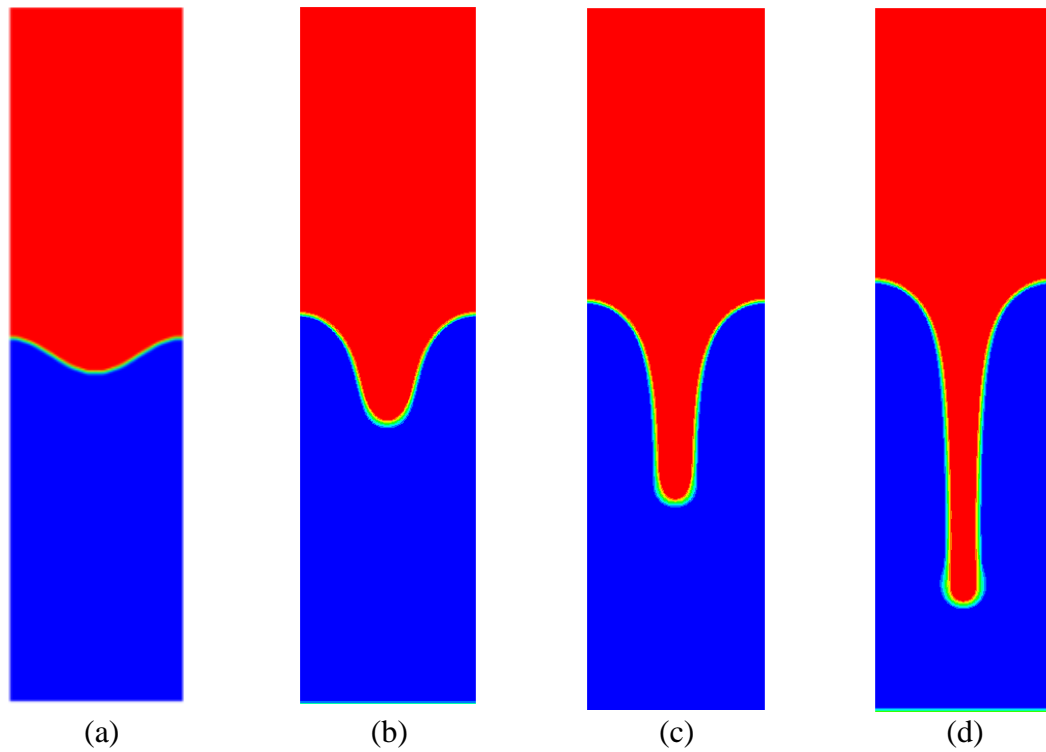


Figure 20. Interface evolution for density ratio of 1,000 ($At = 0.999$) and $Re = 256$ at (a) $t = 0$, (b) $t = 0.5$, (c) $t = 1$, and (d) $t = 1.25$.

4.4. Validation of Cahn-Hilliard Phase Field Model with Marangoni Convection Around a Bubble

In Marangoni convection, fluid flow is induced due to the change of interface surface tension with temperature. In the simplest form, the relation between interface surface tension with temperature is considered linear and can be written as:

$$\sigma(T) = \sigma_0 + \gamma(T - T_0) \quad (60)$$

Where $\gamma = \frac{\partial\sigma}{\partial T}$ (temperature coefficient of surface tension) is negative for most material. σ_0 and T_0 are the reference surface tension and the reference temperature, respectively. Young et al. [38] derived an analytical solution for the thermocapillary migration of bubbles in an infinite domain with fixed temperature gradient:

$$U_{YGB} = \frac{2U}{(2 + 3\tilde{\eta})(2 + \tilde{k})} \quad (61)$$

$\tilde{\eta}$ and \tilde{k} are viscosity and thermal conductivity ratios of fluid and bubble, respectively. Here U is the characteristic velocity that is introduced by the balance between the thermocapillary and viscous forces:

$$U = -\frac{\gamma|\nabla T_\infty|R}{\mu_2} \quad (62)$$

Where ∇T_∞ is the fixed constant temperature gradient and R is the bubble radius, which is considered as the characteristic length to define Reynolds and Marangoni numbers. The Marangoni number, Ma, is defined as:

$$Ma = Re \times Pr = \frac{-\gamma|\nabla T_\infty|R^2 Pr}{\rho\nu_2^2} \quad (63)$$

R is the bubble radius and ∇T_∞ is the fixed constant temperature gradient. For the bubble with a diameter of 1.3 mm and material properties given in Table 1, the Ma number was calculated to be 60.5.

For validation purposes, a cavity of $8R$ width and $16R$ height was considered with a bubble of $R = 20$ lu inserted at the center of the domain. The bottom and top boundary conditions were considered as no slip, while periodic boundary condition was applied for the right and left sides. A linear temperature profile varying from 0 at the bottom wall to 32 at the top wall ($|\nabla T_\infty| = 0.1$) was applied. The other parameters are listed Table 5.

Table 5. Parameters used for simulation of the Marangoni benchmark problem. All values are listed in lattice units.

Pr No	$v_{bubble} = v_{fluid}$	γ	σ_{ref}	\tilde{k}	$\tilde{\eta}$
1	0.2	-10^{-4}	2.5×10^{-3}	1	1

The characteristic velocity, analytical migration velocity, Marangoni, and Reynold numbers can be calculated as $U = 0.001$, $U_{YGB} = 1.33\bar{3} \times 10^{-4}$, $Ma = Re = 01$, respectively. Figure 21 demonstrates the velocity field around the bubble. The shear stress at the interface induces a flow in both fluid and the bubble. Since the temperature coefficient of surface tension is negative, the warmer fluid is pulled down along the melt/bubble interface (from lower surface tension to higher surface tension). However, the shear stress inside the bubble causes a net force in the positive y direction pulling the bubble upward to the hot region. For the small Ma numbers, the temperature field remains almost linear, which is also reported by other researchers [103,115].

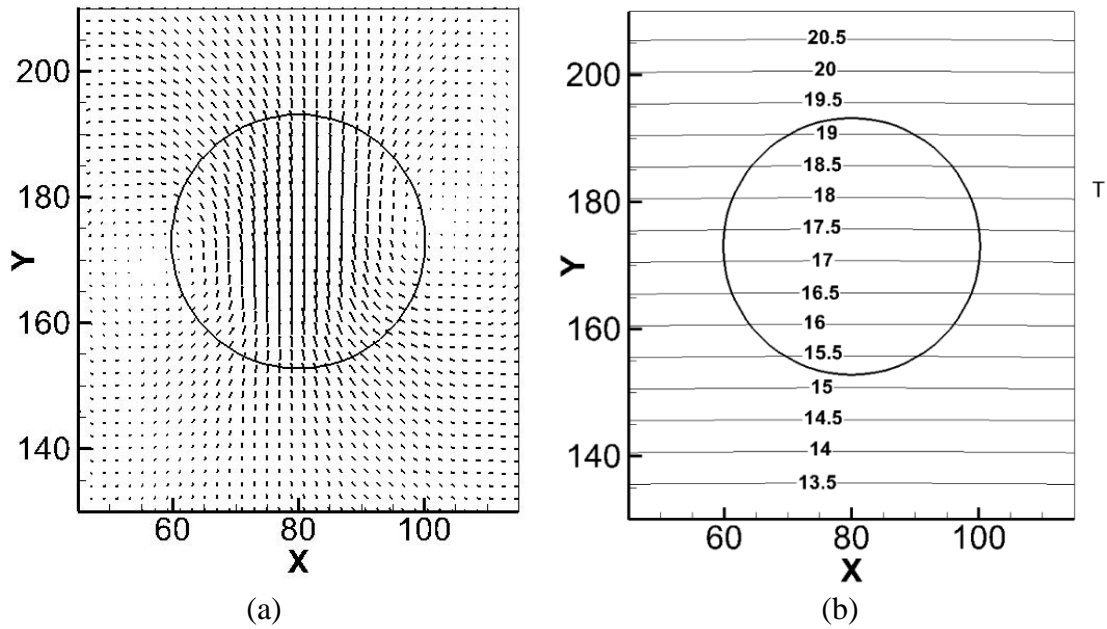


Figure 21. Steady state velocity (a) and temperature (b) distribution around the bubble.

Figure 22 compares the analytical and simulated values of bubble migration velocity. The simulation results converge to $U_M/U_{YGB} = 0.81$, which implies about 20% error. This error originates from the assumption used for deriving the formula. Equation (62) assumes a non-deformable spherical bubble in an infinite axis-symmetric domain. However, the numerical model considers a two-dimensional deformable bubble in a domain with periodic boundary conditions. Other researchers reported similar results obtained by different numerical methods [103,116,117].

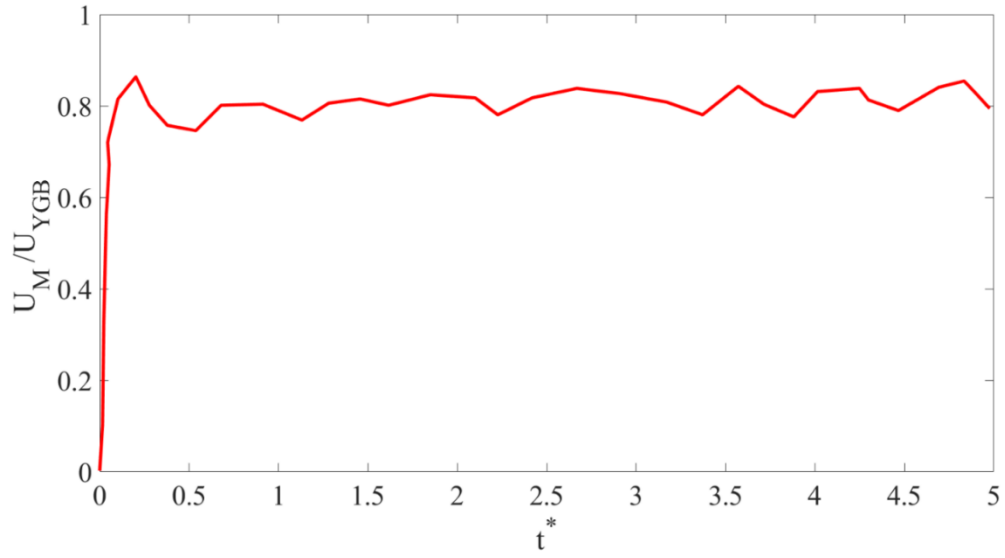


Figure 22. Bubble migration velocity normalized by analytical velocity versus normalized time. The time is non-dimensionalized by R/U .

4.5. Validation of CA Model with Free Dendrite Growth

To validate the dendritic growth model, free dendritic growth of SCN-0.24 wt% water binary alloy was simulated and compared with the LGK analytical model, proposed by Lipton et al. [118,119]. The model can predict the steady state tip velocity, tip radius and growth Peclet number as a function of undercooling. The temperature in the whole domain is assumed to be homogenous with the undercooling varying from 0.5 to 4 °C. A solid seed is initially inserted in the center of the domain with the preferred orientation of 0° with respect to x-axis.

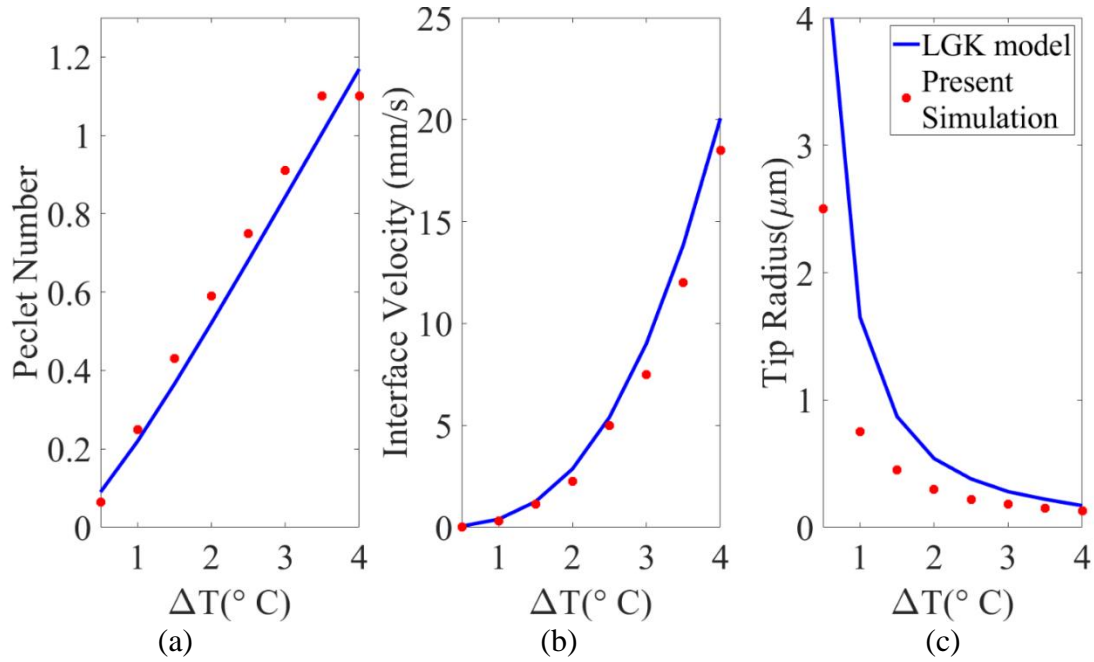


Figure 23. Comparison between the present model and LGK analytical model for (a) Peclet number, (b) interface velocity, and (c) tip radius at different undercoolings

The tip velocity is averaged at four primary arms after the initial transient stage.

The solute Peclet number is defined as $Pe_c = VR/2D$, where R and V are the tip velocity and tip radius, respectively. Figure 23(a) shows that the difference between the Peclet numbers calculated from the numerical and analytical models is small. The results are in good agreement for different undercoolings.

As in Figure 23(c), the error in predicting tip radius increases at low undercoolings. At low undercooling, the dendrite grows slowly, and its shape as simulated by the CA model deviates from the parabolic shape assumed in the LGK model, which results in a deviation from the LGK predictions. Nevertheless, the results are in the same order of magnitude and show the same trends.

4.6. Validation of Dendritic Growth of PFMI Experiment with Phase Field and Cellular Automaton Using Scalable GPU Programming

The columnar dendrite growth is governed by the solute transport equation and a model to track or capture the interface between solid/liquid (S/L). The lattice Boltzmann method was applied to solve the solute diffusion equation, while the CA or PF was employed to compute the evolution of the solidification interface. The simulations were performed using the Graphics Processing Unit (GPU).

The 2D domain was a $2 \times 1.1 \text{ mm}^2$ rectangle (Figure 24(a)). Three seeds were placed on the left wall, all with the crystallographic orientation of 0° from the x-axis, and the temperature gradient $G = 716 \text{ K/m}$ was imposed in the horizontal direction. The primary dendrite arm spacing was defined as $350 \text{ }\mu\text{m}$. The initial undercooling was calculated around 0.7K based on the PFMI experiment and imposed on the right wall.

The three-dimensional (3D) domain was a cuboid with a size of $1.1 \times 1 \times 0.6 \text{ mm}^3$ (Figure 24(b)). Initially, a constant undercooling of 0.7 K was imposed on the bottom wall, and a temperature gradient of $G = 716 \text{ K/m}$ was imposed in the vertical direction. The undercooling was determined based on the temperature profile in the PFMI experiment at the S/L interface during the experiment illustrated in Figure 6. Eight seeds were placed on the bottom wall with an identical crystallographic orientation of $[001]$ and average dendrite arm spacing of $350 \text{ }\mu\text{m}$.

A cooling rate of 0.1 K/s , same as the PFMI experiment, was applied to gradually cool down the domain. The computational domains and initial conditions for both 2D and 3D simulations are demonstrated in Figure 24.

The mesh size for each case was selected individually since the PF method needs a smaller grid size. The uniform initial solute concentration was 0.24 wt% in both cases. The physical properties of SCN-0.24 wt% water alloy used in the simulations are listed in Table 1.

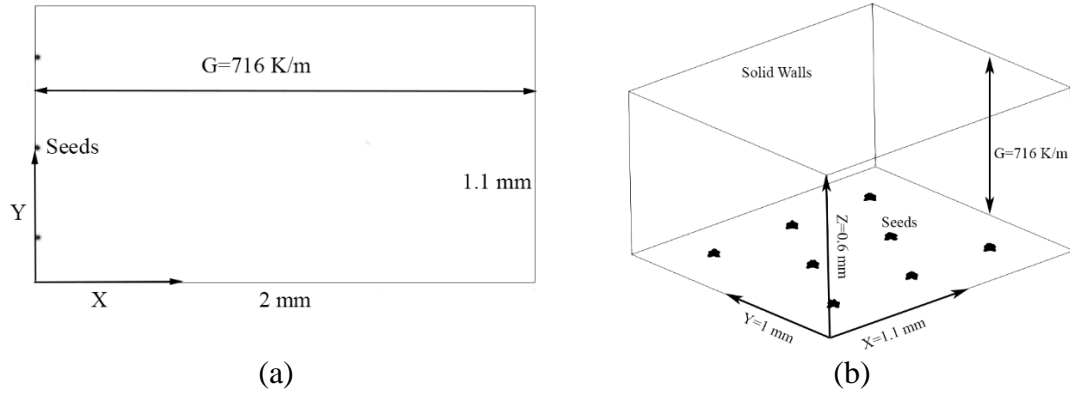


Figure 24. Schematics of the simulation domains: (a) 2D with the domain size of $1.1 \times 2 \text{ mm}^2$ (b) 3D with the domain size of $1.0 \times 1.1 \times 0.6 \text{ mm}^3$.

The problem defined in Figure 24 was solved with CA and PF methods for both 2D and 3D cases. The evolving morphologies in the 2D case for the two methods are demonstrated in Figure 25. The growth is driven by solute transfer in the constant temperature gradient along the x-direction.

The results of the CA method (Figure 25 (a-d)) show that secondary arms develop in the direction perpendicular to the primary arms. Microsegregation due to the entrapment of the solute was observed in the interdendritic region. The average tip velocity for the 2D case simulated by the CA method was calculated as $71.46 \text{ } \mu\text{m/s}$, whereas the 2D PF model it was around $68.95 \text{ } \mu\text{m/s}$. Both methods can capture the side branching of the dendrites. However, the distribution of the solute field obtained by CA and PF is not the same. The discrepancy can be explained by the discrete nature of the

advancement of the solid front in each model. This will eventually affect the amount of solute rejected from growing dendrites and result in different solute maps.

Figure 26 demonstrates the 3D morphologies simulated by the CA and PF methods. Both methods were capable of capturing secondary arms and microsegregation in the interdendritic region. While the overall morphology produced by the CA method is irregular with further side branching including secondary and tertiary arms, the resulted morphology from the PF method is more uniform. The difference between 2D and 3D results can be explained by the more effective diffusion in three dimensions. Also, for the CA model, calculating tip radius and curvature is more accurate in 3D compared to 2D; the calculation of curvature in the 2D deals with nine neighboring nodes while it considers 27 neighboring nodes in 3D. In the PF model, there is no need to calculate the curvature, since the phase field variable is a continuous function changing smoothly from -1 to 1 over the interface width.

Both 2D and 3D PF simulations require considerable computational resources, since the grid size is almost two times finer compared to the CA model. The time step required for the PF model was also smaller than the CA model. The grid size, time step size, and calculated tip velocity for all cases is shown in Table 6.

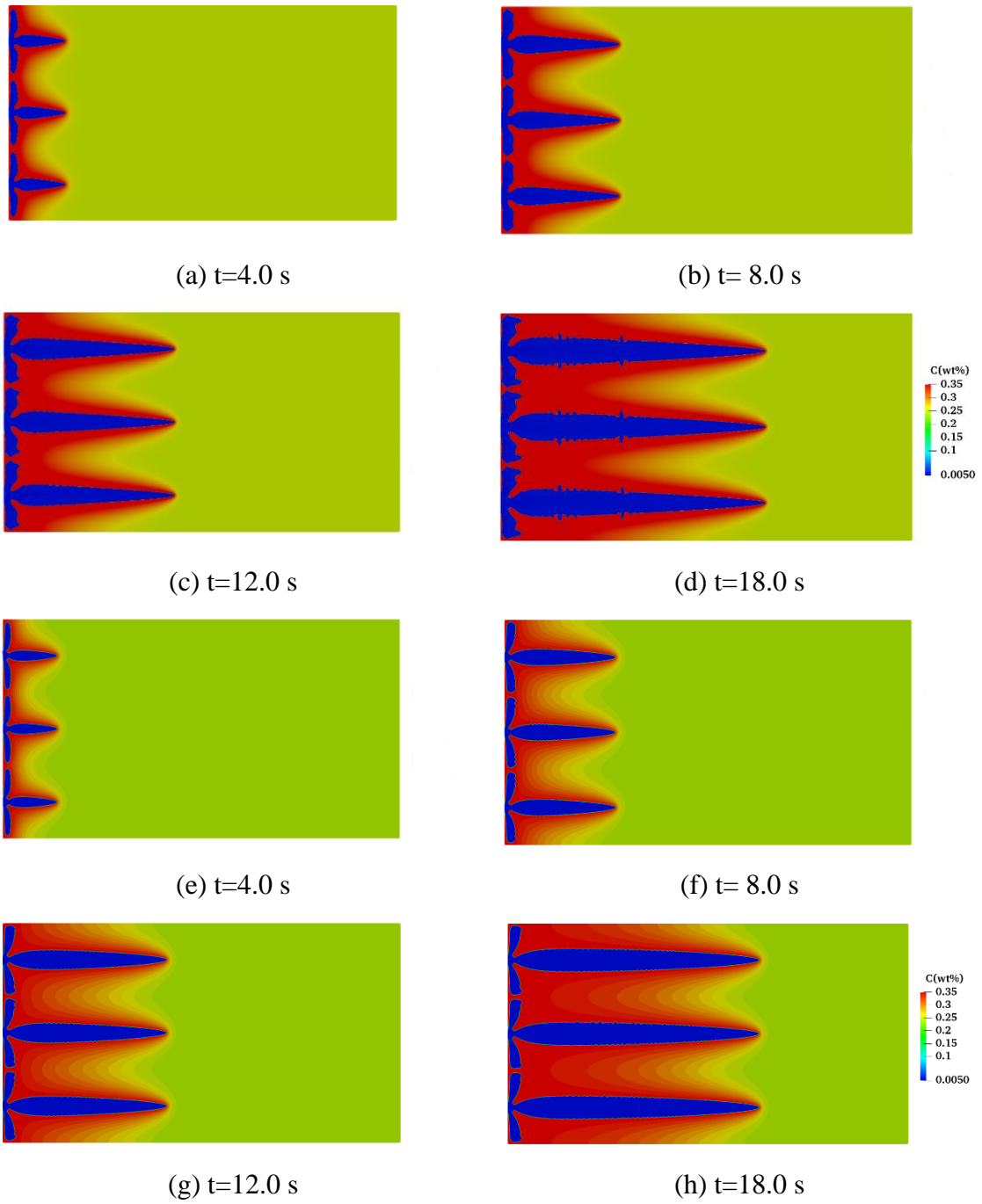


Figure 25. 2D simulation of dendritic morphologies at different times with cellular automata (a-d), and phase field (e-h) methods. The average growth rate for cellular automata and phase field methods at $t=18$ s were $71.46 \mu\text{m/s}$ and $68.95 \mu\text{m/s}$, respectively.

Table 6. Grid size, time step and calculated tip velocity for 2D and 3D simulations for cellular automata and phase field models.

	2D CA	3D CA	2D PF	3D PF	PFMI (left dendrites)	PFMI (right dendrites)
dx(μm)	1.0	2	0.6	1	N/A	N/A
dt(μs)	27.8	71.1	26.7	21.5	N/A	N/A
Average Tip Velocity($\mu\text{m/s}$) at t=4 s	73.49	93.1	69.07	121.4	84	103

The tip velocities resulting from both PF and CA simulations showed good agreement to velocity measured from the PFMI experiment. The simulated morphology looks different in CA and PF results. The calculation time also shows a significant difference between the models. While the 2D CA method took around 480 seconds, the 2D PF simulation took about 1368.21 seconds. For 3D cases, the difference was even more significant. The 3D CA method took about 7640 seconds, while for 3D PF it took around 125800 seconds. All of the simulations were performed on a single NVIDIA Tesla V100 32GB GPU. The computational times were measured after 4s of physical time for the 2D cases 3D cases.

Both PF and CA are suitable for parallel computing since they are both solved locally, and they do not require solving a global matrix in each time step. In general, CA methods need more moderate computational resources. However, the CA method suffers from artificial mesh anisotropy, as observed by many studies [44,120].

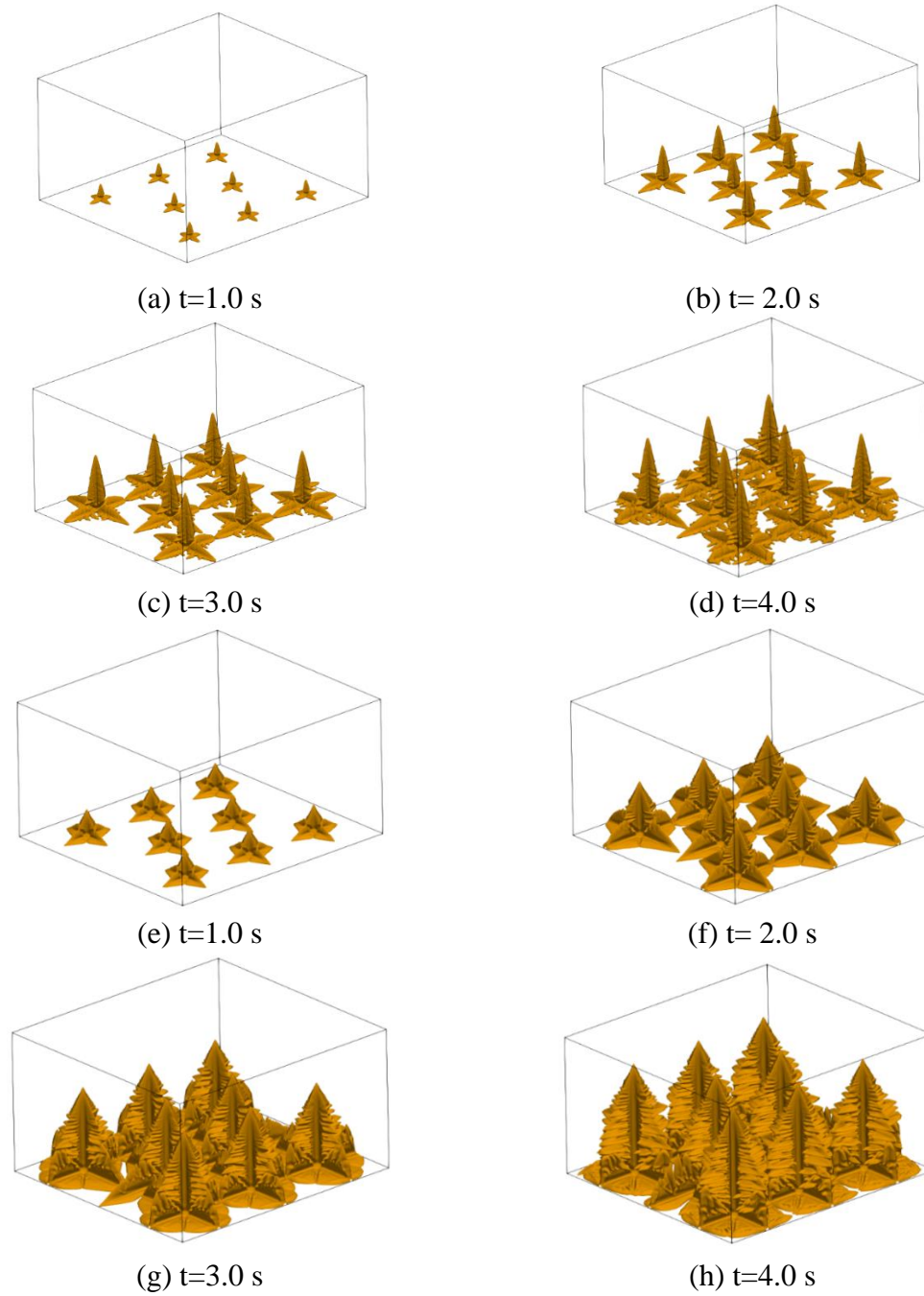


Figure 26. Evolution of 3D dendrites at different times simulated by cellular automata method (a-d) and phase field method (e-h). The average tip velocity was calculated to be $93.1 \mu\text{m/s}$ for cellular automata model and $121.4 \mu\text{m/s}$ for phase field model.

In both 3D and 2D simulations, the PF computational time was one order of magnitude larger compared to CA method. The 2D results of CA and PF methods look similar, whereas, in 3D simulations, the morphologies resulted from the PF simulations were different in shape compared to the CA results.

CHAPTER V

RESULTS

5.1. Columnar Dendritic Growth with Original Shan-Chen Model

The growth of five columnar dendrites in a rectangular domain was simulated using the original Shan-Chen model. The simulation was performed for Al-3 wt% Cu binary alloy with initial undercooling of $\Delta T = 2.0$ K. All the external boundary conditions were considered as stationary walls for the velocity field and insulated for the temperature field except for the left wall where a temperature gradient of 1200 K.m^{-1} was imposed. The boundary condition for the concentration field was assumed as insulated in all directions. The preferential crystallographic orientation was 0° with respect to the x-axis (horizontal). The domain size was $91.2 \mu\text{m} \times 72 \mu\text{m}$, discretized with 304×240 cells for solving fluid flow and solute transport equations, and 38×30 cells for solving the energy equation. Five columnar dendrites and 6 bubbles with a radius between $4 \mu\text{m}$ to $6 \mu\text{m}$ were initially placed in the domain. The contact angle was selected as 150° . Other parameters are shown in Table 7.

Since the focus of this section is to compare the ability of the original and enhanced Shan-Chen models to simulate dendrite-bubble interaction, the gas component rejection into the liquid phase during solidification was not considered in these simulations. The initial condition is depicted in Figure 27.

Table 7. Parameters used for dendritic growth with the original Shan-Chen Model [104,121].

Gibbs Thomson Coefficient (G)	2.4×10^{-7}
Domain size	$90 \mu\text{m} \times 90 \mu\text{m}$
$\Delta T_{\text{undercooling}}$	2K
Contact Angle	150°
Kinematic Viscosity	$5.66 \times 10^{-8} \text{ m}^2/\text{s}$
Solute Diffusivity	$3 \times 10^{-9} \text{ m}^2/\text{s}$
Thermal Diffusivity	$2.42 \times 10^{-5} \text{ m}^2/\text{s}$
Liquidus Slope (m_L)	-2.6 K/wt%
Partitioning Coefficient	0.17

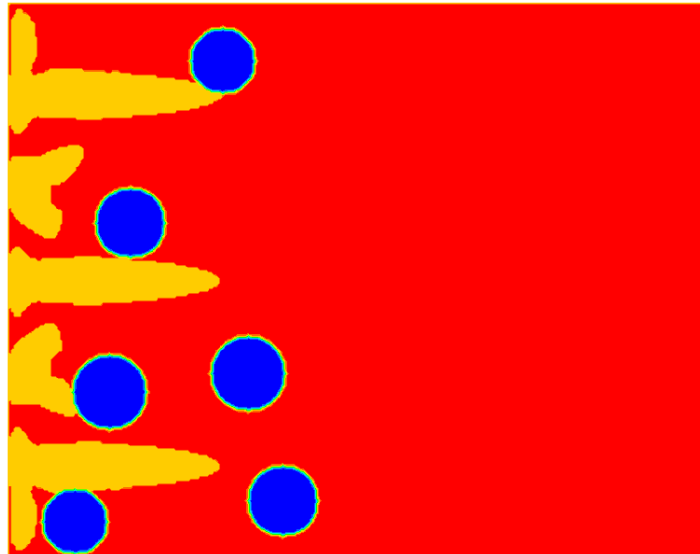


Figure 27. Initial condition for simulation of dendrite-bubble interaction (Yellow: solid, red: liquid, blue: gas). [122]

The interaction between dendrites and bubbles is shown in Figure 28. During the simulation, some bubbles tended to dissolve in the fluid or merge into other bubbles. This process made some bubbles bigger while eliminating the rest. The reason for this phenomenon is that the pressure of the bulk fluid was greater than the corresponding saturated value for the smaller bubbles. Therefore, these bubbles condensed. On the other hand, the pressure of the bulk fluid was lower than the saturated value of larger bubbles,

causing the larger bubbles to grow. This is related to the EOS and the fact that no repulsive force was present in the domain. Therefore, during the simulations, some bubbles became smaller or vanished, while others became larger.

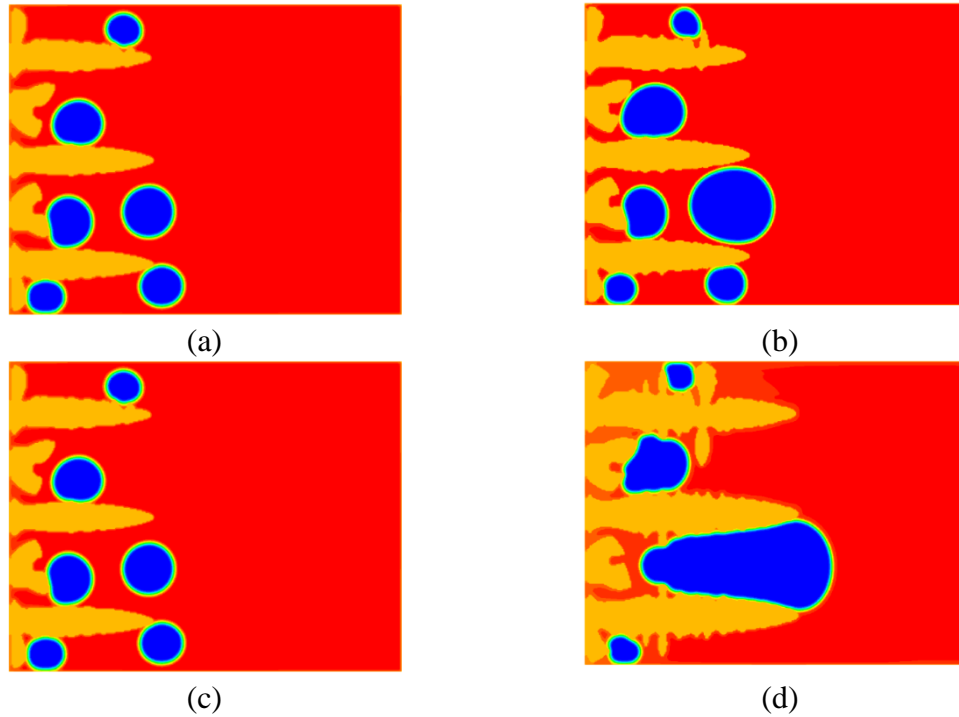


Figure 28. Results of original Shan-Chen model at time: (a) 0.0013, (b) 0.0026, (c) 0.00387, and (d) 0.0052 s for a density ratio of 4. (Yellow: solid, red: liquid, blue: gas).

The rate of bubble merging obtained with the original Shan-Chen model is not realistic as evidenced by experimental results. Coalescence of bubbles occurred in the experiments, but in a different time scale compared to what is presented in Figure 28. Based on the simulation results, all the small bubbles in the middle of the domain coalesced after 0.005 s while in the experiment, this phenomenon happened in the order of 10 s [3,123]. This model also generates a high spurious current, especially in the interface. The spurious current was in the order of 5 mm/s, which is very high and can completely mask the actual physical flow.

5.2. Dendritic Growth with the Enhanced Shan-Chen Model

The same problem of the previous section was modeled with the enhanced version of the Shan-Chen model. Since the enhanced model allows the simulation of higher density ratios, a density ratio of 40 was used for the results shown in Figure 29. The enhanced model also has the ability to control the coalescence of bubbles. The values used for the G parameters were $G_1 = -1.4$ and $G_2 = 1$.

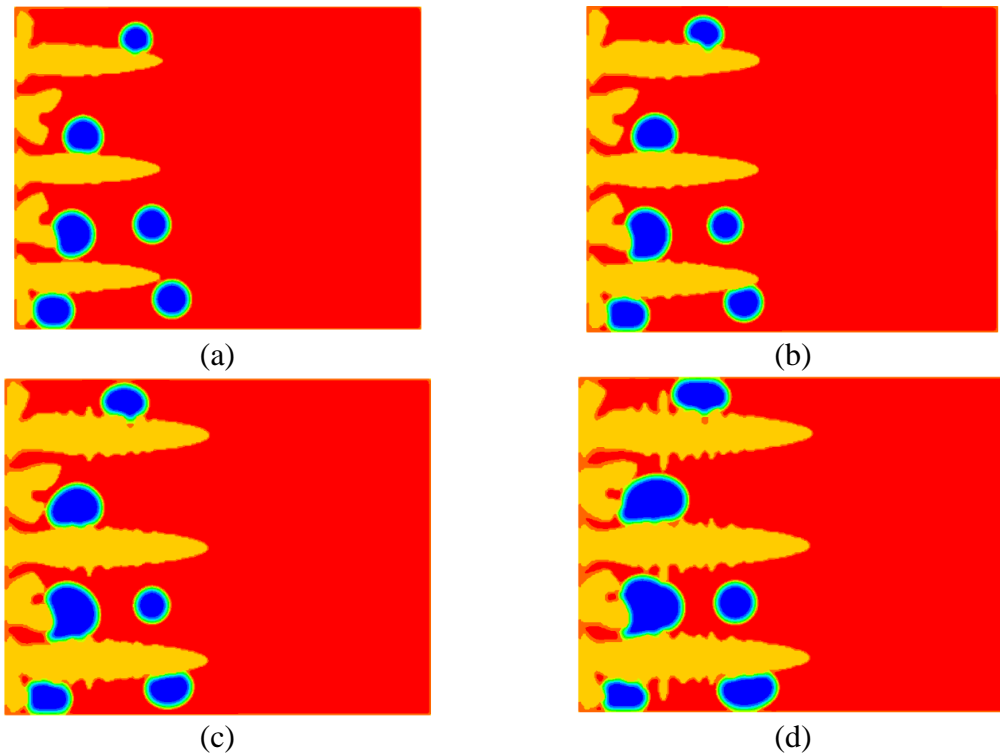


Figure 29. Results of the enhanced model at time (a) 0.0013, (b) 0.0026, (c) 0.00387, and (d) 0.0052 s for $T=0.7T_{cr}$, which corresponds to a density ratio of 40. (Yellow: solid, red: liquid, blue: gas).

The effect of the contact angle can be observed through the shape of bubbles that were in contact with dendrites. The magnitude of the spurious current in this simulation was about 3.5 mm/s, similar to the one obtained with the original model, but for a density

ratio 10 times smaller. As observed in the original Shan-Chen model, dissolution of small bubbles and growth of large bubbles was observed here as well. However, the rate of merging could be controlled by the parameters, G_1 and G_2 , giving the model the ability to reproduce physical results. The enhanced model clearly improved the results by reducing the spurious current and avoiding all bubbles coalescing together. The spurious current acted as a barrier for simulating higher density ratios. The enhanced model handled higher density ratios than the original model with a similar magnitude of spurious current. However, the spurious current was still too large in both models. Since the velocity and concentration fields were coupled, the high spurious current affected the concentration field and, consequently, the morphology of the dendrites and reliability of the results.

5.3. Columnar Dendrite Growth with Phase field

The same dendrite growth problem, as defined in Section 5.2., was solved with the phase field LB model. For comparison purposes, the density ratio was selected as 40 ($\rho_l = 1$ and $\rho_g = 0.025$) even though the phase field model can simulate much higher density ratios. The results are shown in Figure 30, for the same time values of Figure 28.

Unlike the Shan-Chen models, the dissolution and reappearance of bubbles related to the EOS were not observed in this model. Therefore, the size of the bubbles remained almost constant during the simulation. A small movement was observed for bubbles beyond the dendrite tips while the bubbles between dendrites were trapped and did not move.

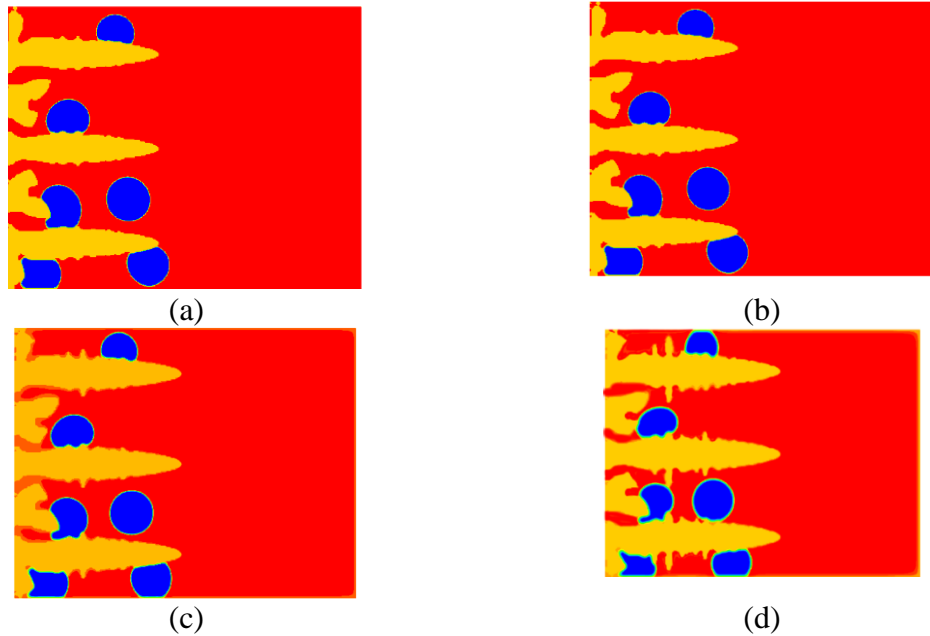


Figure 30. Results of the phase field model at time (a) 0.0013, (b) 0.0026, (c) 0.00387, and (d) 0.0052 s for a density ratio of 40. (Yellow: solid, red: liquid, blue: gas).

Table 8 summarizes the magnitude of the spurious current, the simulated density ratio, and the computational time. The original Shan-Chen model could only handle the density ratio of four while it diverged for the higher density ratios. The phase field method was capable of simulating much higher density ratios, but since the enhanced Shan-Chen model results diverged for the higher density ratios, the selected density ratio was 40 for both models. It can be observed that the original Shan-Chen model was the fastest model, but it produced an unacceptable large spurious current, even for a low density ratio. The phase field model was the most precise model, though at the expense of a significantly higher computational cost.

To compare the magnitude of the spurious current among all models, the velocity profile at $t = 0.0013$ s was plotted along the centerline of the domain in both the x and y-direction as shown in Figure 31.

Table 8. Comparison between different parameters among different LB models.

	Maximum Spurious Velocity (mm/s)	Density Ratio	CPU-Time (s)
Original Shan-Chen model	5	4	1527
The enhanced model	3.5	40	2351
The phase field model	0.03	40	35,861

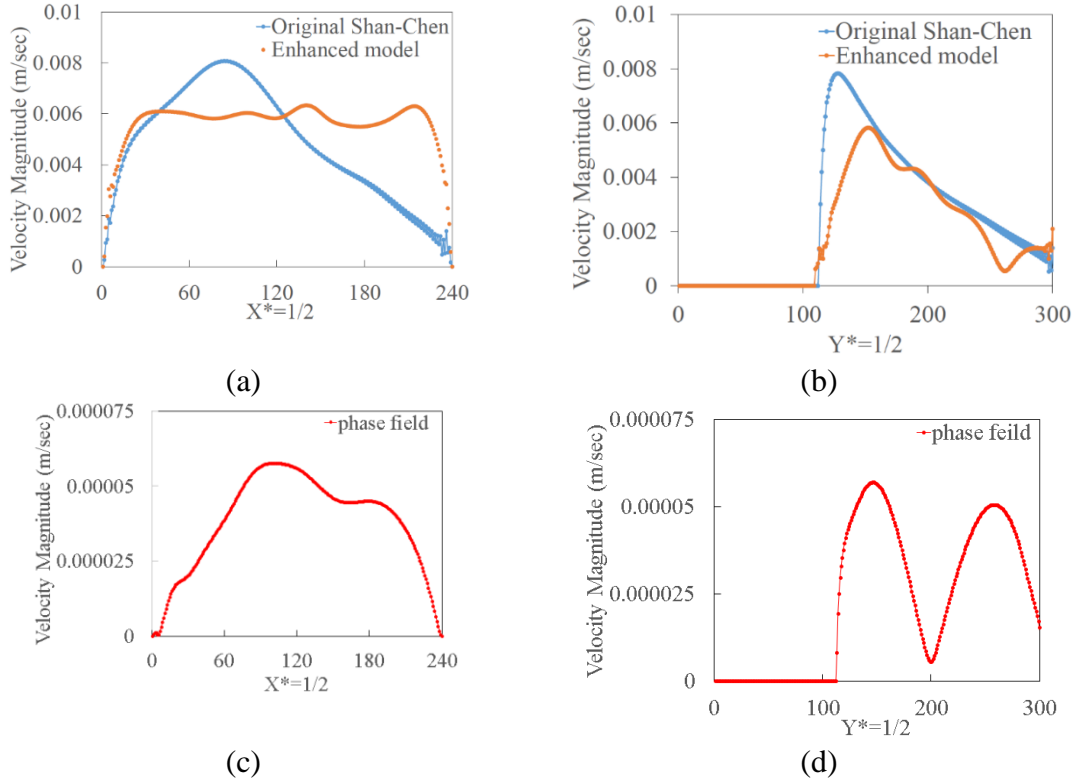


Figure 31. Velocity magnitude along the centerline in the width and height direction (a) $X^*=1/2$ Shan-Chen model, (b) $Y^*=1/2$ Shan-Chen model, (c) $X^*=1/2$ phase field, (d) $Y^*=1/2$ phase field, at $t = 0.0013$ s.

The velocity component was formed by the physical velocity and the spurious current. The reason for the existence of any physical velocity was related to the pressure difference throughout the domain, which was modeled in Shan-Chen models by the EOS and through Equation (43) in the phase field method. From the figure, it is observed that the magnitude of the spurious current was not constant in the whole section. The

maximum spurious current took place near the bubble/fluid interface in all the models i.e., in the bottom of the domain in Figure 31.(a), (c). As expected, the phase field method generated the least spurious current, in the order of 5×10^{-5} m/s.

To have a better understanding of the influence of the spurious current in the simulation, the results compared with PFMI experiment. Since the experiment took place in the space station, the only possible explanation for fluid flow is Marangoni convection. The average bubble velocity due to Marangoni convection in the experiment was in the order of 0.2 mm/s. In enhanced Shan-Chen simulation, the magnitude of spurious current for the density ratio of 40 was around 3.5 mm/s. This implies that the Shan-Chen models generate a high spurious current, which makes them useless to simulate Marangoni convection. Therefore, a phase field model should be utilized for this situation



Figure 32. The arrow shows the typical bubble path. (Courtesy of Grugel, R.N [3]).

However, the Shan-Chen model could successfully simulate elongated porosity based on the in situ X-ray tomography result of Ref.[124]. The experiment refers to directional columnar dendrites of Al-30 wt% Cu alloy contained between two plates as shown in Figure 33. The dendrites were growing downward at an angle of about 60° from the horizontal. The contrast of the image was proportional to the atomic number of the elements (i.e., low Cu concentration appears white in the image). The eutectic line was a nearly straight thin line, shown at about the middle of the Figure 33 images. During the solidification, the shape of the left bottom bubble changed from circular to worm-shape as it can be seen in Figure 33 from the left to right images. The elongated shape can be seen for both left and right bubbles. Since the model parameters were not the same as the experiment, it is hard to compare the results directly. However, the Shan-Chen models can predict that the shape of the bubble changes from a circular to an elongated elliptical shape due to adhesive force between the bubbles and dendrite.



Figure 33. Gas porosity evolution in a directionally solidified Al-30 wt% Cu alloy. (Courtesy of R. Mathiesen, Sintef,[124]).

In conclusion, the Shan-Chen models were capable of modeling phenomena observed in experiments, such as the narrow and long worm-like bubbles in the interdendritic regions. However, they were unable to simulate phenomena that produce

characteristic velocity in the order of 1 mm/s or lower since the spurious current masks the physical flow.

5.4. Fully Coupled Modeling of Bubble Dynamics during Solidification

The model was developed and validated in the section 3.5.1. and 4.2. and 4.3. was used to study the interaction between existing bubbles and evolving dendrites. For the sake of the simplicity, the gas component rejection into the liquid phase during solidification was neglected. The material properties and temperature gradient were chosen to follow the PFMI experimental conditions. The initial condition is shown in Figure 34(a). A constant temperature gradient of 716 K/m was imposed in the vertical direction. The dendrites were considered as rigid solid; no slip bounce back boundary condition was applied for fluid flow and solute transport. For the transport equation, zero flux boundary condition was used for all walls. For temperature field, only vertical walls were subjected to adiabatic boundary conditions, while horizontal walls were kept at a constant temperature. The bottom wall temperature was maintained at 0.7 K undercooling. In CH equation, for nodes inside bubble ϕ is initially set to 0, and for nodes in the melt ϕ is set to 1. The boundary condition for solid phase and evolving dendrites are $\phi = \phi_w$. The grid size was chosen as 1.2 μm , while the time step size was $4.8 \times 10^{-6}\text{s}$ for the CA model and the LB model for solute transport equation. The timestep for LB-PF was one tenth of time step for CA method. Other simulation parameters are listed in Table 9, based on the PFMI experiments for SCN-0.24 wt% water alloy.

Table 9. the PFMI experiment parameter for SCN-0.24 wt% water alloy.

Bubble radius	Contact angle	Number of mesh	Domain size
60 μm	150°	180×150	21 × 180 μm^2

Figure 34 presents the evolution of the dendrites and their interaction with the bubble during solidification of SCN-0.24 wt% water alloy at $Ma = 0.515$. The Marangoni number is calculated using Equation (63) based on the values listed in Table 1 and Table 9. Since the Marangoni number is low, the bubble sticks to the wall and would barely move. Initially, all of the dendrites grow in their preferred crystallographic direction. But later, the Marangoni convection disturbs the stream of the low concentration flow at the interface of the dendrite growing in its vicinity and delays the secondary arm formation; side-branch is seen to appear in later time steps. Even for that small Ma number, the change in the morphology of dendrites can be observed. In addition, as the dendrite grows, the bubble deforms from a half circle to a wormhole (elliptical) shape, which is also observed in PFMI experiments. Although the phase-field variable, ϕ , for both liquid and gas phases is conserved globally, it is known that there exists a critical radius for bubble below which the bubble shrinks spontaneously to the bulk fluid. This phenomenon is observed in other studies as well [125].

It is known that in the absence of convection, dendrites grow symmetrically in their primary direction [21,126]. However, the induced Marangoni convection around the bubble affects the neighboring dendrite growth. Figure 35 compares the dendritic growth in the absence and in the presence of the bubble (i.e., without and with Marangoni convection, respectively). The concentration field is not symmetric in Figure 35(b), due to the existence of bubble and the induced Marangoni convection. More perturbation is

observed on the surface of the dendrite located near the bubble as compared to the dendrites far from the bubble or dendrites growing in the absence of Marangoni convection. Two concentration peaks are observed in top corner. These peaks can be explained by the way boundary conditions were implemented for corner nodes, which generates a small perturbation in neighboring nodes. However, the dendrite growth is not affected by the perturbations since they are small and far from dendrites.

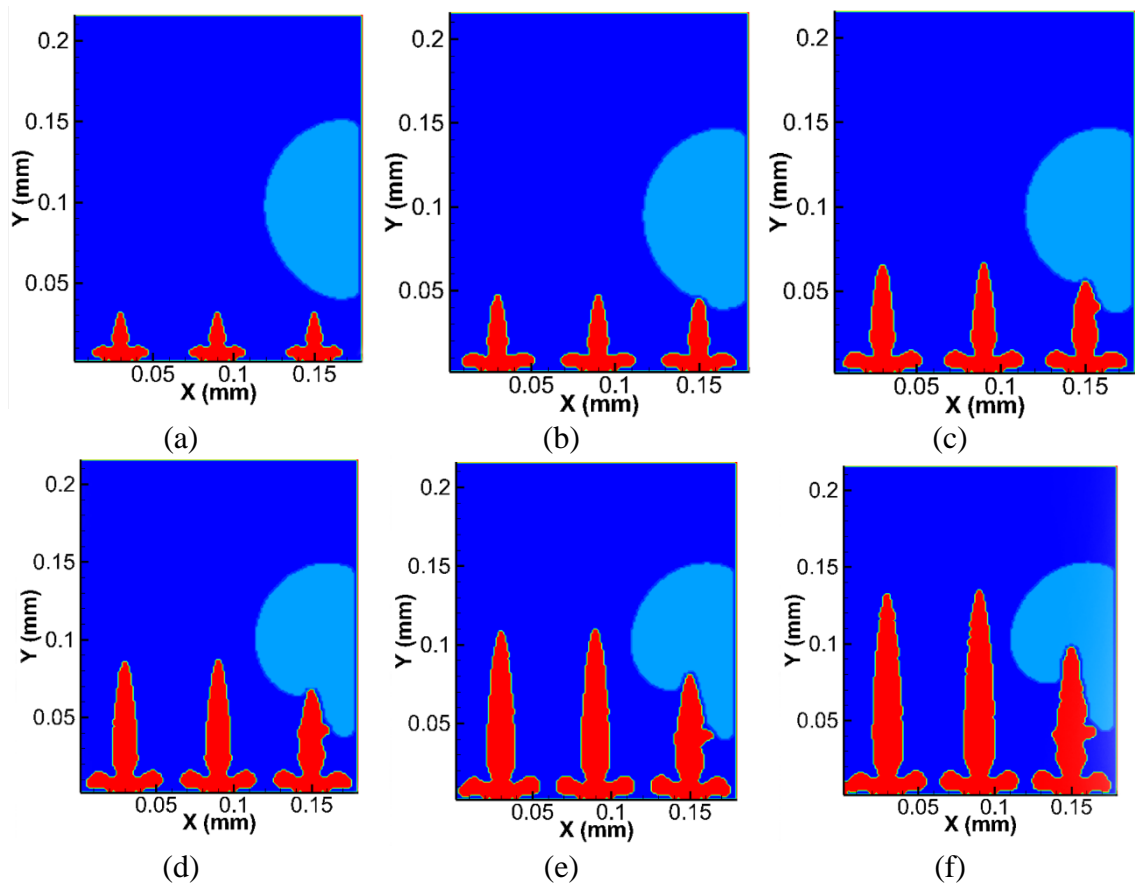


Figure 34. Simulation of bubble-dendrite interactions for $Ma=0.515$ at (a) $t=0$, (b) $t=0.072$, (c) $t=0.144$, (d) $t=0.216$, (e) $t=0.288$, and (f) $t=0.36$ s. (Red: solid, light blue: bubble, blue: liquid) [127]

The generation of two main vortices with opposite directions is depicted in Figure 36. The bubble also generates small eddy currents between dendrites. Since the bubble is

small, the generated Marangoni convection is not strong enough to change the morphology significantly.

The model assumes that dendritic growth only takes place when the order parameter is larger than 0.5. In other words, transformation to solid only happens from liquid phase and not from the gas phase.

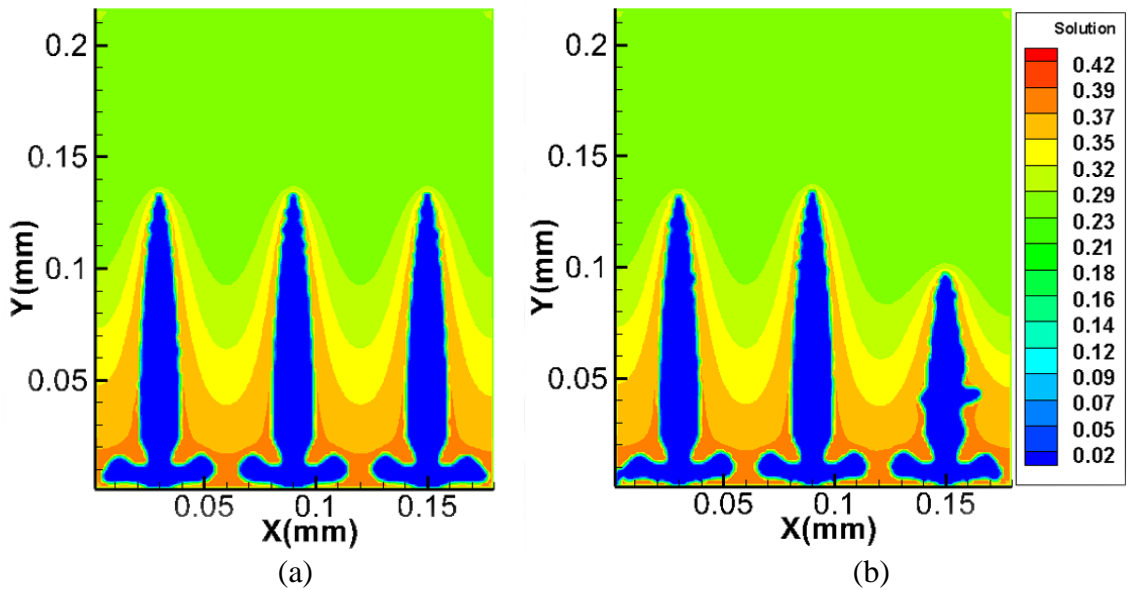


Figure 35. Concentration field around dendrites (a) without any convection (b) with Marangoni convection. Both results are presented at $t = 0.36$ s

The same problem is solved for two smaller bubbles ($12 \mu\text{m}$) trapped in the dendritic region to study the effect of smaller bubbles on dendrite growth. As observed in Figure 37, the induced Marangoni convection for smaller bubbles is not large enough to influence the morphology of dendrites and does not have any visible effect on the dendrite growth.

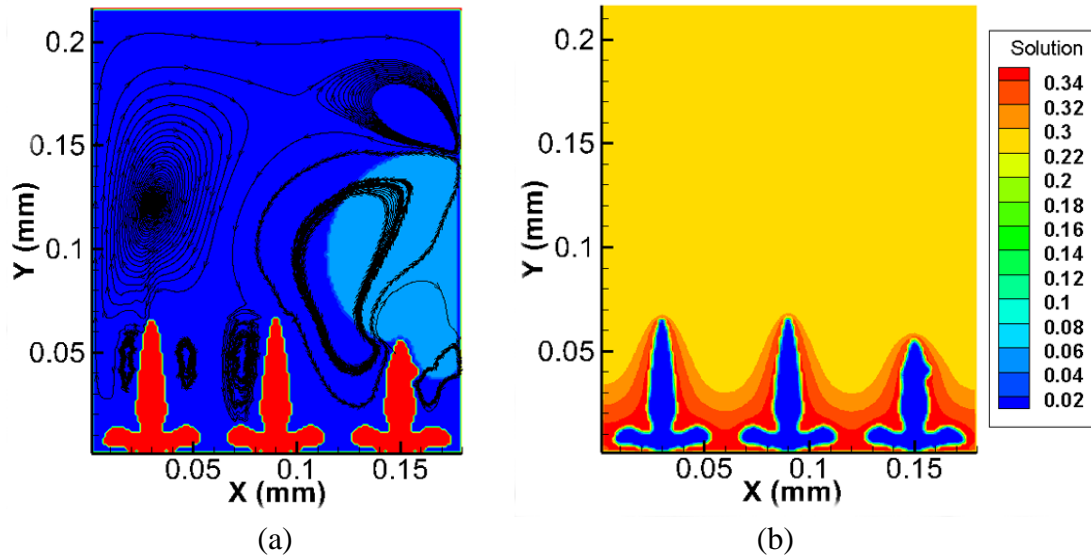


Figure 36. Streamline and concentration distribution around the dendrites growing under $Ma=0.515$ at $t=0.144$ s

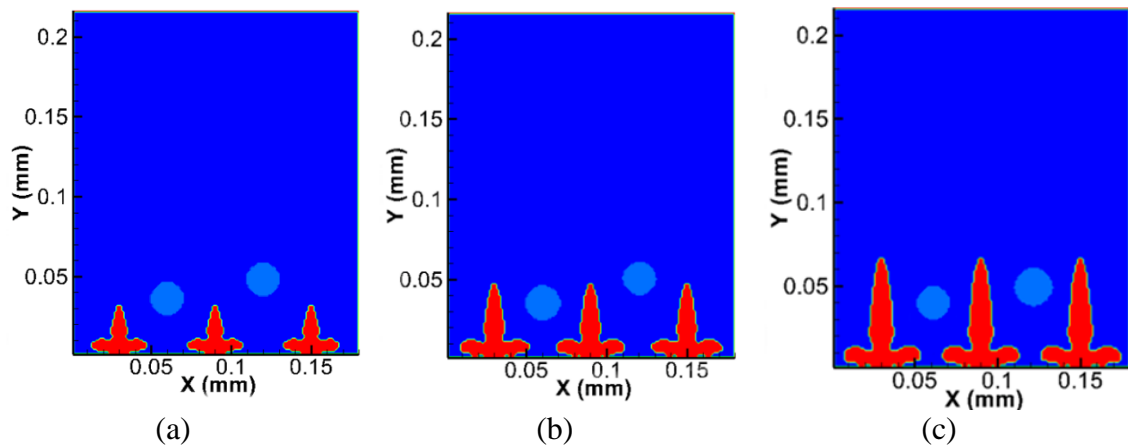


Figure 37. Simulation of dendrite growth in presence of two small bubbles for $Ma=0.025$ at (a) $t=0$, (b) $t=0.072$ and (c) 0.144 s (Red: solid, light blue: bubble, blue: liquid)

5.5. Effect of Bubble Size on Dendrite Growth

In the PFMI experiment, it was observed that bubble-induced Marangoni convection causes changes in fluid flow, temperature and concentration fields which eventually alters the morphology of dendrites as they approach the bubble. The

simulation results presented below show that the bubble induced Marangoni convection changes the dendritic morphology and also distorts the solid/liquid interface.

The simulations presented in section 5.4 were solved by full coupling of dendrite growth and bubble motion models. For higher Marangoni numbers, a very small time step is needed for the CH equation to prevent divergence. To mitigate this problem, the bubble is assumed to be stationary ahead of the solid front, while Marangoni convection may be induced in the melt due to the surface tension gradient at the interface. This is a valid assumption as reported by many experimental observations [3,8,10,40,128,129].

Effect of induced Marangoni convection on dendrite morphology is investigated for SCN-0.24 wt% water alloy. A temperature gradient of 716 K/m and cooling rate of 0.1 K/s was considered, while different Marangoni numbers were implemented because of simulating different bubble sizes. A relatively large domain of $3.5 \times 5 \text{ mm}^2$ was simulated. The objective was to investigate the influence of the induced Marangoni convection on the morphology of growing dendrites at early stages of solidification. The grid size was chosen as 7 μm while the time step was $2.8 \times 10^{-5} \text{ s}$. The properties listed in Table 1 and Table 9 were used in the simulations. The influence of the varying Marangoni number on the dendritic growth is presented in Figure 38. While at small Marangoni numbers the effect on dendrite growth is negligible, the dendrites in the vicinity of the bubble are significantly affected at larger Marangoni numbers. The convection induced at large Marangoni numbers affects the growth direction and morphology of neighboring dendrites. It should be noted that the results are captured at identical time steps. Under more severe Marangoni convection the dendrites away from

the bubble achieve a faster growth speed while growth of dendrites in the immediate neighborhood of the bubble is suppressed. This can be explained by distorted isotherms presented in Figure 39.

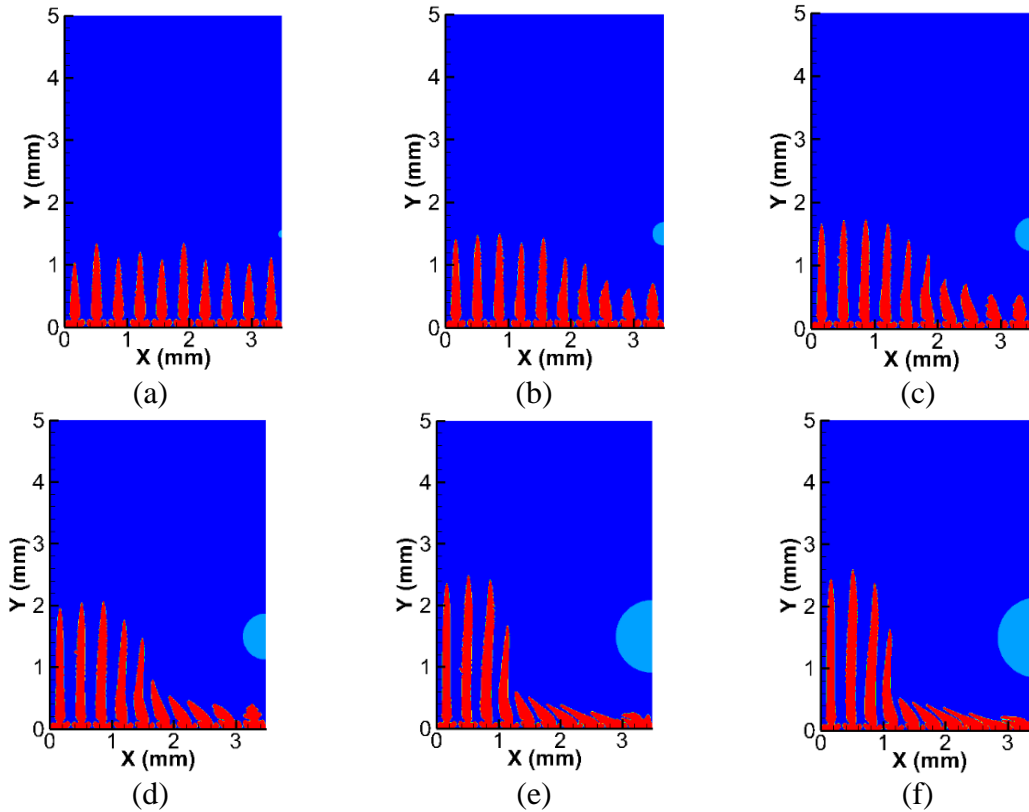


Figure 38. Effect of Marangoni Convection on dendrite growth at (a) $Ma=0.5$, (b) $Ma=5$, (c) 10, (d) 20, (e) 50, (f) 60.5 related to bubble radius (a) $R=0.03$, (b) 0.187, (c) 0.264, (d) 0.3736, (e) 0.59 and (f) 0.65 mm respectively. All of the results are presented for $t= 11.2$ s. (Red: solid, light blue: bubble, blue: liquid)

The influence of bubble size on dendrites can be explained by the strength of the generated vortex and by comparing the streamlines and isothermal contours, as presented in Figure 39. While the vortex induced by larger Marangoni numbers can completely distort the isotherm, the convection generated by small Marangoni numbers barely affects the isotherm. Therefore, the region near the bubble has a higher temperature compared to

a location far from the bubble. The temperature difference makes the dendrite far from the bubble grow faster than the dendrites near the bubble. For large Ma numbers, the convection is strong enough to prevent the neighboring dendrites from growing along their prior preferred crystallographic orientation.

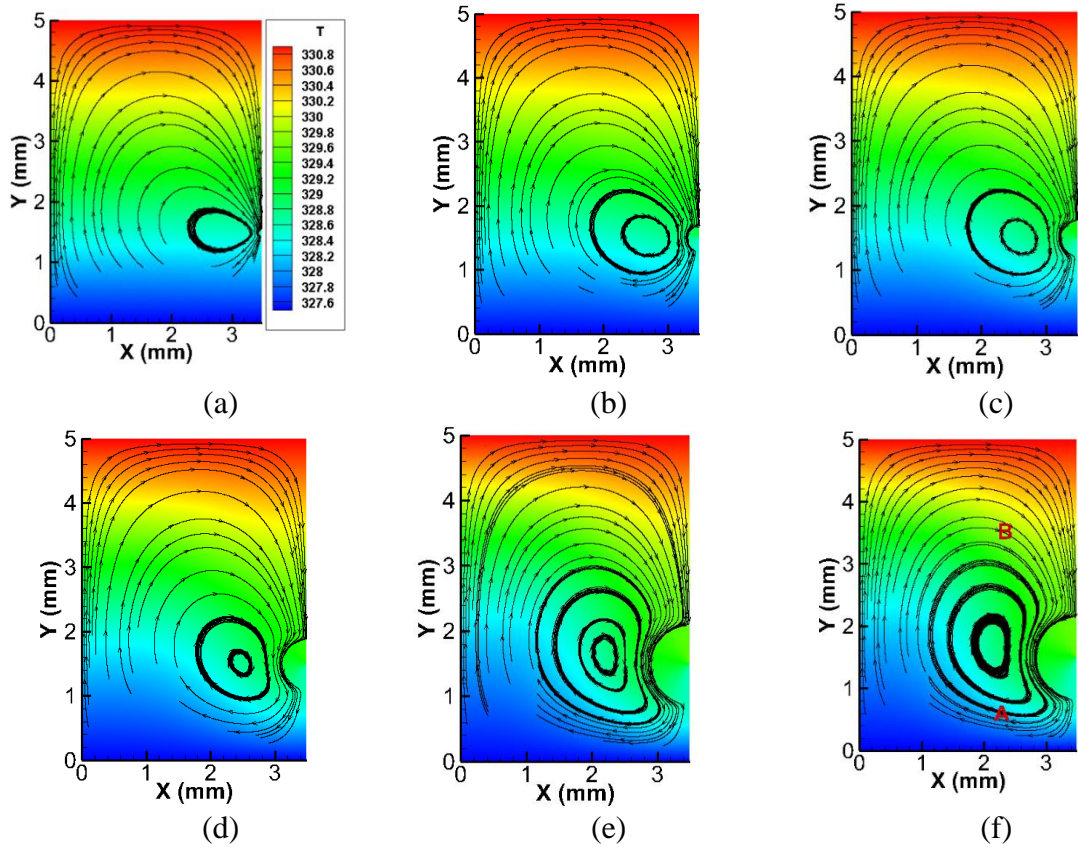


Figure 39. Effect of Marangoni convection on temperature contour and fluid flow at (a) $Ma=0.5$, (b) $Ma=5$, (c) 10, (d) 20, (e) 50, (f) 60.5 related to bubble radius (a) $R=0.03$, (b) 0.187, (c) 0.264, (d) 0.3736, (e) 0.59 and (f) 0.65 mm respectively.

The streamlines do not provide any information about the strength of Marangoni convection since a similar trend is observed for different Marangoni numbers. To study the strength of the generated vortex, the velocity magnitude was measured at the midsection of the domain along the horizontal direction ($y=2.5$ mm). The results are

presented in Figure 40. The velocity magnitude for $Ma=0.5$ is almost zero while it reaches to 0.3 mm/s for $Ma=60.5$. By increasing the Ma number, the velocity magnitude also increases, as shown in Figure 40. The maximum velocity takes place near the bubble region. In all cases, the velocity magnitude is zero near the wall due to the applied no-slip boundary condition.

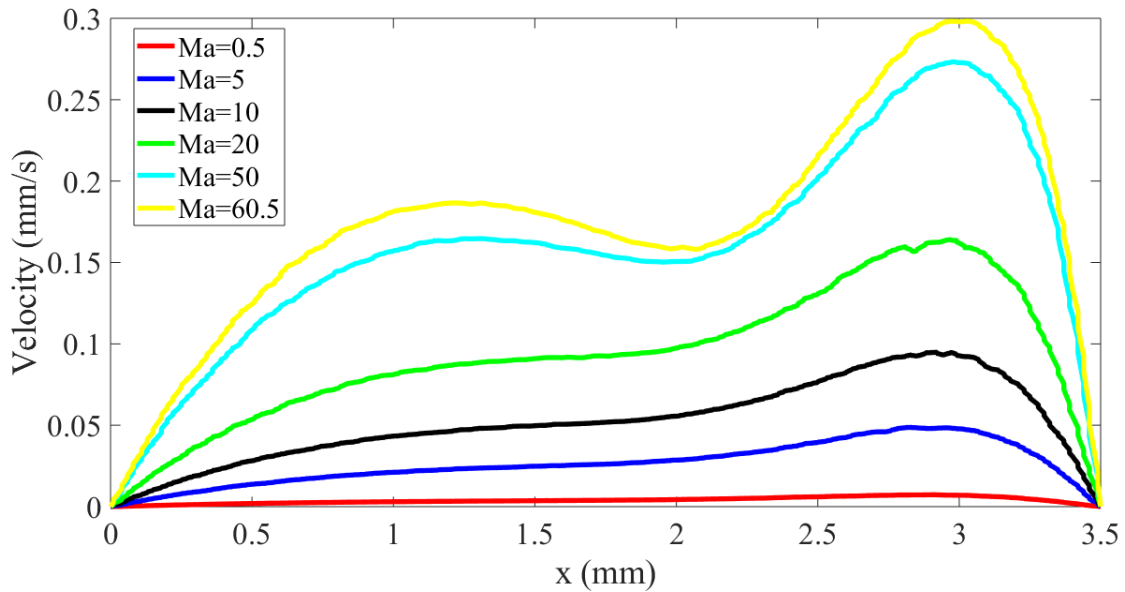


Figure 40. Fluid velocity magnitude at the midsection of the domain ($y=2.5\text{mm}$) for different Ma numbers.

Until now, we developed a two-dimensional (2D) model and simulated the bubble-dendrite interactions during directional solidification of a SCN-0.24 wt% water alloy. We also found that if the bubble is large enough, the resultant Marangoni convection can significantly alter the temperature profile in the adjacent liquid, which deters the dendrites from growing in their preferred orientation. However, there are some limitations to consider in the 2D model. Obviously, the melt cannot flow in the third dimension, which compromises the actual solute concentration profile. It is already

known that diffusion in 3D models is more accurate than in 2D models [121]. Due to the higher solute concentration at the interface, 2D dendrites grow slower compared to 3D dendrites. Additionally, blockage effects caused by bubble or dendrites in the 2D simulation could lead to inaccurate thermal and solute profiles. A 3D simulation is needed to provide more accurate and reliable results.

The purpose of the following section is to investigate the effects of Marangoni convection induced by bubbles on dendrite growth using 3D modeling. A CA-LB model was developed to model the induced convection and track the solid/liquid interface. The induced Marangoni convection during remelting was compared with experimental results. After validation, we proceeded to examine the effects of different parameters related to induced convection on the microstructural evolution.

Again, the induced Marangoni convection during remelting is studied and used as a model validation by comparison with PFMI measurements. As seen before, the bubble located at the left bottom in front of the S/L interface is responsible for Marangoni convection. The existence of Marangoni convection can be inferred by following small bubbles through their paths. The LB model was used to calculate the melt velocity in the presence of a 1.3 mm bubble in front of columnar dendrites. It was assumed that the shape and morphology of dendrites do not change over simulation time. This is a reasonable assumption since the remelting speed of dendrites in the PFMI experiment is orders of magnitude smaller than the calculated speed of the small bubbles [3]. Therefore, the morphology of the dendrites is fixed prior to the simulation of Marangoni convection.

The numerical simulation was carried out in two steps. In the first part of the simulation, the dendritic morphology was produced by simulating columnar dendrite growth of SCN-0.24 wt% water alloy in a convection-free domain. The dendrite growth was calculated using the CA model and by solving the solute concentration equation. The grid size was 5 μm , while the domain was a cuboid with a square base of $3.5 \times 3.5 \text{ mm}^2$ and length of 6 mm . 81 solid seeds were placed in the bottom low-temperature wall with a primary arm spacing of 350 μm . A constant temperature gradient of 716 K/m was applied along the length of the domain. The material properties for all the simulations in this dissertation are listed in Table 1. The resulted dendrites are shown in Figure 41. In the second part of the simulation, the dendritic microstructure from the previous part was imported into the fluid flow model. Then, an entrapped bubble with a diameter of 1.3 mm was added in front of the S/L interface. The Marangoni force was applied to the free surface of the bubble, as discussed in section 3.2. The domain size, grid spacing, and temperature gradient were the same as the first step. The induced Marangoni convection around the free surface of the bubble is illustrated in Figure 41. Comparing the results with Figure 4, the same clockwise circulation is observed. It is also observed that the fluid speeds up when it approaches the bubble and conversely deaccelerates when it distances from the free surface of the bubble. It should be noted that due to the relatively coarse mesh size, secondary branching is not captured, but this is not necessary to simulate the bubble-induced convection.

To compare the result of the current simulation with PFMI experiment, a specific tracer bubble which reaches the maximum distance of 2.8 mm from the S/L interface was

followed in its path. The instantaneous velocity can be calculated at several points along its path. For the simulation, the velocity along a specific streamline that reaches 2.8 mm from S/L interface was plotted. The comparison is shown in Figure 42.

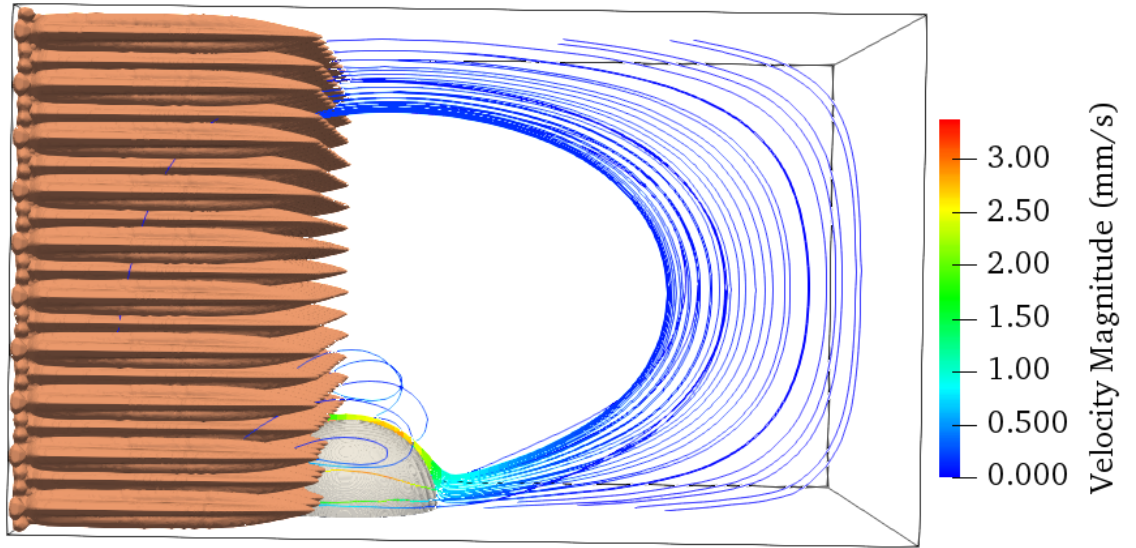


Figure 41. Simulation results of induced Marangoni convection during remelting. Here streamlines are colored with Velocity Magnitude. The domain size is $3.5 \times 3.5 \times 6 \text{ mm}^3$ and flow direction is clockwise.

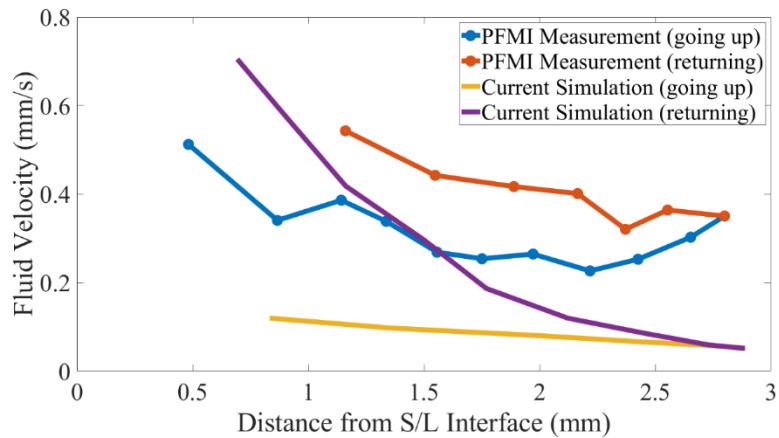


Figure 42. Fluid velocity along a specific path line: comparison between PFMI experiment and the current dissertation.

The same behavior of fluid acceleration when approaching the S/L interface and deceleration when moving away from the interface is observed in both simulation and experimental results. It should be noted that the tracer bubble and the fluid may not have the same velocity. The difference between the bulk fluid flow and the bubble velocity can be explained by the slip ratio. Slip ratio is introduced as the ratio of the bubble velocity to the melt velocity. The slip ratio for the case of gas in bulk fluid is greater than one due to the finite size of the tracer bubble in the PFMI experiment, which means that the tracer bubble velocity is expected to be greater than the melt velocity. This is consistent with the results shown in Figure 42.

The CA-LB model presented in Chapter 3 was combined with a finite difference model for energy equation and was utilized to study the effect of Marangoni convection on dendrite growth. The schematic of the domain is shown in Figure 43.

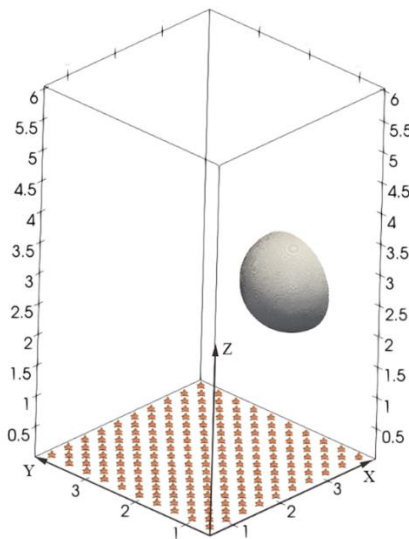


Figure 43. Schematic of the initial condition for the simulation. The temperature gradient is imposed on the vertical direction ($G=716$ K/m). The domain size is $3.5 \times 3.5 \times 6$ mm³. Eighty-one seeds were placed on the bottom wall, all with the same crystallographic direction [001]. A bubble with a diameter between 0.5 mm to 1.5 mm was in front of the solid front.

No-slip bounce back boundary condition was implemented for fluid flow and solute transport at the S/L interface. For the transport equation, zero-flux boundary condition was used for all walls. A temperature gradient of 716 K/m was applied in a vertical direction. Only on vertical walls, the adiabatic boundary conditions were imposed, while the bottom wall was initially at a 0.7 K undercooling. A cooling rate of 0.1 K/s, same as the PFMI experiment, was applied to gradually cool down the domain as it is shown in Equation (1) by \dot{Q} . A hemispherical bubble with the diameter of d was attached to the wall at the distance of $1.5+d/2$ mm from the bottom. In addition, 81 solid seeds with the primary arms spacing of 350 μm were placed in the bottom wall. The simulation was performed for 4 cases where the bubble diameter was 0.5, 1, 1.3, and 1.5 mm corresponding to Ma number 9, 35.8, 60.5, and 80.6. No-slip bounce back boundary condition was implemented for fluid flow and solute transport at the S/L interface. For the transport equation, zero-flux boundary condition was used for all walls. The simulation results for $d=0.5$ mm and $d=1.5$ mm are presented in Figure 44.

Comparing the induced Marangoni convection for larger and smaller bubbles reveals that although the same circulation is observed for both cases, the dendrite growth speed is not the same. While the effect of small bubble on dendrite growth is insignificant, the neighboring dendrites are significantly affected by the larger bubble.

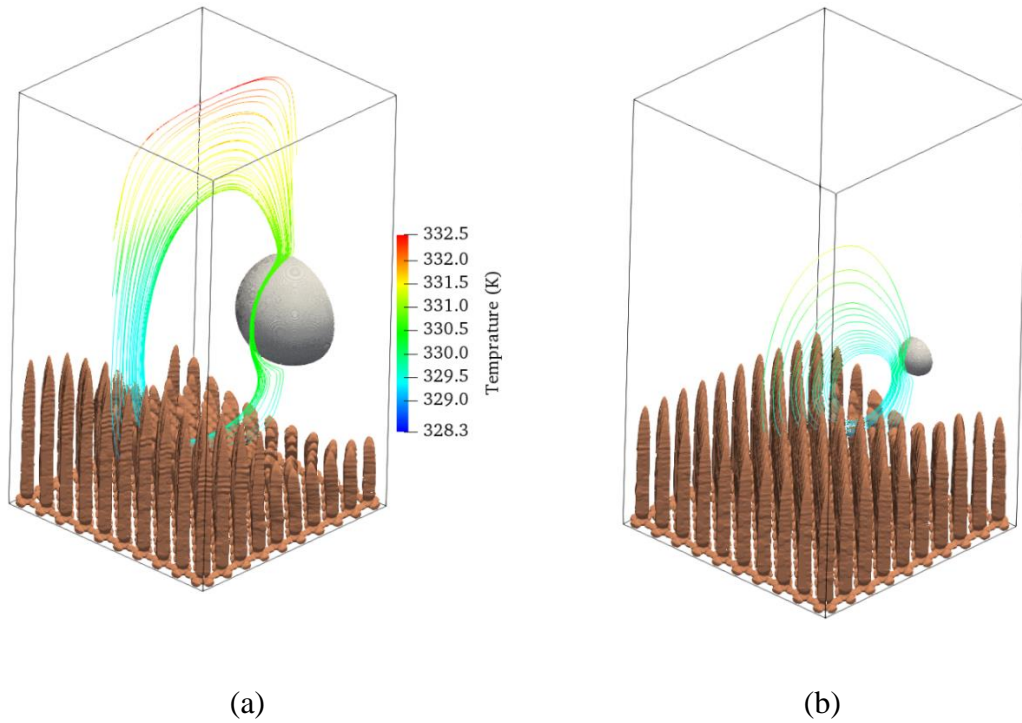


Figure 44. Simulation results for bubble-dendrite interactions at $t=2.97$ s for different bubble sizes: (a) $d=1.5$ mm and (b) $d=0.5$ mm. All dimensions are in mm and streamlines are colored with temperature. The domain size is $3.5 \times 3.5 \times 6$ mm³.

The effect of distance from the bubble on dendrite growth speed was further investigated. The interface velocity for all 81 dendrites is plotted in Figure 45 for $t=0.5$ s to $t=5$ s. The distance from the bubble is categorized as near, moderate, or far, based on the measure explained below. Considering a horizontal plane passing through the middle of the bubble and projection of initial seeds on that plane, if the distance from the center of the bubble to the initial seed is less than d , then it is called near distance. If the distance is between d to $2d$, it is called moderate distance, and if the distance is greater than $2d$, it is called far distance. Later in the dissertation, we explain how d and $2d$ were selected as thresholds. Based on this categorization, there are more dendrites labeled as near for the larger bubble as compared to the smaller bubble. On the other hand, more

dendrites are labeled as far distance for the smaller bubble. More details on the distribution of dendrites over different distances from bubbles, including morphology variation, will be later shown in Figure 49.

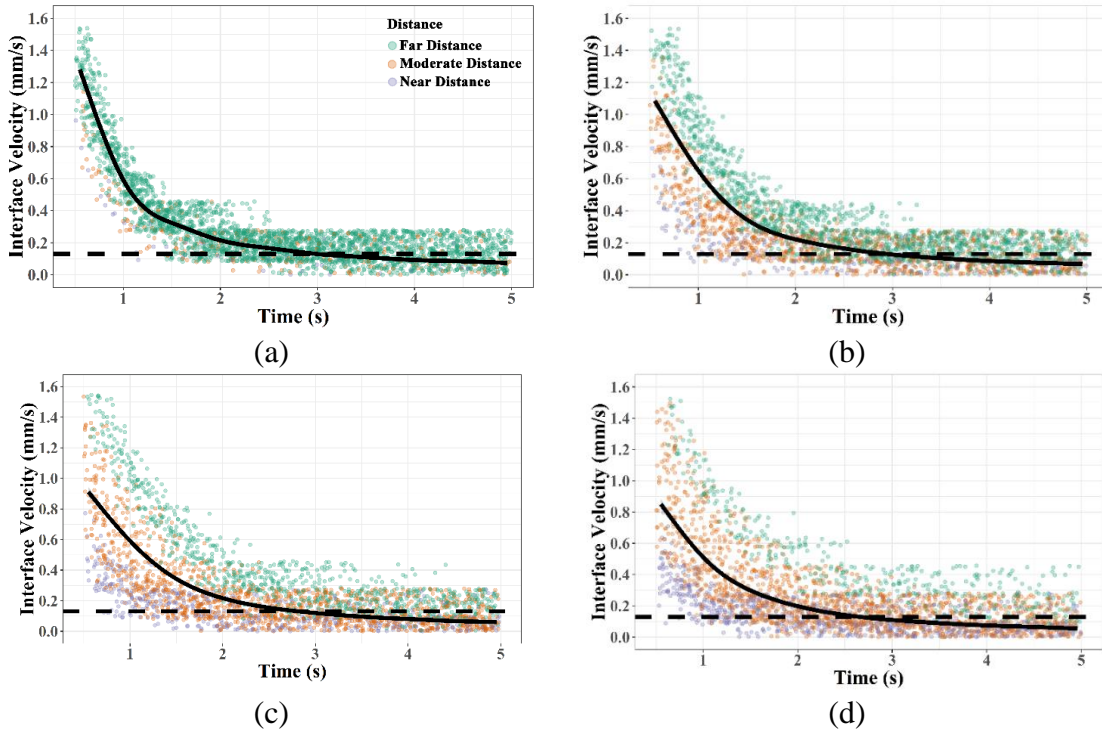


Figure 45. Effect of bubble size on dendrite velocity (a) $d=0.5$ mm, (b) $d=1.0$ mm, (c) $d=1.3$ and (d) $d=1.5$ mm. The dendrites were grouped based on their distance from the bubble. The horizontal dashed line is the PFMI average dendrite growth speed. The black line corresponds to the mean velocity of all dendrites from simulations.

From the figure, it is observed the dendrites growth speed decrease through time.

For small bubble, all the dendrites have almost the same speed in each time step.

However, the variation in dendrites speed is observed for larger bubble based on the distance from the bubble.

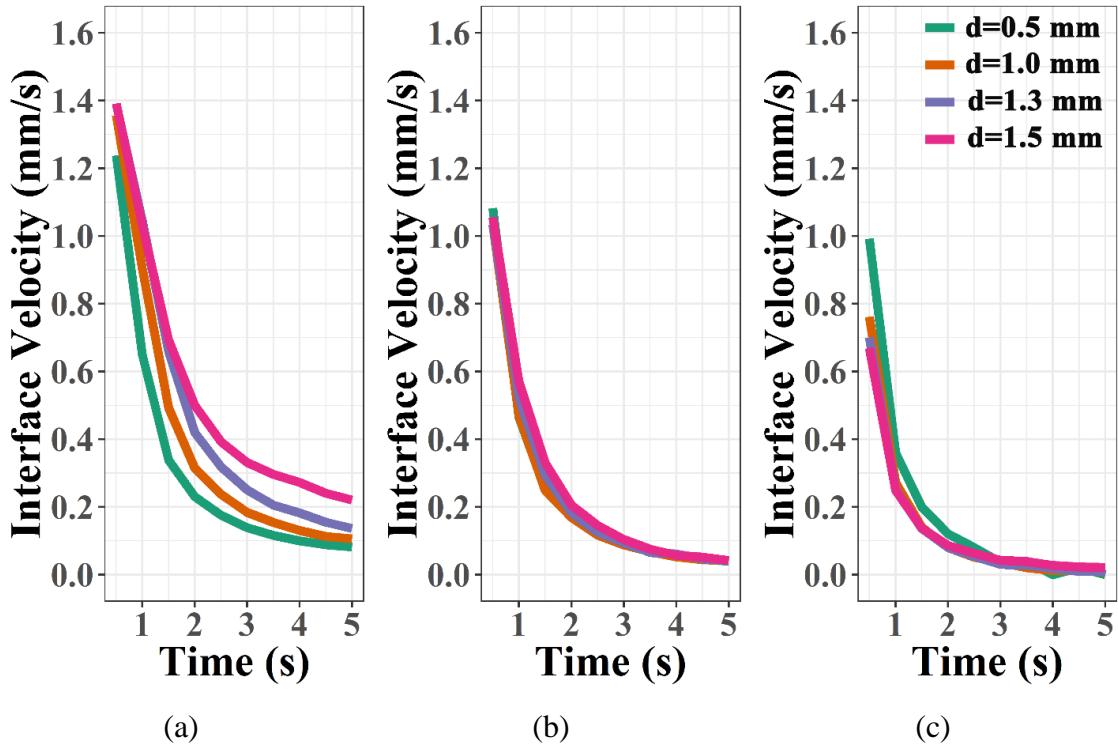


Figure 46. Effects of bubble size (corresponding to Ma number 9,35.8, 60.5 and 80.6) on average dendrite speed during the simulation for (a) far, (b) moderate distance and (c) near distance from the bubble.

As mentioned before, the category of distance from the bubble is related to bubble size. Figure 46 shows the average dendrite speed based on category and bubble sizes. By trial and error between different values, two bounds are selected in a way that all the average lines for moderate distance category are almost overlapped together.

The dendrites morphology evolution and fluid flow pattern are different for each distance category. For near distance dendrites, the flow carries the warmer melt, which reduces the dendrite growth rate and would cause any secondary or tertiary arms to dissolve. The dendrite fragmentation phenomenon is supported by experiments reported in Grugel et al. and Liu et al. [3,130].

For moderate distance from the bubble, the fluid flow is perpendicular to dendrite growth. For larger Marangoni numbers, the convection carries solute-rich and still warm fluid from the near distance dendrites. As a result, for any dendrite, its right side would encounter warmer solute-rich melt while its left side encounters slightly solute poor colder melt. Both effects would cause the dendrites to bend from the vertical direction. However, the average dendrite growth rate is the same for all bubble sizes.

For far distance dendrites, the fluid squeezes out from the cold interdendritic region moving parallel to dendrites and causing the dendrites to grow faster.

Effect of Marangoni convection on dendrite growth rate and morphology can be explained by the temperature and solute concentration contours presented in Figure 47. Due to the difference in solubility of water in solid and liquid phases, water gets rejected to the melt during solidification and produces a solute boundary layer which is enriched with water. The rest of the melt outside the boundary layer has a solute concentration close to the initial concentration, C_0 . The solute boundary layer is easily observable in Figure 47.

The thermal boundary layer is thicker than the solute boundary layer, because the thermal diffusivity is much larger than the solute diffusivity.

The velocity magnitude for different size of bubbles along line AB (3 mm distance from the bottom) is illustrated in Figure 48. The magnitude of the induced convection is linked to the bubble size. In all cases, the maximum velocity was observed near the free surface of the bubble (right). Moving away from the bubble, the velocity magnitude in all cases stabilized between 0 to 0.3 mm/s.

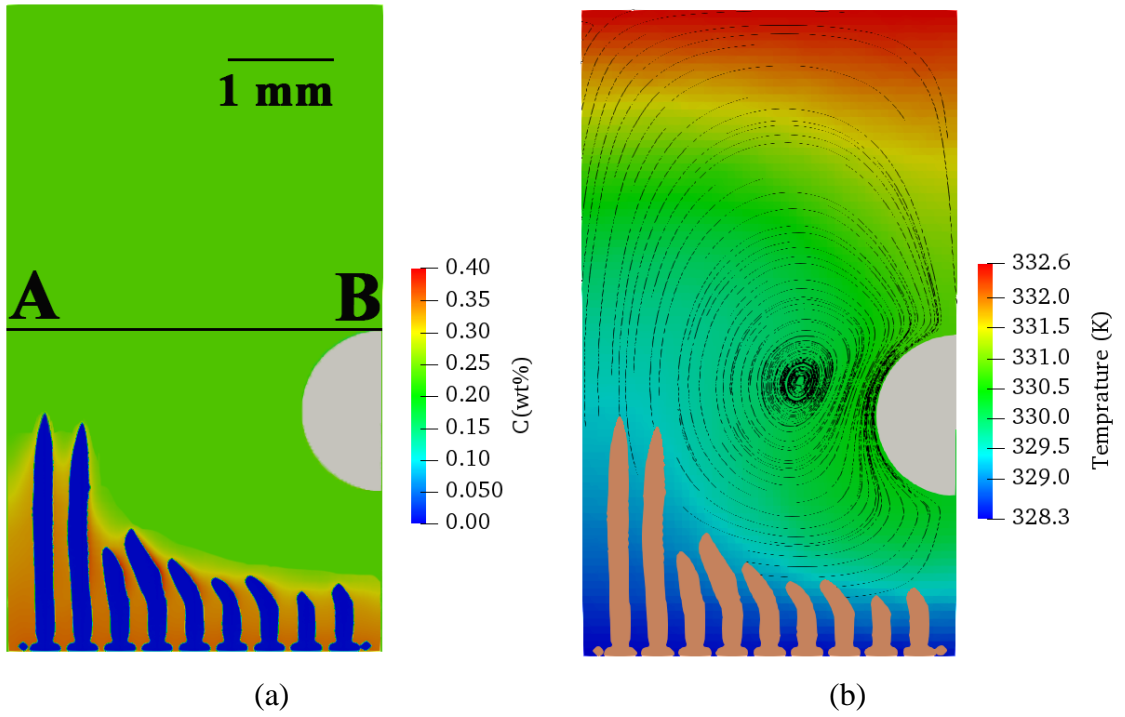


Figure 47. (a) Solute concentration, and (b) temperature fields around the bubble at $t=2.97$ s ($d=1.5$ mm).

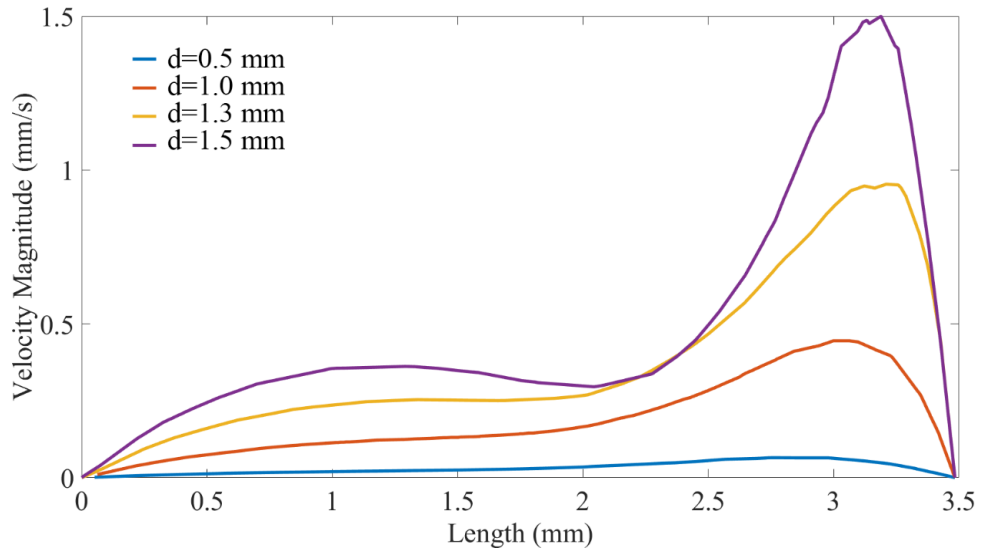


Figure 48. Velocity Magnitude along the A-B line in Figure 47 for different bubble sizes at $t=2.97$ s.

To compare the effect of induced convection on the microstructure, the dendritic morphologies were plotted at a specific time for different bubble sizes, as shown in Figure 49. The figure not only shows the dendrite length with respect to distance from the bubble but also compares the dendritic morphologies in the presence of bubbles of different sizes. While the effects of induced Marangoni convection for the smaller bubble is negligible, the large bubble can alter the growth rate and bend the dendrites in the direction of the fluid flow.

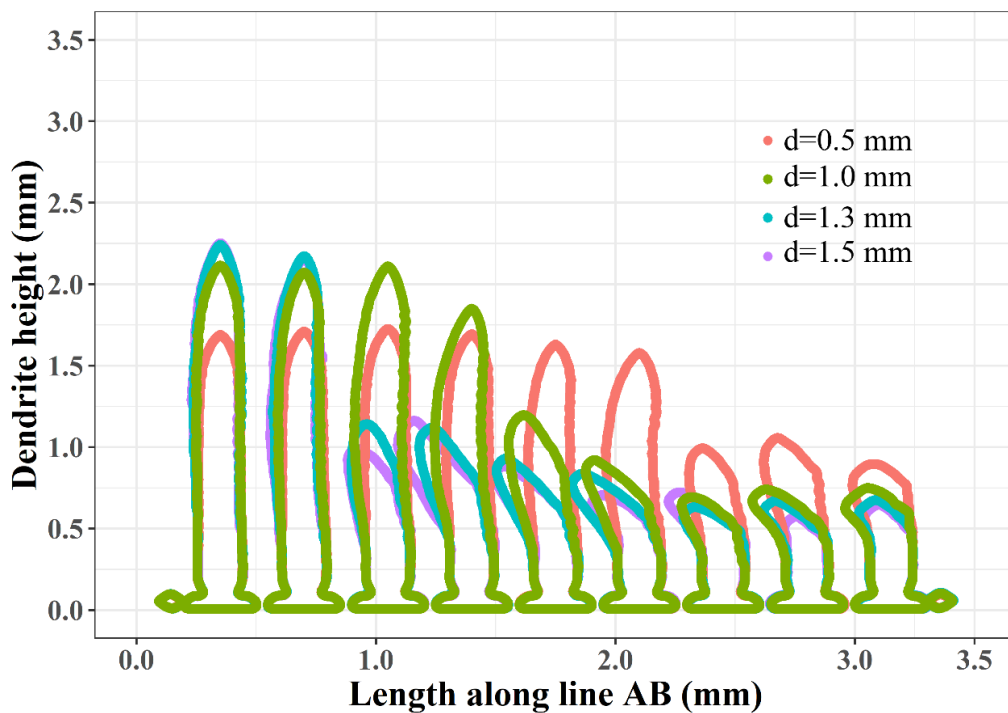


Figure 49. 2D sections of dendritic morphologies at the plane $y=3.75$ mm at $t=2.97$ s for different bubble sizes.

The induced flow near the free surface of the bubble carries the melt with a higher temperature towards the mushy zone (from top to bottom in the figure), which results in a reduction in the dendrite growth velocity. The effect is not restricted to the tip velocity,

but it also hinders the growth of side branches. On the other hand, for the dendrites far from the bubble, the induced convection washes away the high concentration solute from the dendrite's tip leading to a faster growth when the flow and S/L interface are advancing in the same direction, which is also observed in the PFMI experiment, as it was shown in Figure 8.

5.6. Spurious Grain Formation due to Marangoni convection during Directional Solidification of Alloys in μ -g Environment of International Space Station

Finite element simulations by COMSOL Multiphysics 5.0 [131] were used for calculating fluid flow and pattern of motion of fragmented dendrites. COMSOL Multiphysics solves coupled systems of partial differential equations by finite element method. The initial conditions and domain size of the two-dimensional simulation are shown in Figure 50(c). A vertical line separates the mushy zone in the domain from the rest of the melt. The morphology of primary dendrites in the mushy zone was directly imported from the experiments Figure 50(a).

The dendrite fragment 800 μm long and 60 μm in height and width (as measured from Figure 5) is shown on the right side in Figure 50(c). The temperature gradient of 716 K/m (same as PFMI experiment) was imposed in the horizontal direction. The 1.3 mm diameter bubble is located within the mushy zone just below the tips of the dendrite array.

To corroborate the effects of rotation of fragmented dendrites in the MICAST experiment, a finite element simulation by COMSOL Multiphysics was utilized using the physical properties of Al-7 wt% Si alloy listed in Table 2.

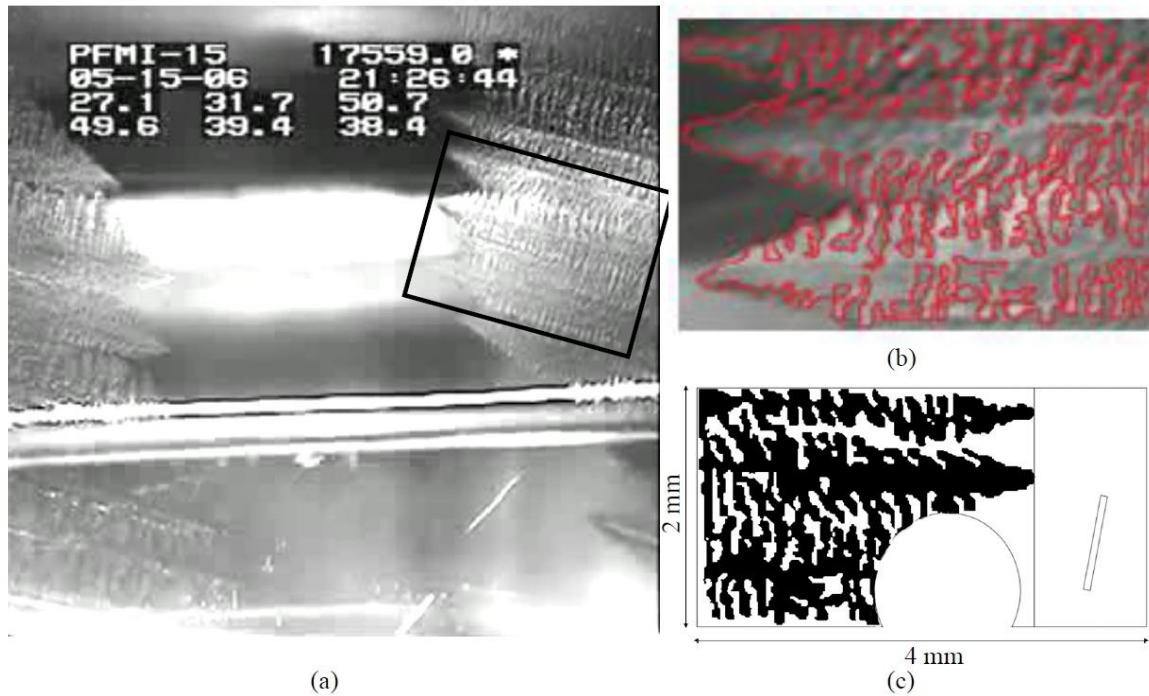


Figure 50. Morphology of dendrite array when the heater was moved away, and the dendrites grew and solidified (21:26:44). The mushy-zone schematic used in (c) for simulation were imported from (b) shown above. (c) Schematic of the initial conditions for the simulation. The temperature gradient is imposed on the horizontal direction ($G = 716$ K/ m). The domain size is 2×4 mm². The 1.3 mm diameter bubble is located within the mushy-zone close to the array-tips.

The schematics of the simulations are illustrated in Figure 51. The domain size was 14×8 mm², and the dendrite primary arm spacing was 550 μ m. The void length was defined as 11 mm for case (a) and 2.5 mm for case (b). The dendrite fragment was 275 μ m long and 80 μ m wide. It was assumed that the fragment originated by a mechanism, similar to the one described above for the SCN-0.24 wt% H₂O sample, by detachment of a secondary arm from its primary tree. Therefore, it was also assumed that the fragment was initially orientated vertically, normal to the growth direction. The temperature gradient was 3200 K/m.

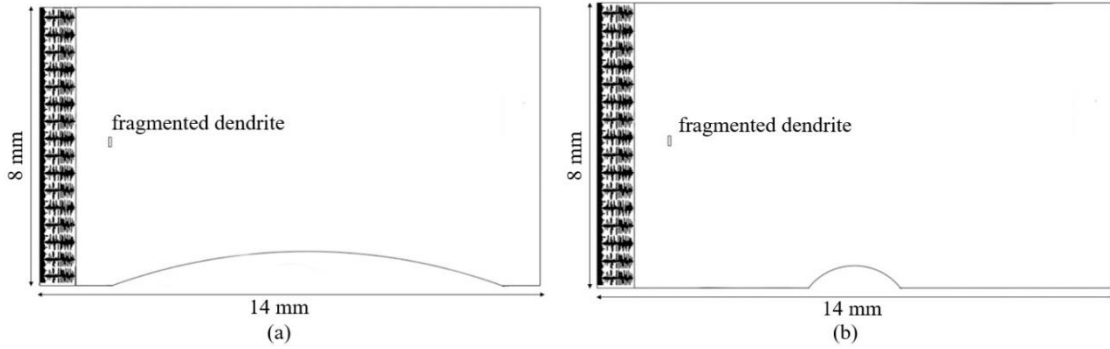


Figure 51. Schematics of the domain dimensions and initial conditions for COMSOL simulations considering two void lengths (a) 11 mm, and (b) 2.5 mm. The temperature gradient was 3200 K/m. The voids were located in the melt ahead of the solidifying mushy zone.

As described above, the Marangoni convection in the microgravity experiments is due to the surface tension gradient at the gas/liquid interface within the pore created by the liquid column getting detached from ampoule wall. The strength is defined by the Marangoni number, Ma , which is the ratio of the thermocapillary effect, and the viscous forces as:

$$Ma = \frac{|\gamma|L\Delta T}{\mu\alpha} \quad (64)$$

Where L is the characteristic length scale (length of the void in the temperature gradient direction), ΔT is the temperature difference across the bubble, γ is the thermal dependence of the surface tension, μ is dynamic viscosity, and α is thermal diffusivity.

The COMSOL Multiphysics software was used to solve the governing equations for incompressible laminar flow in porous media, solid mechanics, and heat transfer.

The governing equations for fluid flow are described as:

$$\frac{\partial u}{\partial x} + \frac{\partial v}{\partial y} = 0 \quad (65)$$

The Navier-Stokes Equation for porous media is written as:

$$\begin{aligned} \frac{1}{\varepsilon} \frac{\partial u}{\partial t} + \frac{u}{\varepsilon^2} \frac{\partial u}{\partial x} + \frac{v}{\varepsilon^2} \frac{\partial v}{\partial y} &= -\frac{1}{\rho_f} \frac{\partial p}{\partial x} + \frac{\mu}{\varepsilon \rho_f} \left(\frac{\partial^2 u}{\partial x^2} + \frac{\partial^2 u}{\partial y^2} \right) - \frac{\mu}{\kappa} u \\ \frac{1}{\varepsilon} \frac{\partial v}{\partial t} + \frac{u}{\varepsilon^2} \frac{\partial v}{\partial x} + \frac{v}{\varepsilon^2} \frac{\partial v}{\partial y} &= -\frac{1}{\rho_f} \frac{\partial p}{\partial y} + \frac{\mu}{\varepsilon \rho_f} \left(\frac{\partial^2 v}{\partial x^2} + \frac{\partial^2 v}{\partial y^2} \right) - \frac{\mu}{\kappa} v \end{aligned} \quad (66)$$

where ε is porosity, κ is permeability, and μ is dynamic viscosity of the fluid. The permeability is written as

$$\kappa(x, y) = \frac{\kappa_0}{100 \times im(x, y) + 0.01 \times \kappa_0} \quad (67)$$

Where $im(x, y)$ is the binary picture imported to COMSOL. The image has the same dimensions as the domain and has a value of 0 for liquid and 1 for solid. the porosity is defined as:

$$\varepsilon_p = 1 - 0.99 \times im(x, y) \quad (68)$$

The energy equation is also solved since the flow is induced by the temperature gradient on the bubble-melt interface.

$$\frac{\partial T}{\partial t} + u \frac{\partial T}{\partial x} + v \frac{\partial T}{\partial y} = \alpha \left(\frac{\partial^2 T}{\partial x^2} + \frac{\partial^2 T}{\partial y^2} \right) \quad (69)$$

The fluid-structure interactions capability of COMSOL Multiphysics is also utilized to predict the motion of the solid in the melt.

The Marangoni convection is induced due to temperature gradient resulting in a surface tension gradient at the interface and is responsible for internal convection inside the domain. It can be formulated as:

$$\left[-p\mathbf{I} + \mu(\nabla\mathbf{u} + (\nabla\mathbf{u})^T) - \frac{2}{3}\mu(\nabla \cdot \mathbf{u})\mathbf{I} \right] \mathbf{n} = \gamma \nabla_t T \quad (70)$$

The simulation results for the PFMI-15 case are shown in Figure 52. The temperature fields and streamlines are plotted for a 20 second interval. The bubble's presence in the bottom is responsible for the dominant vortex roll. The dendrite fragment, marked as a white rectangle, can be seen rotating as a function of time in 10 (a) through (d). In this case, the Marangoni convection barely affects the isotherm, but it is responsible for the rotation of the dendrite fragment.

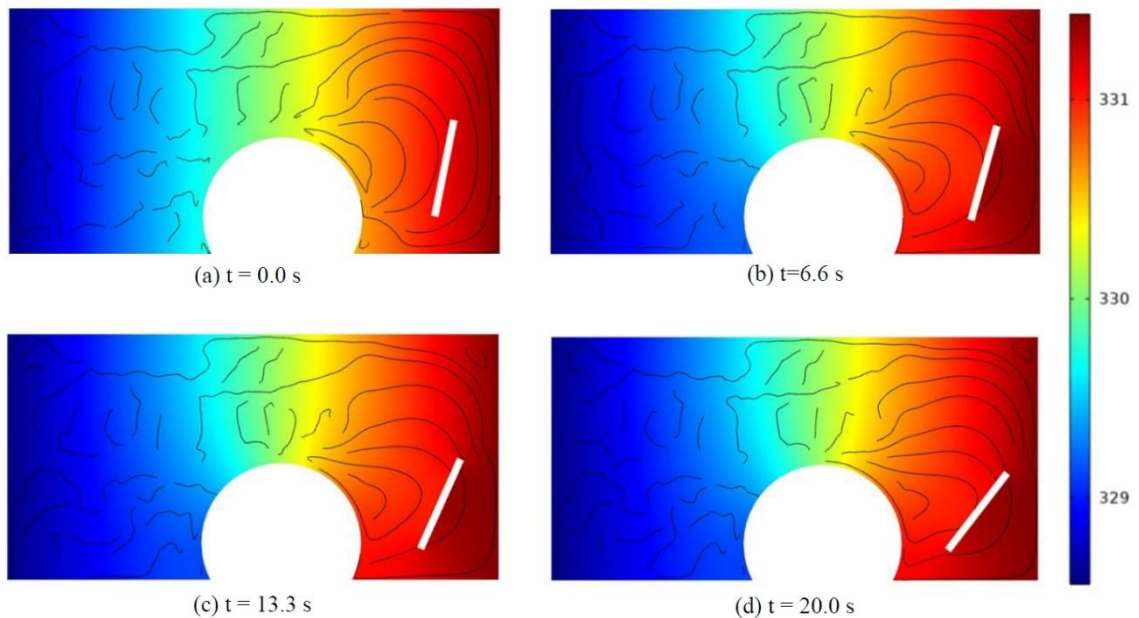


Figure 52. Simulation of the temperature field and streamlines for PFMI 15 experiment (bubble diameter= 1.3 mm, $Ma = 312$, and $G = 716$ K/ m) at (a) $t = 0.0$ s, (b) $t = 6.6$ s, (c) $t = 13.3$ s, and (d) $t = 20.0$ s.

Figure 53 summarizes the trajectory, the x (horizontal) and y components (vertical) of velocity (u and v) for center of mass, and angular velocity of fragmented dendrite. The results show that the fragmented dendrite tends to move toward the bubble at a very low speed. However, the induced convection distorts the isotherms near the rotated fragmented dendrite region, causing apparent clockwise rotation. The order of

magnitude of translational velocity is one μs , where for the angular velocity is one deg/s . The dendrite fragment's final crystallographic orientation is expected to be different from the parent array and when directionally solidified it will grow in its preferred direction resulting in a spurious grain. A rotation of 24.14° measured in the simulation over a 19 s interval is in good agreement with the experimentally observed rotation of about 31.5° over the same interval in the PFMI-video.

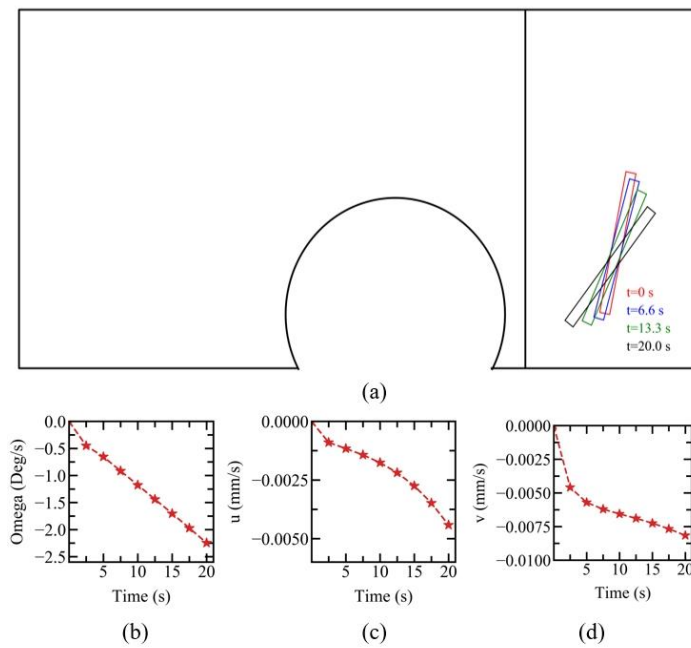


Figure 53. Rotation and velocity components of fragmented dendrite during 20 s of simulation (a) rotation of fragmented dendrites, (b) the angular velocity, (c) and (d) velocity components in horizontal (u) and vertical (v) directions, respectively. The mean rotation speed of the side-branch fragment observed during the PFMI experiment was 1.66 deg/s compared to 1.3 deg/s for simulation.

The temperature distribution and streamlines for the small 2.5-mm diameter surface void in the MICAST sample (Figure 12(b) and Figure 51(b)) during 2 second period are shown in Figure 54. Although the bubble size and temperature gradient and thermal dependence of surface tension are almost 2,4,2 times greater than PFMI sample,

since the thermal diffusivity is around 1/100 of SCN-water alloy, the Marangoni number, in this case, is 104, which is one-third of the one for the PFMI. The Marangoni convection distorts the isotherms, and one primary counterclockwise vortex is observed. However, since the bubble is located outside the mushy zone, the Marangoni convection is much stronger than PFMI. The comparison between isotherms for the PFMI and MICAST samples suggests that convection strength depends on the Marangoni number and the void's location with respect to the S/L interface.

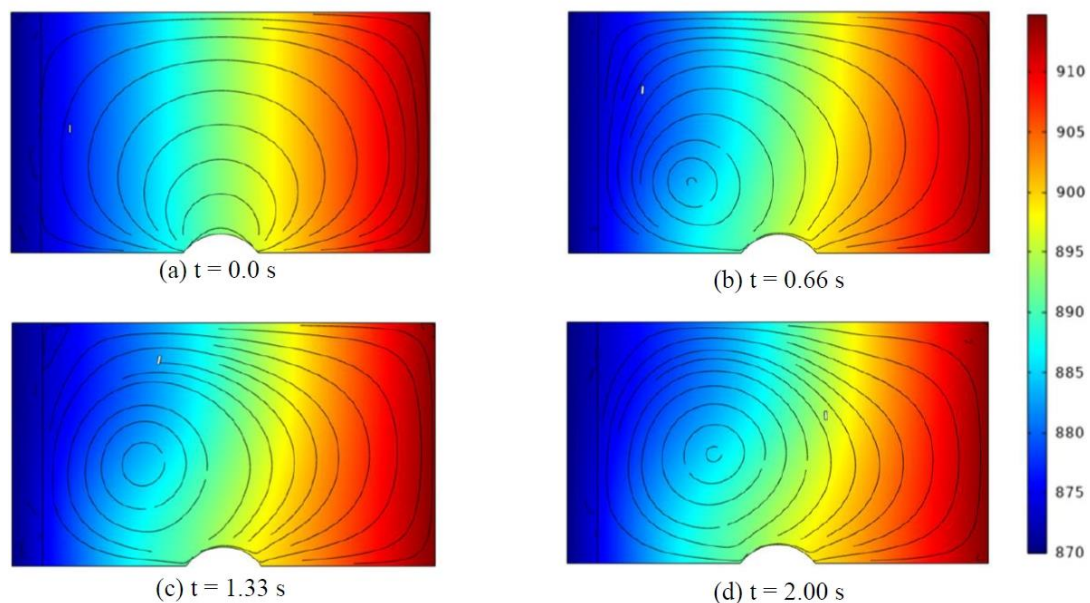


Figure 54. Simulation of the temperature field and streamlines for MICAST2-12 experiment (bubble diameter= 2.5 mm, $Ma= 104$ and $G = 3200 \text{ K/ m}$) at (a) $t=0.0 \text{ s}$, (b) $t= 0.66 \text{ s}$, (c) $t=1.33 \text{ s}$, and (d) $t=2.0 \text{ s}$. The fragmented dendrite is seen as the small white rectangle in the domain.

Again, the trajectory, the center of mass velocity, and angular velocity of fragmented dendrite during the simulation are depicted in Figure 55. The results show that the fragmented branch moves alongside the streamline, which is reasonable due to the small size of the fragment and the fact that the liquid and solid alloy density is almost

the same. The order of magnitude of velocity is also estimated to be around 2.0 mm/s near the void. During this motion, it also rotates initially clockwise and later counterclockwise, driven by the resulting moment acting on the fragmented dendrite.

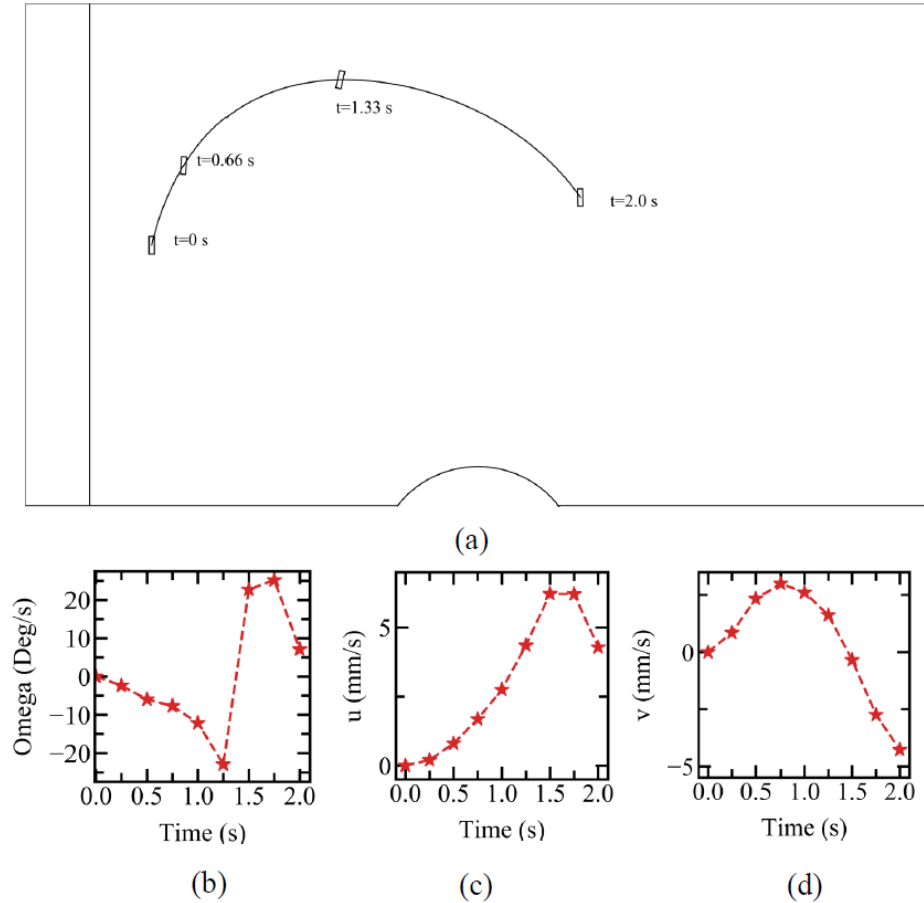


Figure 55. Rotation and velocity components of fragmented dendrite caused by Marangoni convection during 2 seconds of simulation for MICAST in the presence of 2.5 mm diameter bubble (a) rotation of fragmented dendrites, (b) the angular velocity, (c), and (d) velocity component in x and y direction respectively.

For the larger 11-mm long adhered bubble (Figure 12(a) and Figure 51(a)), the temperature and streamlines are shown in Figure 56. The larger Ma number for the longer bubble (2016 vs. 104) results in more severe distortion of isotherms than the smaller 2.5 mm diameter bubble (Figure 54). Furthermore, at $t=2$ s, two primary vortices are

observed. The left one is counterclockwise, and the right one is clockwise. Even though the bulk velocity in the bubble's vicinity is large, it is reduced near the S/L interface or inside the mushy zone. As other researchers suggested [8,132], the distortion of isotherms makes the top dendrites grow faster. It could even cause dendrites near the void to rotate away in the direction of induced flow [83,127].

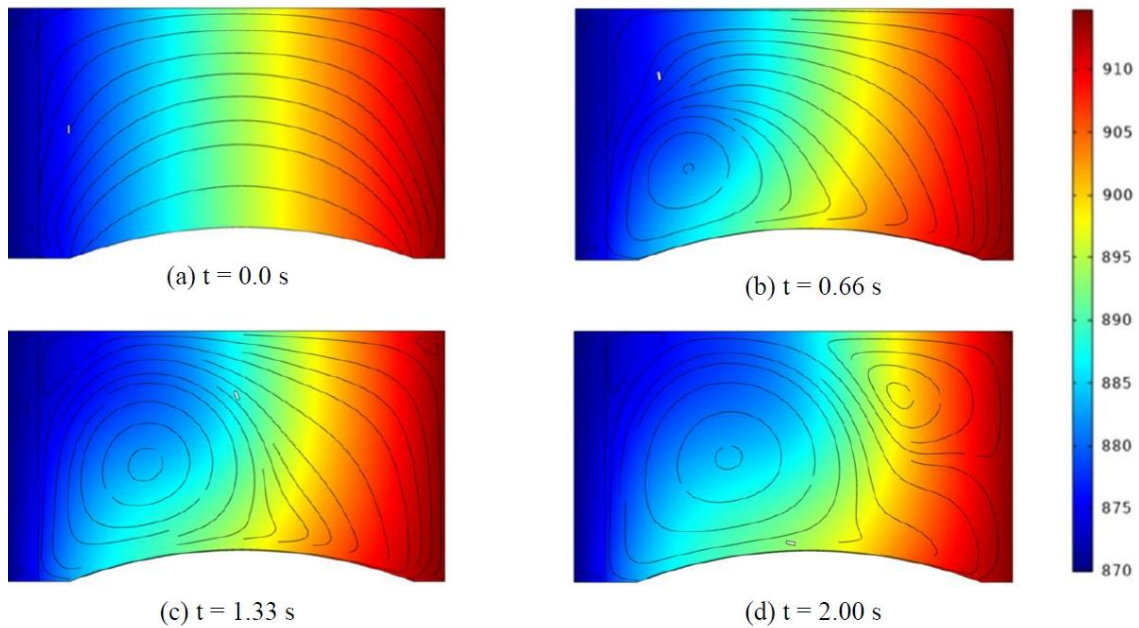
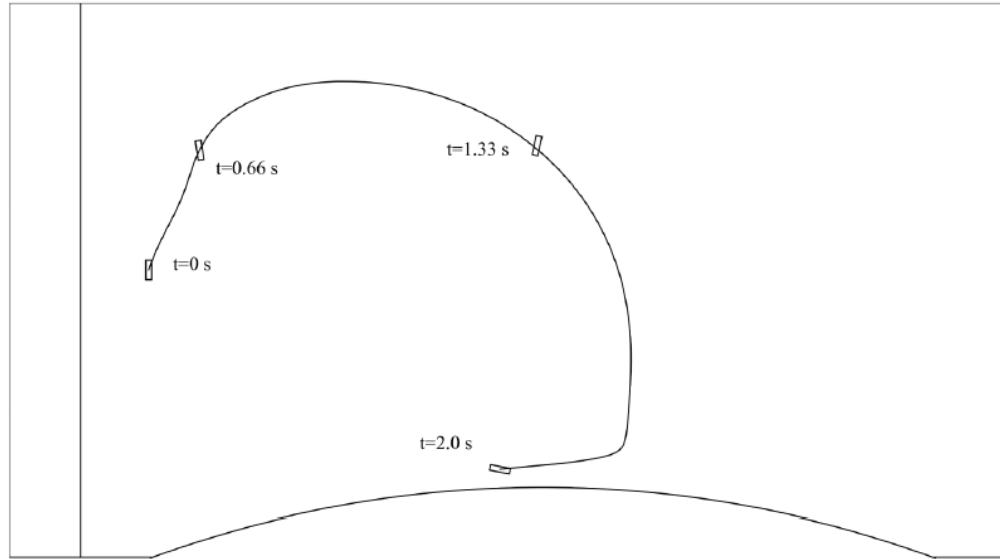


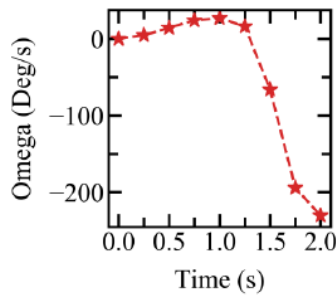
Figure 56. Simulation of the temperature field and streamlines for MICAST2-12 experiment (void length= 11 mm, $Ma= 2016$ and $G = 3200 \text{ K/ m}$) at (a) $t=0.0 \text{ s}$, (b) $t= 0.66 \text{ s}$, (c) $t=1.33 \text{ s}$, and (d) $t=2.0 \text{ s}$. The fragmented dendrite is shown with white rectangle.

As shown in Figure 57, the fragmented dendrite is also moving alongside the streamline. In this case, the order of magnitude of velocity is around 10 mm/s, as compared to 2 mm/s for the smaller 2.5 mm diameter void. The angular velocity is about 100 deg/s when the dendrite fragment approaches the bubble, as compared with about 10

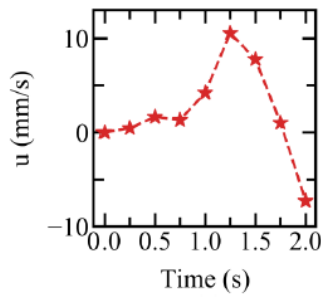
deg/s for the smaller void. The maximum speed of the fragment is observed near the void's free surface as the fragment comes toward the bubble.



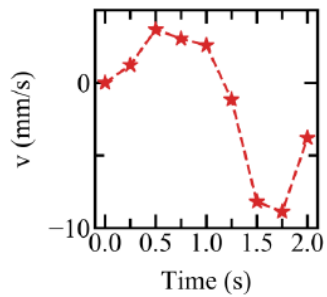
(a)



(b)



(c)



(d)

Figure 57. Rotation and velocity components of fragmented dendrite caused by Marangoni convection during 2 seconds of simulation for MICAST in presence of the 11 mm long void (a) rotation of fragmented dendrites, (b) the angular velocity, (c) and (d) velocity component in x and y direction respectively.

The comparison between angular velocity for PFMI and MICAST simulation results reveals that the convection strength depends on the Marangoni number and the location of the void with respect to the mushy zone. Although the order of magnitude of

Marangoni number is the same for the PFMI and MICAST with 2.5 mm diameter void, the angular velocity in MICAST is ten times larger (10 deg/s for MICAST vs. 1 deg/s for PFMI). For the PFMI case, the bubble was entrapped in the mushy zone which negate the induced convection. When the void is in front of the mushy zone as in MICAST cases, by increasing the Marangoni number by ten times, the angular velocity also increases with the same order.

Marangoni flow caused by the pores forming at the melt-crucible surface is strong enough to rotate the side-branch fragments coming in its path. For the Al-7 wt% Si MICAST2-12 sample, the side-branch fragments can move at 5 to 10 mm/s, which is two orders of magnitude higher than the 40 $\mu\text{m/s}$ growth speed of the solid-liquid interface. The significance of this flow is that a large dendritic array, gets its branches being detached by dissolution (likely in the necked, negative curvature regions where dendrite arms initiate) and rotate, and eventually form a misoriented grain [130,133]. Therefore, it is not surprising that misoriented spurious grains were observed in the MICAST 6, 7 and 2-12 samples, even though they were directionally solidified in the low gravity environment of space. It is crucial that a mechanism such as piston-spring assembly be used to keep the melt continually pressed onto the solid forming from it in order to eliminate the possibility of melt-ampoule detachment.

5.7. Three-Dimensional Phase Field Modeling of Columnar to Equiaxed Transition

Another mechanism responsible for the formation of misaligned microstructure that can occur both in microgravity and terrestrial conditions is the nucleation of solid

crystals in the melt ahead of the columnar zone. When the number of grains and the volume they occupy become large enough to block the columnar solidification front, columnar to equiaxed transition (CET) occurs. Although not directly relevant to Marangoni convection, CET is included in this dissertation because it is important to differentiate this mechanism of possible microstructure alteration from the one produced by surface-driven convection. Understanding the CET is vital in production of materials with superior properties using casting, welding, and additive manufacturing processes. In this dissertation, a three-dimensional (3D) phase field-lattice Boltzmann (PF/LB) model was developed to simulate the CET in directional solidification of Inconel 718 alloy. The phase field (PF) method was used to determine the solid/liquid transition. The solute diffusion equation was solved by the lattice Boltzmann method (LBM), due to its suitability for parallel processing and its simplicity in terms of modeling complex boundaries. A CET solidification map was developed for different temperature gradients and growth rates and the evolution of dendrites for equiaxed, columnar, and mixed regimes were studied. The resulting microstructure for different growth regimes was demonstrated and discussed in terms of grain size and orientation. In addition, the variation of maximum solute concentration along the sample height was investigated. It was found that while initial grain size does not affect the average grain size for equiaxed growth, it affects the primary dendrite arm spacing (PDAS) for columnar growth significantly. A model was proposed to predict the primary dendrite arm spacing for columnar growth in a wide range of temperature gradient, solidification rate, and initial grain size. The novelty of this model is in the inclusion of the effect of initial grain size,

which is important in processes that involve melting and solidification on a preexisting substrate, such as welding and additive manufacturing.

A number of theoretical and empirical models have been developed by researchers for the prediction of the CET. Hunt [134] assumed that in directional solidification, the equiaxed grain could grow if there is a constitutional undercooling zone in front of the interface. Hunt found a correlation between the lower and higher bounds of the temperature gradient, G , in the liquid for fully columnar growth to occur. If the volume fraction of equiaxed grains is less than 0.0066 ($\varphi < 0.0066$), the CET will not happen. Hunt found the temperature gradient corresponding to this condition to be:

$$G > 0.617(100N_0)^{\frac{1}{3}}\left(1 - \frac{\Delta T_n^3}{\Delta T^3}\right)\Delta T \quad (71)$$

When the volume fraction of equiaxed grains is greater than 0.49 ($\varphi > 0.49$), the corresponding upper bound of G , for fully equiaxed growth to occur, was found to be:

$$G < 0.617(N_0)^{\frac{1}{3}}\left(1 - \frac{\Delta T_n^3}{\Delta T^3}\right)\Delta T \quad (72)$$

Where G is temperature gradient and V_p is the growth rate, the cooling rate can be defined as: $\frac{\partial T}{\partial t} = G \times V_p$. N_0 is the total number of heterogeneous substrate particles originally available for nucleation per unit volume. The local constitutional undercooling is defined as $\Delta T = T_l(C) - T$, where $T_l(C)$ is the liquidus temperature corresponding to the solute concentration and T is the local temperature. ΔT is the columnar front undercooling and ΔT_n is the instantaneous nucleation undercooling. At values of G between these two inequalities (Equations (71) and (72)), a mixed columnar–equiaxed structure is expected.

The extended volume fraction of equiaxed grains, φ , is defined as:

$$\varphi = 1 - \exp\left(-\frac{4}{3}\pi r^3 N_0\right) \quad (73)$$

where r is the radius of the equiaxed grain given by:

$$r = \int_0^t V_p dt \quad (74)$$

Gaumann et al [135] extended the Hunt model to rapid solidification by considering the non-equilibrium effects. The final results were presented as:

$$\frac{G^n}{V_p} = a \left[\frac{1}{n+1} \left(\frac{-4}{3} \frac{\pi N_0}{\ln(1-\varphi)} \right)^{1/3} \right]^n \quad (75)$$

Comparing with the experiments, Knapp et al [136] found the constants in Equation (75) for Inconel 718 alloy to be $a=4.5 \text{ K}^2\text{s}/\text{m}$, $n=2$, and $N_0 = 2.65 \times 10^{14} \text{ m}^{-3}$. With these parameters, the conditions for fully equiaxed and fully columnar grain formation were calculated as:

$$\frac{G^2}{V_p} < 6.98 \times 10^9 \frac{\text{K}^2\text{s}}{\text{m}^3} \text{ for fully equiaxed} \quad (76)$$

$$\frac{G^2}{V_p} > 1.52 \times 10^{11} \frac{\text{K}^2\text{s}}{\text{m}^3} \text{ for fully columnar} \quad (77)$$

Again, if the value of $\frac{G^2}{V_p}$ is between these two values, a mixed columnar–equiaxed structure is expected.

The primary dendrite arm spacing (PDAS) in the microstructure of directionally solidified alloys is one of the common metrics utilized for validation purposes. The PDAS is known to be related to material properties including fatigue strength and creep [137,138]. Several analytical models have been proposed to predict the PDAS given the

temperature gradient (G) and the growth rate (V_p). It should be mentioned that expecting to have a single value for primary arm spacing based on solidification parameters (cooling rate, temperature gradient, etc.) is not realistic. The arm spacing is rather history dependent. In other words, instead of a single value of the arm spacing, a family of solutions is observed. The arm spacing belongs to a continuous interval, between a minimum value below which primary branches eliminate, and a maximum value above which the tertiary branching mechanism takes place (see Gurevich and Karma [139]). Therefore, the arm spacing has an allowance range even for a defined solidification condition rather than a single number [140,141].

Nastac et al. [142] suggested the following expression for PDAS.

$$\lambda_1 = \mu_{PDAS} G^{-0.5} R^{-0.25} \quad (78)$$

where μ_{PDAS} is a microstructural coefficient, found to be $\mu_{PDAS} = 2.21 \times 10^{-3}$ for Inconel 718. Weidong et al. [141] proposed that the PDAS can be described as:

$$\lambda_1 = a\varepsilon^{-b} \quad (79)$$

where a and b are material dependent and ε is the cooling rate defined as $\frac{\partial T}{\partial t} = G \times V_p$.

For Inconel 718, $a \approx 50 \mu m K s^{-1}$ and $b=1/3$. In another model by Kurtz-Fisher [143], it was proposed that PDAS could be predicted as:

$$\lambda_1 = 4.3 \Delta T_n^{0.5} \left(\frac{D_l \Gamma}{\Delta T_0 k} \right)^{0.25} G^{-0.5} V_p^{-0.25} \quad (80)$$

where ΔT_n is the non-equilibrium solidification range for Inconel 718, D_l is the diffusion coefficient in the liquid, Γ is the Gibbs-Thomson coefficient, ΔT_0 is the

equilibrium solidification temperature range, and k is the partition coefficient. Finally, Trivedi [144] proposed the following equation for PDAS predictions:

$$\lambda_1 = 2.83(L\Delta T_0 k D_l \Gamma)^{0.25} G^{-0.5} V_p^{-0.25} \quad (81)$$

where L is the constant of harmonic perturbation.

Taking Inconel 718 alloy as an example, each of the aforementioned models predicts a different PDAS for identical processing conditions.

During solidification, due to the difference in solubility of Nb in the solid and liquid phase, solute partitioning occurs. The amount of solute rejected from the solidifying cells at each time-step can be calculated as:

$$\Delta C_l = \frac{\Delta \phi}{2} C_l^e (1 - k) \quad (82)$$

The rejected solute is then evenly redistributed among the surrounding liquid and interface cells in order to conserve the total solute content. Once the solute concentration is known in each node, the supersaturation variable can be calculated using Equation (54) [105]. No-slip bounce-back boundary condition was implemented for solute transport equation at the solid/liquid interface, while zero-flux boundary condition was applied for all domain walls.

In the absence of solid movement in the liquid, the number of solid crystals that nucleate in the bulk liquid per time step can be calculated as [145,146]:

$$\frac{\partial N_l}{\partial t} = -2\mu_N \Delta T \left(\frac{\partial T}{\partial t} \right) (1 - f_s) \quad (83)$$

where f_s is the fraction of solid, defined as $f_s = (1 + \phi)/2$.

$$dp_i = \frac{\partial N_l}{N^{l_0}} \quad (84)$$

where N^{l_0} is the number of liquid nodes in the domain. The nodes are considered to be liquid when $\phi < -0.9$. Once the probability of nucleation (dp_i) is found, it is compared to a random number between 0 and 1, generated in each node. If the generated random number is less than dp_i , then the nucleation occurs for that node.

Twenty-eight cases were simulated in a wide range of temperature gradients and solidification rates. The temperature gradient ranged from 10 K/m to 10^7 K/m, and the solidification rate ranged from 10^{-4} m/s to 10^{-1} m/s, which covers conditions experienced in most of the industrial solidification processes. A solidification map was developed based on the simulation results. Table 2 lists the processing conditions, G and V_p , for each of the cases along with the resulting solidification structure, i.e., columnar, equiaxed, or mixed. The solidification map is plotted in Figure 58. The solid line in the figure is based on the analytical model presented in Equations (71) and (72).

In the columnar microstructure, slender dendrites can be observed in the direction of temperature gradient, but in the equiaxed regime, the dendrites are randomly distributed and oriented in the domain with comparable arm lengths. The difference can be explained by the availability of nucleation sites in each case. In the equiaxed regime, there is a large, undercooled region in the melt allowing for nucleation to occur. However, in columnar growth, due to high-temperature gradient, the undercooling is not large enough for nucleation to occur. The present model with the proposed nucleation model can reasonably predict different solidification regimes as is shown in Figure 58.

Out of 28 cases, only 3 examples are shown here to represent 3 different solidification regimes.

Table 10. Simulation conditions and final grain structures predicted by the present model for directional solidification of Inconel 718 alloy.

Case	G (K/m)	V _p (m/s)	Simulated Structure
1	1e1	1e-1	Equiaxed
2	1e2	1e-1	Equiaxed
3	1e3	1e-1	Equiaxed
4	1e4	1e-1	Equiaxed
5	1e5	1e-1	Columnar
6	1e6	1e-1	Columnar
7	1e7	1e-1	Columnar
8	1e1	1e-2	Equiaxed
9	1e2	1e-2	Equiaxed
10	1e3	1e-2	Equiaxed
11	1e4	1e-2	Mixed
12	1e5	1e-2	Columnar
13	1e6	1e-2	Columnar
14	1e7	1e-2	Columnar
15	1e1	1e-3	Equiaxed
16	1e2	1e-3	Equiaxed
17	1e3	1e-3	Equiaxed
18	1e4	1e-3	Columnar
19	1e5	1e-3	Columnar
20	1e6	1e-3	Columnar
21	1e7	1e-3	Columnar
22	1e1	1e-4	Equiaxed
23	1e2	1e-4	Equiaxed
24	1e3	1e-4	Mixed
25	1e4	1e-4	Columnar
26	1e5	1e-4	Columnar
27	1e6	1e-4	Columnar
28	1e7	1e-4	Columnar

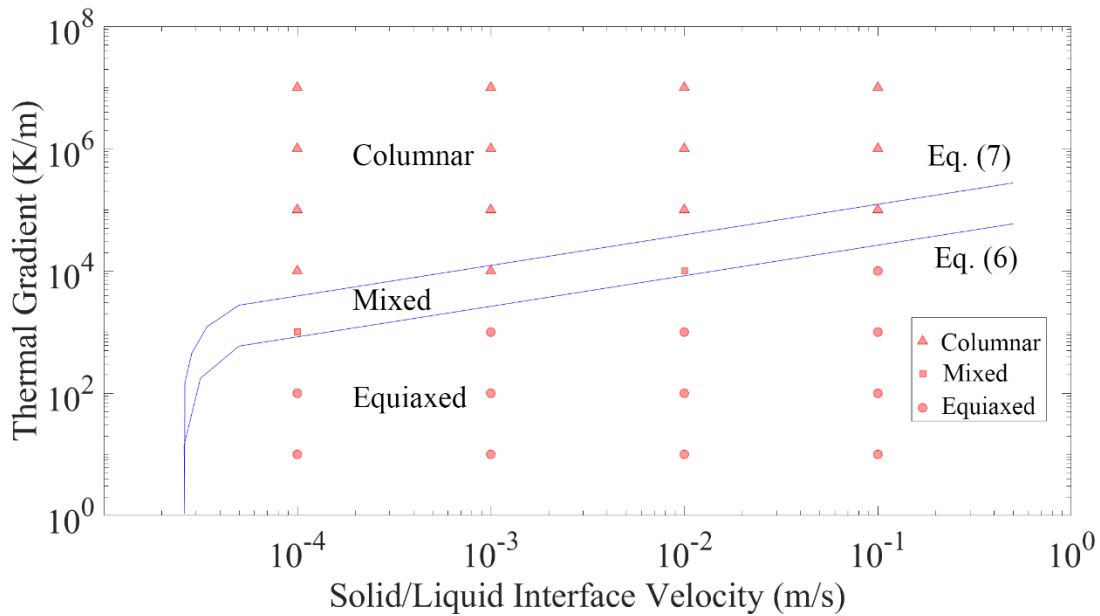


Figure 58. The simulated solidification map for Inconel 718 alloy. The solid lines show the predictions based on Equations (76) and (77). [147]

Figure 59 demonstrates the growth morphology for different solidification regimes. Figure 59 (a-c) shows a columnar microstructure for $G = 10^6$ K/m and $V_p = 10^{-3}$ m/s, which corresponds to a cooling rate of 10^3 K/s, a condition similar to what often happens in powder-bed metal additive manufacturing processes [136]. Figure 59 (g-i) shows the results for $G = 10^2$ K/m, $V_p = 10^{-1}$ m/s, and cooling rate of 10 K/s, which results in an equiaxed microstructure. The seeds at the bottom of the domain start to grow initially, but then new seeds nucleate and grow in the liquid. The new seeds in front of the solid/liquid interface obstruct the growth of the bottom columnar dendrites. The mixed regime, shown in Figure 59 (d to f), corresponds to $G = 10^4$ K/m, $V_p = 10^{-2}$ m/s and cooling rate of 10^2 K/s. In this case, nucleation occurs in front of the solid/liquid interface, but the new misoriented dendrites cannot completely block the growth of the

columnar dendrites. The columnar to equiaxed transition is promoted by decreasing the temperature gradient and increasing the solidification rate.

The 2D solute concentration and grain orientation maps for the mid-section of the domain is demonstrated in Figure 60. Electron backscatter diffraction (EBSD) is a popular microscopy technique applied to reveal microstructure information including crystallographic orientation. Our output results are compatible with EBSD format; therefore, it can be used in any library or software that analyzes the EBSD as the input file. To visualize our results, we used the MTEX library which is a free MATLAB toolbox for analyzing and modeling crystallographic textures by means of EBSD or pole figure data [148].

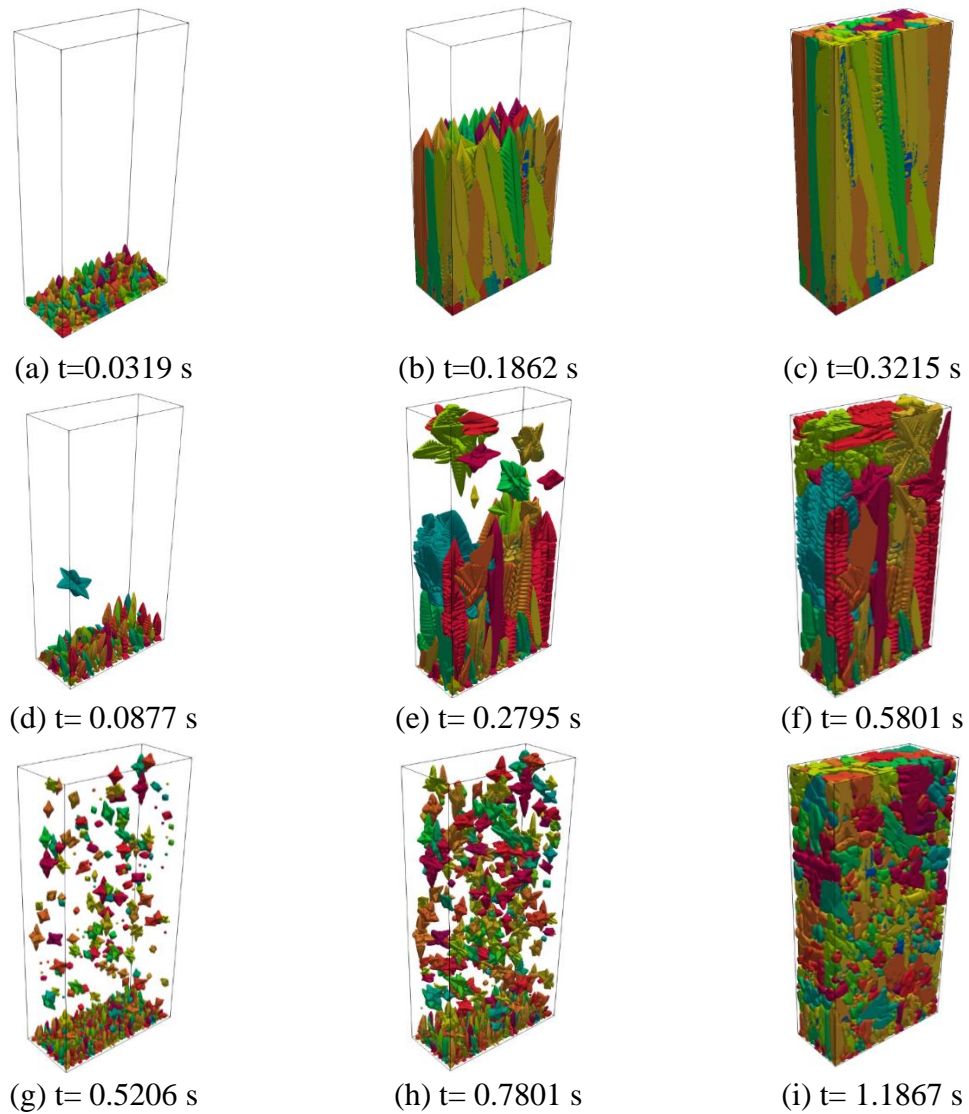


Figure 59. Evolution of dendrites with time for different solidification regimes: (a-c) columnar: $G=10^6$ K/m and $V_p=10^{-3}$ m/s, (d-f) mixed: $G=10^4$ K/m and $V_p=10^{-2}$ m/s, (g-i) equiaxed: $G=10^3$ K/m and $V_p=0.1$ m/s when initial grain seeds distance equals to $12 \mu\text{m}$.

For columnar growth in Figure 60 (a-b), the dendrites with crystallographic orientations parallel to the temperature gradient overgrow the others. As a result of this competitive growth, the dendrites are almost parallel to each other in the upper section of the domain. For mixed growth in Figure 60 (c-d), two different regions can be observed. The first region is in the lower section of the domain, where the columnar dendrites with

orientation near the temperature gradients are dominant. The second region is in the upper section of the domain, with mostly equiaxed dendrites. For equiaxed growth in Figure 60 (e-f), the domain is filled with equiaxed dendrites except for a thin region at the bottom.

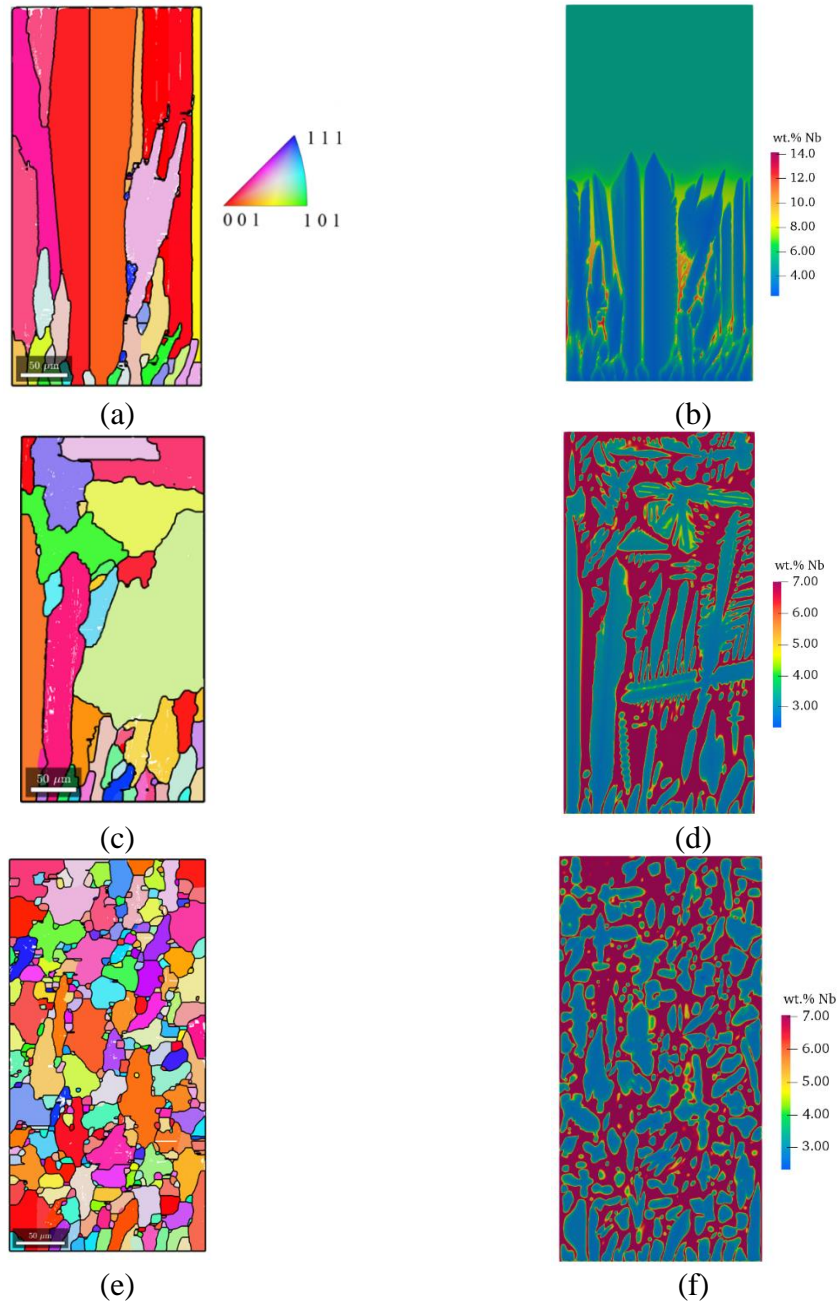


Figure 60. Grain orientation and solute maps for a cross-sectional plane passing through the middle Y-axis, (a) final grain structure at $t= 0.3215$ s and (b) solute field at $t= 0.1862$ s for $G=10^6$ K/m and $V_p=0.001$ m/s, (c) final grain structure at $t= 0.5801$ s and (d) solute field at $t= 0.2795$ s for $G=10^4$ K/m and $V_p=10^{-2}$ m/s, (e) final grain structure at $t=1.1867$ s and (f) solute field at $t= 0.7801$ s for $G=10^2$ K/m and $V_p=0.1$ m/s when initial grain seeds distance equals to $12 \mu\text{m}$.

The corresponding Nb concentration for different regimes in the middle of solidification is also demonstrated in Figure 60. The solute concentration is higher in the interdendritic region for columnar growth compared to mixed or equiaxed growth. In columnar growth, liquid may get trapped in the interdendritic region, preventing Nb to be diluted to the liquid away from the solidification front. In the mixed or equiaxed growth, the interdendritic solute entrapment is not significant, resulting in a lower interdendritic concentration of Nb.

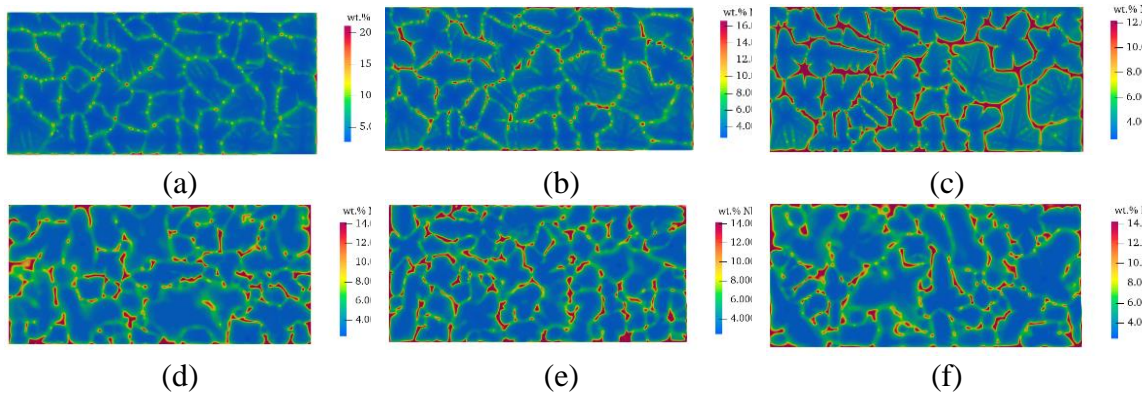


Figure 61. Solution map for columnar (a to c) at $t = 0.3215$ and equiaxed growth (d to e) at $t = 1.1867$ s at different heights of the sample. (a) and (d) correspond to $Z = 0.1$ mm, (b) and (e) correspond to $Z = 0.2$ mm and (c) and (f) correspond to $Z = 0.3$ mm

The solute concentration of Nb at the end of solidification also provides useful information about material properties such as hot cracking resistance. It is known that Inconel 718 melt with Nb concentration less than 23 wt.% transforms into the austenite phase (c) and with a Nb concentration greater than 23 wt.% transforms into the eutectic phase (c + Laves phase) [149]. The hot cracking resistance is reduced in the microstructure that contains long continuous chains of Laves phase. Avoiding the long continuous Laves phase can improve the hot cracking resistance of Inconel 718 alloy [150]. Figure 61 shows the solute concentration at different heights of the sample domain

for columnar and equiaxed regimes when the solid fraction is equal to 0.9. The solid fraction was defined as the ratio of the number of solid nodes in the domain to the total number of nodes. For columnar growth in Figure 61 (a to c,) the same microstructure pattern can be seen in different cross-sections. The observation verifies that only dendrites with crystallographic orientation close to the temperature gradient survive during solidification. On the other hand, in the equiaxed growth, each cross-section has its unique pattern of microstructure. The observation confirms that the nucleation of new seeds in the equiaxed regime is responsible for the resulted microstructure pattern. The contour legends in Figure 4 are adjusted based on the maximum solute concentration: 20.85 wt.% for columnar at $Z=0.1$ mm (Figure 4 (a)), 16.73 wt.% for columnar at $Z=0.2$ mm (Figure 61 (b)), 12.45 wt.% for columnar at $Z=0.3$ mm (Figure 61 (c)), and 14.3 wt.% for equiaxed at all heights (Figure 61 (d-f)). The growth regime can significantly affect the solute segregation in the domain. While the maximum concentration significantly varies from the bottom to the top of the domain in case of columnar growth, it remains the same at different heights for the equiaxed case.

The maximum solute concentration for different growth regimes is plotted in Figure 62. The variation of maximum solute along the Z-axis reveals the mechanism of liquid entrapment in the interdendritic region. In all cases, interdendritic regions with a high solute concentration can be identified; they are scattered through the domains and are the last regions in which solidification takes place. The difference between the maximum value in different regimes can be explained in twofold. First, in columnar growth, especially at the bottom of the domain, two neighboring dendrites have different

preferred crystalline orientations; therefore, they can enclose a comparatively large amount of liquid in the interdendritic region compared to equiaxed or mixed growth. The amount of enclosed melt is responsible for the final maximum concentration of Nb. Second, in the upper part of the columnar growth case, the dendrites grow faster since they almost grow parallel to each other, giving less time to Nb concentration to build up. Similar observations were also reported by other scholars [150].

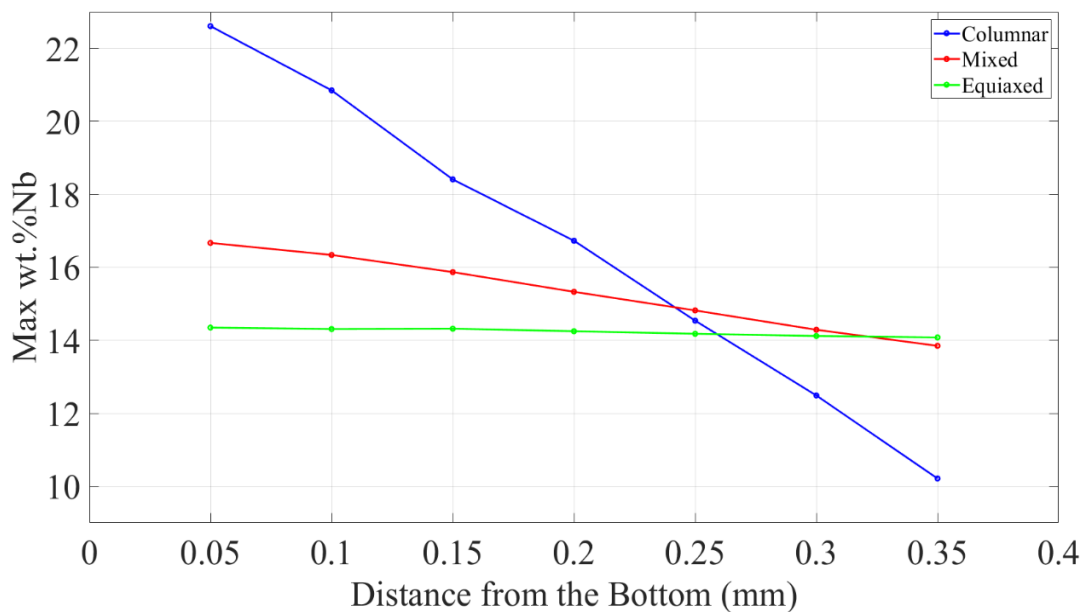


Figure 62. Maximum solute concentration for different growth regime at different vertical distances when the solid fraction in the whole domain is 0.9.

The effect of cooling rate on the microstructure was also investigated. As expected, the model predicts a finer microstructure for all regimes when the cooling rate increases. The effect of increasing the cooling rate on columnar growth is presented in Figure 63. for three processing conditions. The simulated primary dendrite arm spacing (PDAS) shows an inverse relation to the cooling rate. For the cooling rates of 100,

1000,10000 K/s, the simulated average PDAS was measured to be 40.2, 25.6, and 19.1 μm , respectively.

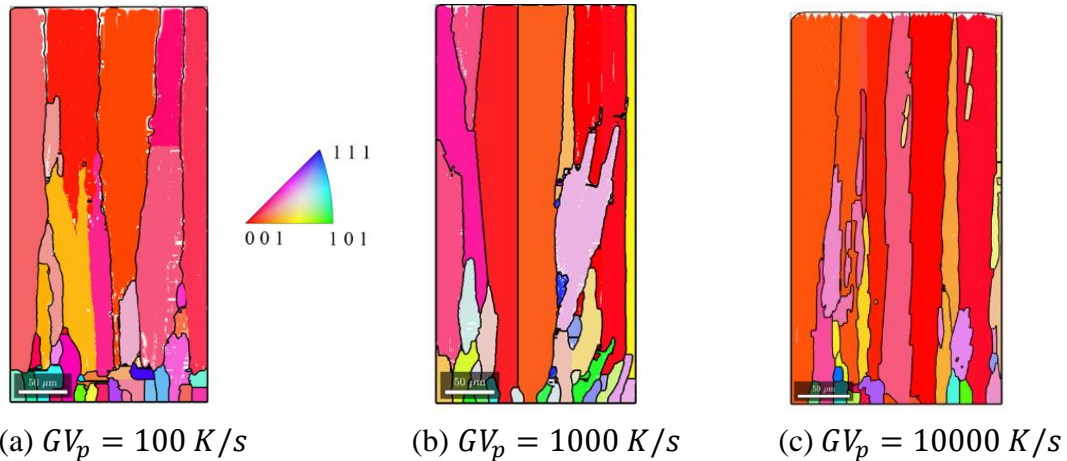


Figure 63. Columnar grain structure for a) $GV_p=100 \text{ K/s}$, b) $GV_p=1000 \text{ K/s}$, c) $GV_p=10000 \text{ K/s}$ when initial grain seeds distance equals to $12 \mu m$.

In equiaxed growth, increasing the cooling rate increases the probability of nucleation, according to Equation (83), which leads to a finer microstructure. Three examples of equiaxed microstructures with three different cooling rates are presented in Figure 64. For the cooling rates of 10, 100,1000 K/s, the average grain size was measured to be 40.32, 28.6, and $6.34 \mu m$, respectively.

The predicted PDAS values from this dissertation were compared with previous analytical models introduced. Table 11 shows a summary of the results. Each model predicts that by increasing the cooling rate, the PDAS would decrease. The simulated results have the same order of magnitude compared to other analytical models.

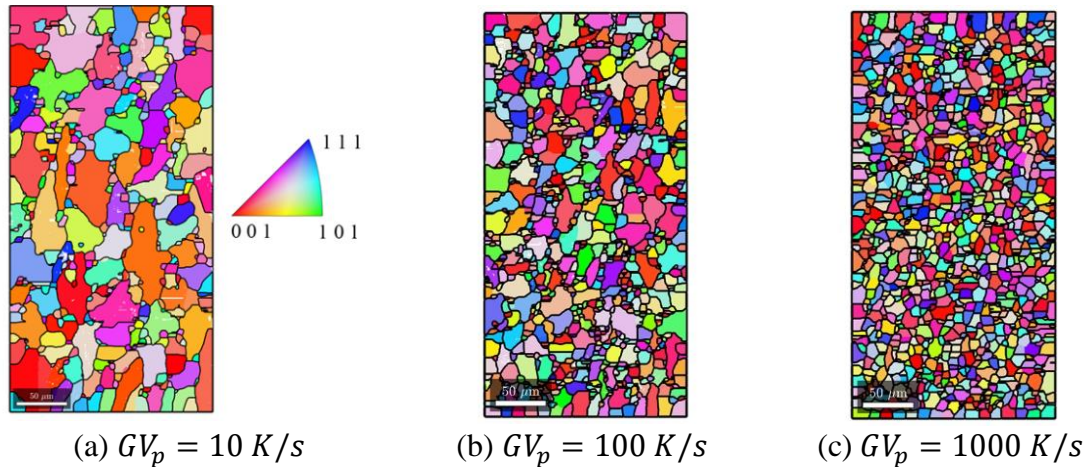


Figure 64. Equiaxed grain structure for a) $GV_p=10 \text{ K/s}$, b) $GV_p=100 \text{ K/s}$, c) $GV_p=1000 \text{ K/s}$ when initial grain seeds distance equals to $12 \mu\text{m}$.

Nevertheless, it is observed that there is a rather wide variation in the values predicted by different models for the same cooling rate. This large variation implies that there are other parameters besides solidification rate and temperature gradient that affect grain morphologies. At the beginning of each simulation, randomly oriented seeds are placed at the bottom of the domain with a predefined spacing. The density and spacing of the initial seeds can alter the eventual PDAS in the material. The initial seed spacing (grain size), and distribution can reproduce the size of preexisting grains in the substrate, for example in welding and additive manufacturing processes. To verify this hypothesis, we studied the effects of initial seed spacing on the microstructure for both growth regimes.

Table 12 shows the effect of initial grain size (IGS) on the microstructure for columnar growth when the cooling rate varies from 10 to 10000 K/s . The initial grain size was chosen as 6, 12, and $18 \mu\text{m}$. It was observed that the IGS has a strong influence on the average PDAS; a finer initial grain size leads to smaller average PDAS. The

difference is more evident for the higher cooling rates. As reported by Boussinot et al. [151], by increasing the cooling rate, usual spacing selection mechanisms are inhibited, and the dendritic structure remains strongly influenced by the initial conditions. The same trend is also observed here concerning the PDAS.

Table 11. Comparison of analytical PDAS $\lambda_1(\mu\text{m})$ predictions to the present model.

Models	Cooling rate (K/s)		
	100	1000	10000
Nastac [145]	39.3	12.4	3.9
Huang [140]	10.8	5.0	2.3
Kurtz-Fisher [143]	131.3	41.5	13.1
Trivedi [144]	99.8	31.6	9.9
Lenart-Eshraghi [152]	44.2	27.6	22.1
Present	40.2±3.75	25.6±4.74	19.1±4.89

Thirty-six cases were simulated for three different temperature gradient levels, four solidification rate levels, and three initial grain size levels. The strength of relations between cooling rate, temperature gradient, solidification rate, initial seed spacing, and PDAS can be represented numerically by Pearson's correlation coefficient. Pearson's correlation coefficient can take values between [-1, 1], where values greater than zero represent a positive correlation between variables. A positive correlation between two variables means that when the value of one variable increases, the other variable also increases. Zero means no correlation, and negative values denote negative (opposite) correlation. The stronger the relationship of the two variables, the closer the Pearson correlation coefficient would be to either +1 or -1. The results are summarized in Table 13.

Table 12. Effect of different initial grain size on PDAS for columnar growth at different cooling rates.

Cooling Rate	Initial Grain Size		
	6 μm	12 μm	18 μm
10 K/s ($V_p=10^{-4}$ m/s, $G = 10^5$ K/m)	47.1 \pm 7.3	51.1 \pm 6.9	56.4 \pm 7.0
10 ² K/s ($V_p=10^{-4}$ m/s, $G = 10^6$ K/m)	37.5 \pm 5.9	39.3 \pm 4.5	43.5 \pm 4.2
10 ² K/s ($V_p=10^{-3}$ m/s, $G = 10^5$ K/m)	36.3 \pm 6.8	40.2 \pm 3.8	46.2 \pm 5.1
10 ³ K/s ($V_p=10^{-4}$ m/s, $G=10^7$ K/m)	30.3 \pm 4.7	34.5 \pm 5.2	39.4 \pm 6.3
10 ³ K/s ($V_p=10^{-3}$ m/s, $G=10^6$ K/m)	20.5 \pm 6.6	25.6 \pm 4.7	37.6 \pm 5.9
10 ³ K/s ($V_p=10^{-2}$ m/s, $G=10^5$ K/m)	18.2 \pm 3.5	25.1 \pm 5.6	32.6 \pm 7.2
10 ⁴ K/s ($V_p=10^{-3}$ m/s, $G=10^7$ K/m)	9.1 \pm 4.2	19.1 \pm 4.9	25.1 \pm 3.6
10 ⁴ K/s ($V_p=10^{-2}$ m/s, $G=10^6$ K/m)	16.7 \pm 3.4	25.1 \pm 4.2	31.41 \pm 4.4
10 ⁴ K/s ($V_p=10^{-1}$ m/s, $G=10^5$ K/m)	19.45 \pm 5.3	28.69 \pm 4.1	31.73 \pm 5.2
10 ⁵ K/s ($V_p=10^{-2}$ m/s, $G=10^7$ K/m)	12.3 \pm 2.1	20.1 \pm 4.5	29.1 \pm 4.3
10 ⁵ K/s ($V_p=10^{-1}$ m/s, $G=10^6$ K/m)	10.9 \pm 4.3	18.1 \pm 5.3	23.2 \pm 4.8
10 ⁶ K/s ($V_p=10^{-1}$ m/s, $G=10^7$ K/m)	8.3 \pm 3.9	13.0 \pm 4.9	15.4 \pm 5.3

Table 13. Correlation matrix showing pairwise correlation Pearson's coefficient between variables.

	<i>PDAS</i>	<i>IGS</i>	<i>G</i>	<i>V_p</i>
<i>PDAS</i>	1.000	0.4104	-0.3836	-0.5522
<i>IGS</i>	0.4104	1.000	0.000	0.000
<i>G</i>	-0.3836	0.000	1.000	0.000
<i>V_p</i>	-0.5522	0.000	0.000	1.000

Obviously, the correlation coefficient between a variable and itself (main diagonal in Table 13) is one. For the independent variable pairs, such as cooling rate and temperature gradient, the correlation is zero. The relationship between PDAS and IGS is quite strong. By implementing different curve fitting techniques and multiple linear regression analysis, we propose the following equation to predict PDAS as a function of G , V_p and IGS .

$$PDAS = 0.0193 IGS^{0.5166} G^{-0.1110} V_p^{-0.1351} \quad (85)$$

The R-squared value was calculated as 0.877, which means the model fits the data series well. It should be noted that the effect of cooling rate is embedded in temperature gradient and solidification rate. In comparison with the models presented in Equations (78), (80), and (81), our model also includes the effect of initial grain size, which shows a significant effect based on our simulation results. This can be very useful for processes in which melting and solidification take place on a preexisting substrate. One potential application of our model is in predicting grain morphology in welding and additive manufacturing processes, based on the solidification parameters where initial grain size represents the substrate grain structure. The model is valid in a wide range of temperature gradient, solidification rate, and initial grain size ($10^5 \text{ K/m} \leq G \leq 10^7 \text{ K/m}$, $10^{-4} \text{ m/s} \leq V_p \leq 10^{-1} \text{ m/s}$, $6 \mu\text{m} \leq \text{IGS} \leq 18 \mu\text{m}$).

On the other hand, different trends are observed for equiaxed grains, as it is shown in Table 14. In contrast to columnar growth, the initial grain size does not affect the final grain size for the same cooling rate. The results indicate that the nucleation rate has a dominant effect on the final grain size, whereas the initial seed spacing at the bottom of the domain does not seem to affect the average grain size.

Table 14. Effects of initial grain size on the final grain size for equiaxed growth at different cooling rates.

Cooling Rate	Initial Grain Size		
	$6 \mu\text{m}$	$12 \mu\text{m}$	$18 \mu\text{m}$
10 K/s ($V_p=0.1 \text{ m/s}$, $G = 100 \text{ K/m}$)	39.64 ± 7.18	40.32 ± 4.66	37.98 ± 2.37
10^2 K/s ($V_p=0.1 \text{ m/s}$, $G = 10^3 \text{ K/m}$)	29.39 ± 7.65	28.6 ± 4.34	27.6 ± 5.74
10^3 K/s ($V_p=0.1 \text{ m/s}$, $G = 10^4 \text{ K/m}$)	7.12 ± 3.29	6.34 ± 4.19	7.7 ± 3.62

CHAPTER VI

CONCLUSION

In this dissertation, new computational models were developed to investigate the Marangoni convection induced by bubbles and voids formed by detachment of the melt from the mold and its effect on microstructural evolution during solidification. Parallel models using the CUDA GPU (graphics processing unit) and Message Passing Interface (MPI) techniques were created to perform these large-scale computationally demanding simulations. During the solidification under microgravity conditions and in the presence of a bubble, the variation in the liquid-gas surface tension at the free surface of the bubble can induce Marangoni convection. The data from PFMI and MICAST experiments conducted on the International Space Station were utilized to validate several aspects of the developed models.

The cellular automaton (CA) and Allen-Cahn Phase Field (PF) techniques were utilized to track the solid/liquid interface while lattice Boltzmann (LB) and finite difference (FD) were applied for the solute transport equation. The FD method and frozen temperature approximation were implemented for the energy equation. One of the challenges is how to model the bubble dynamics. Different categories of the lattice Boltzmann multiphase flow model were implemented to recover continuity and NS equations to simulate the effects of the bubble-dendrite interaction. The models include Shan-Chen based and Cahn–Hilliard (CH)-PF based LB method. The original Shan-Chen

model has already been studied for this problem by other researchers, but the results are limited to small density ratios between the fluid and gas phases, which do not correspond to real physical properties. In this dissertation, to attempt the simulation of higher density ratios and reduce the magnitude of the spurious current, several individual enhancements available for the original Shan-Chen model were, for the first time, used in a combined form to develop an enhanced version of the original model. It is found that the enhancements, including the use of a realistic equation of state, a high order isotropy force scheme, and a mid-range repulsion force, could improve the accuracy and capability of the original Shan-Chen method. Even with the implementation of all these enhancements, the spurious currents are still significant, which makes this enhanced model unsuitable for studying the Marangoni effect in many practical situations. A more reliable and accurate alternative is the phase field lattice Boltzmann method. Although computationally more expensive than the Shan-Chen model, it can produce accurate results not affected by spurious currents.

An enhanced model was implemented with the combination of all enhancements to validate the phase separation problem. Different phase separation scenarios regarding the bubble's coalescence were observed based on the selection of model parameters. For the phase field model validation, the Rayleigh instability problem was successfully solved with a low and high-density ratio.

It is shown that although Shan-Chen methods can replicate some qualitative features of bubble-dendrite interaction, the generated spurious current is unacceptably large, particularly for practical values of the density ratio between fluid and gas phases.

This occurred even after the implementation of several enhancements to the original Shan-Chen method. This severe limitation makes the Shan-Chen models unsuitable for simulating fluid flow phenomena such as Marangoni convection because the large spurious currents completely mask the physical flow. Therefore, it is still a long way until current Shan-Chen models can simulate phenomena in a microscale resolution with real physical properties. On the other hand, the phase field method is more accurate than the Shan-Chen model for simulation of fluids with a high-density ratio. It generates an acceptable small spurious current, though at the expense of higher computational costs.

PFMI and MICAST experiments and simulation results confirmed that Marangoni convection could produce non-homogeneity of the microstructure due to rotation of fragmented dendrite side-arms or rotation of primary dendritic arms from the original direction.

When a large bubble and the solid front are close enough, the induced Marangoni convection can alter the expected quiescent environment under the microgravity conditions, altering the microstructure. The effect of bubble size was investigated through large-scale simulations of dendrite growth. While no apparent effect on the microstructure was observed for small bubbles, the large bubbles altered the growth rate and tilted the dendrites in the direction of the fluid flow. Three regimes of growth were observed for dendrites based on the distance from the bubble. The details of these three regimes were discussed thoroughly. The simulations provided quantitative information about the effects of Marangoni convection on the microstructure.

Examination of PFMI microgravity experiment revealed that dendrites in the vicinity of a surface pore appear to rotate as if falling sideways. A model to predict the rotation of fragmented dendrites was developed and compared with the PFMI experiments. For the PFMI conditions, the simulation results predicted a rotation of 24° over 19 seconds of simulation for the fragmented side-arm compared to the 31.5° rotation observed in the PFMI videos. Then the same model to predict fragmented dendrites' trajectory motion in a different alloy, Al-7Si (MICAST), for small and large bubbles was utilized. The order of velocity magnitude for the fragmented dendrite was about 1 mm/s, which was hundred times larger than the rate of dendrite growth in those conditions.

Marangoni convection caused by detachment of melt column from the ampoule wall during directional solidification of alloys in the low-gravity environment of space station is intense enough to rotate broken-off dendrite fragments and lead to the formation of misoriented spurious grains. The strength of convection is dependent on the Marangoni number and location of the pore relative to the mushy zone. Formation of stray grains via fragmentation and rotation of side arms via Marangoni convection is also likely to be very important for some terrestrial solidification processes, such as laser fusion of powder beds used in additive manufacturing.

The results shed light on unexplained observations in the PFMI and MICAST experiments such as deviation of dendritic array from its original growth direction in the absence of terrestrial convection.

CHAPTER VII

POTENTIAL CONTINUATIONS

7.1. Adaptive Grid Refinement Method

In our simulation, both PF and CA models need relatively fine grids to capture the interface between phases. Additionally, phase field and energy equations are discretized by explicit finite difference method. By implementing adaptive grid refinements and using finer mesh for regions near the interface and coarser mesh for the rest of the domain, the computational time can be reduced significantly with still acceptable accuracy.

For LB and CA methods with no availability of explicit adaptive scheme suitable for parallel computing, we suggest using different meshes for solving different physics. More detail about the method can be found in our previous work [153]. The implementation of adaptive grid can enhance the capability of the model to simulate much larger domains.

7.2. Effect of Marangoni Convection on Microstructure Formation During Additive Manufacturing

Selective laser melting (SLM) is one of the primary types of procedures used in the additive manufacturing (AM) industry. This relatively new manufacturing process is

known to offer many advantages and opportunities over conventional methods. The developed large-scale model can be used to study the effects of various processing parameters and Marangoni convection on the solidified microstructures. The possible results of that study could help researchers to produce parts with desired microstructure.

7.3. Hybrid MPI-CUDA Approach

In our current model, the domain size is limited by available GPU memory. One solution is to use a GPU with larger memory. For larger domain sizes, implementing a hybrid parallel approach, in which CPU and GPU parallelization techniques are combined, can solve the memory problem. For implementation, the large system is divided into several subdomains. MPI is used to communicate data between each subdomain, which is assigned to one node. Each node then executes the GPU parallel simulation in the corresponding subdomain. Implementation of a hybrid MPI-CUDA will significantly reduce the computational time compared to the MPI model and will solve the memory problem of the single GPU programming approach.

BIBLIOGRAPHY

- [1] R.N. Grugel, A. V. Anilkumar, P. Luz, L. Jeter, M.P. Volz, R. Spievy, G. Smith, Toward understanding pore formation and mobility during controlled directional solidification in a microgravity environment investigation (PFMI), 2001 Conf. Exhib. Int. Sp. Stn. Util. (2001). <https://doi.org/10.2514/6.2001-5119>.
- [2] T.M. Pollock, W.H. Murphy, The breakdown of single-crystal solidification in high refractory nickel-base alloys, *Metall. Mater. Trans. A Phys. Metall. Mater. Sci.* 27 (1996) 1081–1094. <https://doi.org/10.1007/BF02649777>.
- [3] R.N. Grugel, L.N. Brush, A. V. Anilkumar, Disruption of an aligned dendritic network by bubbles during re-melting in a microgravity environment, *Microgravity Sci. Technol.* 24 (2012) 93–101. <https://doi.org/10.1007/s12217-011-9297-y>.
- [4] J. Hong, D. Ma, J. Wang, F. Wang, B. Sun, A. Dong, F. Li, A. Bührig-Polaczek, Freckle defect formation near the casting interfaces of directionally solidified superalloys, *Materials (Basel)*. 9 (2016) 929. <https://doi.org/10.3390/ma9110929>.
- [5] M.E. Glicksman, M.B. Koss, E.A. Winsa, Dendritic Growth Velocities in Microgravity, *Phys. Rev. Lett.* 73 (1994) 573–576. <https://doi.org/10.1103/PhysRevLett.73.573>.
- [6] O. Funke, G. Phanikumar, P.K. Galenko, L. Chernova, S. Reutzel, M. Kolbe, D.M. Herlach, Dendrite growth velocity in levitated undercooled nickel melts, *J. Cryst. Growth.* 297 (2006) 211–222. <https://doi.org/10.1016/j.jcrysgro.2006.08.045>.
- [7] J. Gao, M. Han, A. Kao, K. Pericleous, D. V. Alexandrov, P.K. Galenko, Dendritic growth velocities in an undercooled melt of pure nickel under static magnetic fields: A test of theory with convection, *Acta Mater.* 103 (2016) 184–191. <https://doi.org/10.1016/j.actamat.2015.10.014>.
- [8] S. Barsi, M. Kassemi, J.I.D. Alexander, Effects of void-induced convection on interface morphology and segregation during low-g solidification, *Int. J. Heat Mass Transf.* 47 (2004) 5129–5137. <https://doi.org/10.1016/j.ijheatmasstransfer.2004.05.024>.
- [9] R.N. Grugel, A. V. Anilkumar, Bubble formation and transport during directional solidification in microgravity: Model experiments on the space station, in: *AIAA Pap.*, 2004: pp. 6091–6096. <https://doi.org/10.2514/6.2004-627>.

- [10] Y.Z. Li, N. Mangelinck-Noël, G. Zimmermann, L. Sturz, H. Nguyen-Thi, Effect of solidification conditions and surface pores on the microstructure and columnar-to-equiaxed transition in solidification under microgravity, *J. Alloys Compd.* 749 (2018) 344–354. <https://doi.org/10.1016/j.jallcom.2018.03.300>.
- [11] A.D. Monde, O. Chawla, V. Kumar, S. Karagadde, P.R. Chakraborty, Shrinkage induced flow during directional solidification of pure substance in a bottom cooled cavity: A study on flow reversal phenomena, *Phys. Fluids.* 32 (2020). <https://doi.org/10.1063/5.0002953>.
- [12] A.G. Murphy, R.H. Mathiesen, Y. Houltz, J. Li, C. Lockowandt, K. Henriksson, N. Melville, D.J. Browne, Direct observation of spatially isothermal equiaxed solidification of an Al–Cu alloy in microgravity on board the MASER 13 sounding rocket, *J. Cryst. Growth.* 454 (2016) 96–104. <https://doi.org/10.1016/j.jcrysgr.2016.08.054>.
- [13] L. Abou-Khalil, G. Salloum-Abou-Jaoude, G. Reinhart, C. Pickmann, G. Zimmermann, H. Nguyen-Thi, Influence of gravity level on Columnar-to-Equiaxed Transition during directional solidification of Al – 20 wt.% Cu alloys, *Acta Mater.* 110 (2016) 44–52. <https://doi.org/10.1016/j.actamat.2016.03.007>.
- [14] G. Salloum-Abou-Jaoude, H. Nguyen-Thi, G. Reinhart, R.H. Mathiesen, G. Zimmermann, D. Voss, Characterization of motion of dendrite fragment by X-ray radiography on Earth and under microgravity environment, *Mater. Sci. Forum.* 790–791 (2014) 311–316. <https://doi.org/10.4028/www.scientific.net/MSF.790-791.311>.
- [15] H. Zhang, M. Wu, S.N. Tewari, A. Ludwig, A. Kharicha, Geometrical effect on macrosegregation formation during unidirectional solidification of Al–Si alloy, *J. Mater. Process. Technol.* 288 (2021) 116913. <https://doi.org/10.1016/j.jmatprotec.2020.116913>.
- [16] J.S. Langer, Instabilities and pattern formation in crystal growth, *Rev. Mod. Phys.* 52 (1980) 1–28. <https://doi.org/10.1103/RevModPhys.52.1>.
- [17] W.J. Boettinger, F.S. Biancaniello, S.R. Coriell, Solutal convection induced macrosegregation and the dendrite to composite transition in off-eutectic alloys, *Metall. Trans. A.* 12 (1981) 321–327. <https://doi.org/10.1007/BF02655205>.
- [18] K. Murakami, T. Fujiyama, A. Koike, T. Okamoto, Influence of melt flow on the growth directions of columnar grains and columnar dendrites, *Acta Metall.* 31 (1983) 1425–1432. [https://doi.org/10.1016/0001-6160\(83\)90012-3](https://doi.org/10.1016/0001-6160(83)90012-3).
- [19] E.A. Brener, Effects of surface energy and kinetics on the growth of needle-like dendrites, *J. Cryst. Growth.* 99 (1990) 165–170. [https://doi.org/10.1016/0022-0248\(90\)90505-F](https://doi.org/10.1016/0022-0248(90)90505-F).

- [20] B. Drevet, H. Nguyen Thi, D. Camel, B. Billia, M.D. Dupouy, Solidification of aluminum-lithium alloys near the cell/dendrite transition-influence of solutal convection, *J. Cryst. Growth.* 218 (2000) 419–433. [https://doi.org/10.1016/S0022-0248\(00\)00567-4](https://doi.org/10.1016/S0022-0248(00)00567-4).
- [21] Z. Min, J. Shen, Z. Feng, L. Wang, L. Wang, H. Fu, Effects of melt flow on the primary dendrite spacing of Pb-Sn binary alloy during directional solidification, *J. Cryst. Growth.* 320 (2011) 41–45. <https://doi.org/10.1016/j.jcrysgro.2011.01.013>.
- [22] W.U. Mirihanage, L. Arnberg, R.H. Mathiesen, In-situ observation of transient columnar dendrite growth in the presence of thermo-solutal convection, in: *IOP Conf. Ser. Mater. Sci. Eng.*, 2012. <https://doi.org/10.1088/1757-899X/33/1/012033>.
- [23] D. V. Alexandrov, P.K. Galenko, Dendrite growth under forced convection: analysis methods and experimental tests, *Uspekhi Fiz. Nauk.* 184 (2014) 833–850. <https://doi.org/10.3367/ufnr.0184.201408b.0833>.
- [24] R.N. Grugel, A. V. Anilkumar, C.P. Lee, Direct observation of pore formation and bubble mobility during controlled melting and re-solidification in microgravity, *Solidif. Process. Microstruct. A Symp. Honor Wilfried Kurz.* (2004) 111–116.
- [25] RUDY JF, RUPERT EJ, Effects of Porosity on Mechanical Properties of Aluminum Welds, *Weld J.* 49 (1970) 322. http://files.aws.org/wj/supplement/WJ_1970_07_s322.pdf%5Cnpapers3://publication/uuid/B0E1D22C-8E87-46B0-84E0-27996EC4A7DE (accessed March 25, 2019).
- [26] Q.G. Wang, D. Apelian, D.A. Lados, Fatigue behavior of A356-T6 aluminum cast alloys. Part I. Effect of casting defects, *J. Light Met.* 1 (2001) 73–84. [https://doi.org/10.1016/S1471-5317\(00\)00008-0](https://doi.org/10.1016/S1471-5317(00)00008-0).
- [27] Q.G. Wang, D. Apelian, D.A. Lados, Fatigue behavior of A356/357 aluminum cast alloys. Part II - Effect of microstructural constituents, *J. Light Met.* 1 (2001) 85–97. [https://doi.org/10.1016/S1471-5317\(00\)00009-2](https://doi.org/10.1016/S1471-5317(00)00009-2).
- [28] H.R. Ammar, A.M. Samuel, F.H. Samuel, Porosity and the fatigue behavior of hypoeutectic and hypereutectic aluminum-silicon casting alloys, *Int. J. Fatigue.* 30 (2008) 1024–1035. <https://doi.org/10.1016/j.ijfatigue.2007.08.012>.
- [29] R. Balasubramaniam, J.E. Lavery, Numerical simulation of thermocapillary bubble migration under microgravity for large reynolds and marangoni numbers, *Numer. Heat Transf. Part A Appl.* 16 (1989) 175–187. <https://doi.org/10.1080/10407788908944712>.
- [30] Q. Han, Motion of bubbles in the mushy zone, *Scr. Mater.* 55 (2006) 871–874.

<https://doi.org/10.1016/j.scriptamat.2006.07.052>.

- [31] H. Jamgotchian, R. Trivedi, B. Billia, Interface dynamics and coupled growth in directional solidification in presence of bubbles, *J. Cryst. Growth*. 134 (1993) 181–195. [https://doi.org/10.1016/0022-0248\(93\)90125-G](https://doi.org/10.1016/0022-0248(93)90125-G).
- [32] H. Xing, J.Y. Wang, C.L. Chen, K.X. Jin, Z.F. Shen, Morphological evolution of the interface microstructure in the presence of bubbles during directional solidification, *Scr. Mater.* 63 (2010) 1228–1231. <https://doi.org/10.1016/j.scriptamat.2010.08.043>.
- [33] I. Farup, J.M. Drezet, M. Rappaz, In situ observation of hot tearing formation in succinonitrile-acetone, *Acta Mater.* 49 (2001) 1261–1269. [https://doi.org/10.1016/S1359-6454\(01\)00013-1](https://doi.org/10.1016/S1359-6454(01)00013-1).
- [34] D.G. Kim, J.M. Kim, H.W. Kwon, C.R. Loper, Influence of gravity on the interaction between pore and solid/liquid interface, *J. Mater. Sci. Lett.* 19 (2000) 717–719. <https://doi.org/10.1023/A:1006735316744>.
- [35] J.M. Kim, D.G. Kim, H.W. Kwon, C.R. Loper, Pore behavior at the solid/liquid interface during solidification, *Scr. Mater.* 39 (1998) 969–975. [https://doi.org/10.1016/S1359-6462\(98\)00242-5](https://doi.org/10.1016/S1359-6462(98)00242-5).
- [36] J.M. Papazian, W.R. Wilcox, Interaction of bubbles with solidification interfaces, *AIAA J.* 16 (1978) 447–451. <https://doi.org/10.2514/3.60910>.
- [37] S.C. Hardy, The motion of bubbles in a vertical temperature gradient, *J. Colloid Interface Sci.* 69 (1979) 157–162. [https://doi.org/10.1016/0021-9797\(79\)90090-0](https://doi.org/10.1016/0021-9797(79)90090-0).
- [38] N.O. Young, J.S. Goldstein, M.J. Block, The motion of bubbles in a vertical temperature gradient, *J. Fluid Mech.* 6 (1959) 350–356. <https://doi.org/10.1017/S0022112059000684>.
- [39] R.N. Grugel, A. V. Anilkumar, M.C. Cox, Observation of an aligned gas - Solid “eutectic” during controlled directional solidification aboard the international space station - Comparison with ground-based studies, in: 43rd AIAA Aerosp. Sci. Meet. Exhib. - Meet. Pap., American Institute of Aeronautics and Astronautics, Reston, Virginia, 2005: pp. 14687–14694. <https://doi.org/10.2514/6.2005-919>.
- [40] M. Kassemi, S. Barsi, M. Kaforey, D. Matthiesen, Effect of void location on segregation patterns in microgravity solidification, *J. Cryst. Growth*. 225 (2001) 516–521. [https://doi.org/10.1016/S0022-0248\(01\)00945-9](https://doi.org/10.1016/S0022-0248(01)00945-9).
- [41] A.A. Wheeler, B.T. Murray, R.J. Schaefer, Computation of dendrites using a phase field model, *Phys. D Nonlinear Phenom.* 66 (1993) 243–262. [https://doi.org/10.1016/0167-2789\(93\)90242-S](https://doi.org/10.1016/0167-2789(93)90242-S).

- [42] A. Karma, W.J. Rappel, Quantitative phase-field modeling of dendritic growth in two and three dimensions, *Phys. Rev. E - Stat. Physics, Plasmas, Fluids, Relat. Interdiscip. Top.* 57 (1998) 4323–4349. <https://doi.org/10.1103/PhysRevE.57.4323>.
- [43] P. Zhao, J.C. Heinrich, Front-tracking finite element method for dendritic solidification, *J. Comput. Phys.* 173 (2001) 765–796. <https://doi.org/10.1006/jcph.2001.6911>.
- [44] K. Reuther, M. Rettenmayr, Perspectives for cellular automata for the simulation of dendritic solidification - A review, *Comput. Mater. Sci.* 95 (2014) 213–220. <https://doi.org/10.1016/j.commatsci.2014.07.037>.
- [45] C. Beckermann, H.J. Diepers, I. Steinbach, A. Karma, X. Tong, Modeling Melt Convection in Phase-Field Simulations of Solidification, *J. Comput. Phys.* 154 (1999) 468–496. <https://doi.org/10.1006/jcph.1999.6323>.
- [46] N. Al-Rawahi, G. Tryggvason, Numerical simulation of dendritic solidification with convection: Two-dimensional geometry, *J. Comput. Phys.* 180 (2002) 471–496. <https://doi.org/10.1006/jcph.2002.7092>.
- [47] D. Chatterjee, S. Chakraborty, A hybrid lattice Boltzmann model for solid-liquid phase transition in presence of fluid flow, *Phys. Lett. Sect. A Gen. At. Solid State Phys.* 351 (2006) 359–367. <https://doi.org/10.1016/j.physleta.2005.11.014>.
- [48] Y. Lu, C. Beckermann, J.C. Ramirez, Three-dimensional phase-field simulations of the effect of convection on free dendritic growth, *J. Cryst. Growth.* 280 (2005) 320–334. <https://doi.org/10.1016/j.jcrysgro.2005.03.063>.
- [49] M. Do-Quang, G. Amberg, Simulation of free dendritic crystal growth in a gravity environment, *J. Comput. Phys.* 227 (2008) 1772–1789. <https://doi.org/10.1016/j.jcp.2007.09.025>.
- [50] T.Y. Hou, J.S. Lowengrub, M.J. Shelley, Boundary Integral Methods for Multicomponent Fluids and Multiphase Materials, *J. Comput. Phys.* 169 (2001) 302–362. <https://doi.org/10.1006/jcph.2000.6626>.
- [51] M. Souli, D.J. Benson, Arbitrary Lagrangian-Eulerian and Fluid-Structure Interaction, 2013. <https://doi.org/10.1002/9781118557884>.
- [52] G. Tryggvason, B. Bunner, A. Esmaeeli, D. Juric, N. Al-Rawahi, W. Tauber, J. Han, S. Nas, Y.J. Jan, A Front-Tracking Method for the Computations of Multiphase Flow, *J. Comput. Phys.* 169 (2001) 708–759. <https://doi.org/10.1006/jcph.2001.6726>.
- [53] M.F. Zhu, D.M. Stefanescu, Virtual front tracking model for the quantitative

- modeling of dendritic growth in solidification of alloys, *Acta Mater.* 55 (2007) 1741–1755. <https://doi.org/10.1016/j.actamat.2006.10.037>.
- [54] E. Uzgoren, J. Sim, W. Shyy, Marker-based, 3-D adaptive cartesian grid method for multiphase flow around irregular geometries, *Commun. Comput. Phys.* 5 (2009) 1–41. <https://doi.org/10.2514/6.2008-1239>.
- [55] M. Muradoglu, S. Tasoglu, A front-tracking method for computational modeling of impact and spreading of viscous droplets on solid walls, *Comput. Fluids.* 39 (2010) 615–625. <https://doi.org/10.1016/j.compfluid.2009.10.009>.
- [56] H. Terashima, G. Tryggvason, A front-tracking method with projected interface conditions for compressible multi-fluid flows, *Comput. Fluids.* 39 (2010) 1804–1814. <https://doi.org/10.1016/j.compfluid.2010.06.012>.
- [57] D. She, R. Kaufman, H. Lim, J. Melvin, A. Hsu, J. Glimm, *Front-Tracking Methods*, in: *Handb. Numer. Anal.*, 2016: pp. 383–402. <https://doi.org/10.1016/bs.hna.2016.07.004>.
- [58] R. Scardovelli, S. Zaleski, Direct numerical simulation of free-surface and interfacial flow, *Annu. Rev. Fluid Mech.* 31 (1999) 567–603. <https://doi.org/10.1146/annurev.fluid.31.1.567>.
- [59] B.G.M. van Wachem, A.E. Almstedt, Methods for multiphase computational fluid dynamics, *Chem. Eng. J.* 96 (2003) 81–98. <https://doi.org/10.1016/j.cej.2003.08.025>.
- [60] M. Wörner, Numerical modeling of multiphase flows in microfluidics and micro process engineering: A review of methods and applications, *Microfluid. Nanofluidics.* 12 (2012) 841–886. <https://doi.org/10.1007/s10404-012-0940-8>.
- [61] K. Connington, T. Lee, A review of spurious currents in the lattice Boltzmann method for multiphase flows, *J. Mech. Sci. Technol.* 26 (2012) 3857–3863. <https://doi.org/10.1007/s12206-012-1011-5>.
- [62] J.J. Huang, C. Shu, J.J. Feng, Y.T. Chew, A phase-field-based hybrid lattice-boltzmann finite-volume method and its application to simulate droplet motion under electrowetting control, *J. Adhes. Sci. Technol.* 26 (2012) 1825–1851. <https://doi.org/10.1163/156856111X599607>.
- [63] M. Eshraghi, B. Jelinek, S.D. Felicelli, Large-Scale Three-Dimensional Simulation of Dendritic Solidification Using Lattice Boltzmann Method, *Jom.* 67 (2015) 1786–1792. <https://doi.org/10.1007/s11837-015-1446-0>.
- [64] X. Shan, H. Chen, Lattice Boltzmann model for simulating flows with multiple phases and components, *Phys. Rev. E.* 47 (1993) 1815–1819.

<https://doi.org/10.1103/PhysRevE.47.1815>.

- [65] M.R. Swift, E. Orlandini, W.R. Osborn, J.M. Yeomans, Lattice Boltzmann simulations of liquid-gas and binary fluid systems, *Phys. Rev. E - Stat. Physics, Plasmas, Fluids, Relat. Interdiscip. Top.* 54 (1996) 5041–5052. <https://doi.org/10.1103/PhysRevE.54.5041>.
- [66] T. Inamuro, T. Ogata, S. Tajima, N. Konishi, A lattice Boltzmann method for incompressible two-phase flows with large density differences, *J. Comput. Phys.* 198 (2004) 628–644. <https://doi.org/10.1016/j.jcp.2004.01.019>.
- [67] X. He, S. Chen, R. Zhang, A Lattice Boltzmann Scheme for Incompressible Multiphase Flow and Its Application in Simulation of Rayleigh-Taylor Instability, *J. Comput. Phys.* 152 (1999) 642–663. <https://doi.org/10.1006/jcph.1999.6257>.
- [68] T. Lee, L. Liu, Lattice Boltzmann simulations of micron-scale drop impact on dry surfaces, *J. Comput. Phys.* 229 (2010) 8045–8063. <https://doi.org/10.1016/j.jcp.2010.07.007>.
- [69] H. Huang, M.C. Sukop, X.Y. Lu, *Multiphase Lattice Boltzmann Methods: Theory and Application*, 2015. <https://doi.org/10.1002/9781118971451>.
- [70] T. Lee, C.L. Lin, A stable discretization of the lattice Boltzmann equation for simulation of incompressible two-phase flows at high density ratio, *J. Comput. Phys.* 206 (2005) 16–47. <https://doi.org/10.1016/j.jcp.2004.12.001>.
- [71] H. Huang, J.J. Huang, X.Y. Lu, A mass-conserving axisymmetric multiphase lattice Boltzmann method and its application in simulation of bubble rising, *J. Comput. Phys.* 269 (2014) 386–402. <https://doi.org/10.1016/j.jcp.2014.03.028>.
- [72] J.Y. Shao, C. Shu, A hybrid phase field multiple relaxation time lattice Boltzmann method for the incompressible multiphase flow with large density contrast, *Int. J. Numer. Methods Fluids.* 77 (2015) 526–543. <https://doi.org/10.1002/flid.3995>.
- [73] H. Liu, Y. Zhang, A.J. Valocchi, Modeling and simulation of thermocapillary flows using lattice Boltzmann method, *J. Comput. Phys.* 231 (2012) 4433–4453. <https://doi.org/10.1016/j.jcp.2012.02.015>.
- [74] H. Liu, A.J. Valocchi, Y. Zhang, Q. Kang, Lattice Boltzmann phase-field modeling of thermocapillary flows in a confined microchannel, *J. Comput. Phys.* 256 (2014) 334–356. <https://doi.org/10.1016/j.jcp.2013.08.054>.
- [75] H. Safari, M.H. Rahimian, M. Krafczyk, Consistent simulation of droplet evaporation based on the phase-field multiphase lattice Boltzmann method, *Phys. Rev. E - Stat. Nonlinear, Soft Matter Phys.* 90 (2014). <https://doi.org/10.1103/PhysRevE.90.033305>.

- [76] J.Y. Shao, C. Shu, H.B. Huang, Y.T. Chew, Free-energy-based lattice Boltzmann model for the simulation of multiphase flows with density contrast, *Phys. Rev. E - Stat. Nonlinear, Soft Matter Phys.* 89 (2014) 1–14.
<https://doi.org/10.1103/PhysRevE.89.033309>.
- [77] A. Tiribocchi, N. Stella, G. Gonnella, A. Lamura, Hybrid lattice Boltzmann model for binary fluid mixtures, *Phys. Rev. E - Stat. Nonlinear, Soft Matter Phys.* 80 (2009). <https://doi.org/10.1103/PhysRevE.80.026701>.
- [78] S. Gottlieb, J.S. Mullen, S.J. Ruuth, A fifth order flux implicit WENO method, *J. Sci. Comput.* 27 (2006) 271–287. <https://doi.org/10.1007/s10915-005-9034-z>.
- [79] W. Wu, M.F. Zhu, D.K. Sun, T. Dai, Q.Y. Han, D. Raabe, Modelling of dendritic growth and bubble formation, in: *IOP Conf. Ser. Mater. Sci. Eng.*, 2012.
<https://doi.org/10.1088/1757-899X/33/1/012103>.
- [80] D. Sun, M. Zhu, J. Wang, B. Sun, Lattice Boltzmann modeling of bubble formation and dendritic growth in solidification of binary alloys, *Int. J. Heat Mass Transf.* 94 (2016) 474–487.
<https://doi.org/10.1016/j.ijheatmasstransfer.2015.11.079>.
- [81] L. Chen, Q. Kang, Y. Mu, Y.L. He, W.Q. Tao, A critical review of the pseudopotential multiphase lattice Boltzmann model: Methods and applications, *Int. J. Heat Mass Transf.* 76 (2014) 210–236.
<https://doi.org/10.1016/j.ijheatmasstransfer.2014.04.032>.
- [82] M. Ghods, M. Lauer, S.R. Upadhyay, R.N. Grugel, S.N. Tewari, D.R. Poirier, Spurious Grain Formation at Cross-Sectional Expansion During Directional Solidification: Influence of Thermosolutal Convection, *J. Mater. Eng. Perform.* 27 (2018) 3122–3130. <https://doi.org/10.1007/s11665-018-3364-0>.
- [83] S.A. Nabavizadeh, M. Eshraghi, S.D. Felicelli, S.N. Tewari, R.N. Grugel, The Marangoni convection effects on directional dendritic solidification, *Heat Mass Transf. Und Stoffuebertragung.* 56 (2020) 1329–1341.
<https://doi.org/10.1007/s00231-019-02799-4>.
- [84] Q. Li, C. Beckermann, Modeling of free dendritic growth of succinonitrile-acetone alloys with thermosolutal melt convection, *J. Cryst. Growth.* 236 (2002) 482–498.
[https://doi.org/10.1016/S0022-0248\(01\)02390-9](https://doi.org/10.1016/S0022-0248(01)02390-9).
- [85] S.A. Nabavizadeh, R. Lenart, M. Eshraghi, S.D. Felicelli, S.N. Tewari, R.N. Grugel, Dendritic solidification of Succinonitrile-0.24 wt% water alloy: A comparison with microgravity experiments for validating dendrite tip velocity, *Acta Astronaut.* 175 (2020) 163–173.
<https://doi.org/10.1016/j.actaastro.2020.05.059>.

- [86] L.L. Strutzenberg, R.N. Grugel, R. Trivedi, Morphological evolution of directional solidification interfaces in microgravity: An analysis of model experiments performed on the international space station, in: 43rd AIAA Aerosp. Sci. Meet. Exhib. - Meet. Pap., 2005: pp. 9137–9142. <https://doi.org/10.2514/6.2005-917>.
- [87] S. Angart, M. Lauer, S.N. Tewari, R.N. Grugel, D.R. Poirier, Comparison of directionally solidified samples solidified terrestrially and aboard the international space station, Proc. 61st Annu. Tech. Conf. Invest. Cast. Inst. (2014).
- [88] M. Lauer, M. Ghods, S.G. Angart, R.N. Grugel, S.N. Tewari, D.R. Poirier, Macroseggregation During Re-melting and Holding of Directionally Solidified Al-7 wt.% Si Alloy in Microgravity, Jom. 69 (2017) 1289–1297. <https://doi.org/10.1007/s11837-017-2380-0>.
- [89] M. Ghods, S.R. Upadhyay, R.S. Rajamure, S.N. Tewari, R.N. Grugel, D.R. Poirier, M. Lauer, Primary dendrite array morphology in Al-7 wt% Si alloy samples directionally solidified aboard the International Space Station, J. Cryst. Growth. 562 (2021) 126077. <https://doi.org/10.1016/j.jcrysgro.2021.126077>.
- [90] M. Ghods, L. Johnson, M. Lauer, R.N. Grugel, S.N. Tewari, D.R. Poirier, Radial macroseggregation and dendrite clustering in directionally solidified Al-7Si and Al-19Cu alloys, J. Cryst. Growth. 441 (2016) 107–116. <https://doi.org/10.1016/j.jcrysgro.2016.02.014>.
- [91] L. Ratke, S. Steinbach, G. Müller, M. Hainke, A. Roosz, Y. Fautrelle, M.D. Dupouy, G. Zimmermann, A. Weiss, H.J. Diepers, J. Lacaze, R. Valdes, G.U. Grün, H.P. Nicolai, H. Gerke-Cantow, MICAST - Microstructure formation in casting of technical alloys under diffusive and magnetically controlled convective conditions, in: Mater. Sci. Forum, 2006: pp. 131–144. <https://doi.org/10.4028/0-87849-991-1.131>.
- [92] S.A. Nabavizadeh, S. Upadhyay, M. Eshraghi, S.D. Felicelli, S.N. Tewari, R.N. Grugel, Spurious grain formation due to Marangoni convection during directional solidification of alloys in μ -g environment of International Space Station, J. Cryst. Growth. 574 (2021) 126334. <https://doi.org/10.1016/j.jcrysgro.2021.126334>.
- [93] M.N. Özişik, Finite Difference Methods in Heat Transfer, CRC press, 2017. <https://doi.org/10.1201/9781315168784>.
- [94] P.L. Bhatnagar, E.P. Gross, M. Krook, A model for collision processes in gases. I. Small amplitude processes in charged and neutral one-component systems, Phys. Rev. 94 (1954) 511–525. <https://doi.org/10.1103/PhysRev.94.511>.
- [95] L. Luo, Lattice-gas automata and lattice Boltzmann equations for two-dimensional hydrodynamics, (1993) 183. <http://adsabs.harvard.edu/abs/1993PhDT.....233L> (accessed March 25, 2019).

- [96] U. Frisch, B. Hasslacher, Y. Pomeau, Lattice-gas automata for the Navier-Stokes equation, *Phys. Rev. Lett.* 56 (1986) 1505–1508.
<https://doi.org/10.1103/PhysRevLett.56.1505>.
- [97] V.C.A. Ferraro, S. Chapman, T.G. Cowling, *The Mathematical Theory of Non-Uniform Gases. An Account of the Kinetic Theory of Viscosity, Thermal Conduction, and Diffusion in Gases*, *Math. Gaz.* 38 (1954) 63.
<https://doi.org/10.2307/3609795>.
- [98] M.C. Sukop, D.T. Thorne, *Lattice Boltzmann modeling: An introduction for geoscientists and engineers*, 2006. <https://doi.org/10.1007/978-3-540-27982-2>.
- [99] R. Benzi, L. Biferale, M. Sbragaglia, S. Succi, F. Toschi, Mesoscopic modeling of a two-phase flow in the presence of boundaries: The contact angle, *Phys. Rev. E - Stat. Nonlinear, Soft Matter Phys.* 74 (2006).
<https://doi.org/10.1103/PhysRevE.74.021509>.
- [100] P. Yuan, L. Schaefer, Equations of state in a lattice Boltzmann model, *Phys. Fluids.* 18 (2006). <https://doi.org/10.1063/1.2187070>.
- [101] X. Shan, Analysis and reduction of the spurious current in a class of multiphase lattice Boltzmann models, *Phys. Rev. E - Stat. Nonlinear, Soft Matter Phys.* 73 (2006). <https://doi.org/10.1103/PhysRevE.73.047701>.
- [102] S. Chibbaro, G. Falcucci, G. Chiatti, H. Chen, X. Shan, S. Succi, Lattice Boltzmann models for nonideal fluids with arrested phase-separation, *Phys. Rev. E - Stat. Nonlinear, Soft Matter Phys.* 77 (2008).
<https://doi.org/10.1103/PhysRevE.77.036705>.
- [103] L. Zheng, S. Zheng, Q. Zhai, Continuous surface force based lattice Boltzmann equation method for simulating thermocapillary flow, *Phys. Lett. Sect. A Gen. At. Solid State Phys.* 380 (2016) 596–603.
<https://doi.org/10.1016/j.physleta.2015.11.033>.
- [104] H. Yin, S.D. Felicelli, L. Wang, Simulation of a dendritic microstructure with the lattice Boltzmann and cellular automaton methods, *Acta Mater.* 59 (2011) 3124–3136. <https://doi.org/10.1016/j.actamat.2011.01.052>.
- [105] M. Eshraghi, S.D. Felicelli, B. Jelinek, Three dimensional simulation of solutal dendrite growth using lattice Boltzmann and cellular automaton methods, *J. Cryst. Growth.* 354 (2012) 129–134. <https://doi.org/10.1016/j.jcrysgro.2012.06.002>.
- [106] B. Jelinek, M. Eshraghi, S. Felicelli, J.F. Peters, Large-scale parallel lattice Boltzmann-cellular automaton model of two-dimensional dendritic growth, *Comput. Phys. Commun.* 185 (2014) 939–947.
<https://doi.org/10.1016/j.cpc.2013.09.013>.

- [107] J.E. Taylor, II-mean curvature and weighted mean curvature, *Acta Metall. Mater.* 40 (1992) 1475–1485. [https://doi.org/10.1016/0956-7151\(92\)90091-R](https://doi.org/10.1016/0956-7151(92)90091-R).
- [108] S. Pan, M. Zhu, A three-dimensional sharp interface model for the quantitative simulation of solutal dendritic growth, *Acta Mater.* 58 (2010) 340–352. <https://doi.org/10.1016/j.actamat.2009.09.012>.
- [109] B. Echebarria, R. Folch, A. Karma, M. Plapp, Quantitative phase-field model of alloy solidification, *Phys. Rev. E - Stat. Physics, Plasmas, Fluids, Relat. Interdiscip. Top.* 70 (2004) 22. <https://doi.org/10.1103/PhysRevE.70.061604>.
- [110] A. Rai, M. Markl, C. Körner, A coupled Cellular Automaton–Lattice Boltzmann model for grain structure simulation during additive manufacturing, *Comput. Mater. Sci.* 124 (2016) 37–48. <https://doi.org/10.1016/j.commatsci.2016.07.005>.
- [111] A.G. Yiotis, J. Psihogios, M.E. Kainourgiakis, A. Papaioannou, A.K. Stubos, A lattice Boltzmann study of viscous coupling effects in immiscible two-phase flow in porous media, *Colloids Surfaces A Physicochem. Eng. Asp.* 300 (2007) 35–49. <https://doi.org/10.1016/j.colsurfa.2006.12.045>.
- [112] R. Borcia, I.D. Borcia, M. Bestehorn, Drops on an arbitrarily wetting substrate: A phase field description, *Phys. Rev. E - Stat. Nonlinear, Soft Matter Phys.* 78 (2008) 1–6. <https://doi.org/10.1103/PhysRevE.78.066307>.
- [113] R. Borcia, I.D. Borcia, M. Bestehorn, Static and dynamic contact angles - A phase field modelling, *Eur. Phys. J. Spec. Top.* 166 (2009) 127–131. <https://doi.org/10.1140/epjst/e2009-00892-0>.
- [114] S. Schmieschek, J. Harting, Contact angle determination in multicomponent lattice Boltzmann simulations, *Commun. Comput. Phys.* 9 (2011) 1165–1178. <https://doi.org/10.4208/cicp.201009.271010s>.
- [115] H. Liu, A.J. Valocchi, Y. Zhang, Q. Kang, Phase-field-based lattice Boltzmann finite-difference model for simulating thermocapillary flows, *Phys. Rev. E - Stat. Nonlinear, Soft Matter Phys.* 87 (2013) 13010. <https://doi.org/10.1103/PhysRevE.87.013010>.
- [116] M. Herrmann, J. Lopez, P. Brady, M. Raessi, Thermocapillary motion of deformable drops and bubbles, *Proc. Summer Progr.* (2008) 155–170. http://citeseerx.ist.psu.edu/viewdoc/download?doi=10.1.1.169.9854&rep=rep1&type=pdf%5Cnhttp://www.stanford.edu/group/ctr/Summer/SP08/3_2_Lopez.pdf.
- [117] Z. Guo, P. Lin, A thermodynamically consistent phase-field model for two-phase flows with thermocapillary effects, *J. Fluid Mech.* 766 (2015) 226–271. <https://doi.org/10.1017/jfm.2014.696>.

- [118] J. Lipton, M.E. Glicksman, W. Kurz, Dendritic growth into undercooled alloy metals, *Mater. Sci. Eng.* 65 (1984) 57–63. [https://doi.org/10.1016/0025-5416\(84\)90199-X](https://doi.org/10.1016/0025-5416(84)90199-X).
- [119] J. Lipton, M.E. Glicksman, W. Kurz, Equiaxed dendrite growth in alloys at small supercooling, *Metall. Trans. A.* 18 (1987) 341–345. <https://doi.org/10.1007/BF02825716>.
- [120] M. Rappaz, C.A. Gandin, Probabilistic modelling of microstructure formation in solidification processes, *Acta Metall. Mater.* 41 (1993) 345–360. [https://doi.org/10.1016/0956-7151\(93\)90065-Z](https://doi.org/10.1016/0956-7151(93)90065-Z).
- [121] M. Eshraghi, M. Hashemi, B. Jelinek, S.D. Felicelli, Three-dimensional lattice Boltzmann modeling of dendritic solidification under forced and natural convection, *Metals (Basel)*. 7 (2017) 474. <https://doi.org/10.3390/met7110474>.
- [122] S.A. Nabavizadeh, M. Eshraghi, S.D. Felicelli, A comparative study of multiphase lattice Boltzmann methods for bubble-dendrite interaction during solidification of alloys, *Appl. Sci.* 9 (2018) 57. <https://doi.org/10.3390/app9010057>.
- [123] P.S. Wei, C.C. Huang, Z.P. Wang, K.Y. Chen, C.H. Lin, Growths of bubble/pore sizes in solid during solidification - An in situ measurement and analysis, *J. Cryst. Growth.* 270 (2004) 662–673. <https://doi.org/10.1016/j.jcrysgro.2004.06.039>.
- [124] L. Arnberg, R.H. Mathiesen, The real-time, high-resolution X-ray video microscopy of solidification in aluminum alloys, *Jom.* 59 (2007) 20–26. <https://doi.org/10.1007/s11837-007-0099-z>.
- [125] P. Yue, C. Zhou, J.J. Feng, Spontaneous shrinkage of drops and mass conservation in phase-field simulations, *J. Comput. Phys.* 223 (2007) 1–9. <https://doi.org/10.1016/j.jcp.2006.11.020>.
- [126] R. Rojas, T. Takaki, M. Ohno, A phase-field-lattice Boltzmann method for modeling motion and growth of a dendrite for binary alloy solidification in the presence of melt convection, *J. Comput. Phys.* 298 (2015) 29–40. <https://doi.org/10.1016/j.jcp.2015.05.045>.
- [127] S.A. Nabavizadeh, M. Eshraghi, S.D. Felicelli, S.N. Tewari, R.N. Grugel, Effect of bubble-induced Marangoni convection on dendritic solidification, *Int. J. Multiph. Flow.* 116 (2019) 137–152. <https://doi.org/10.1016/j.ijmultiphaseflow.2019.04.018>.
- [128] M.V.A. Bianchi, R. Viskanta, Gas segregation during solidification processes, *Int. J. Heat Mass Transf.* 40 (1997) 2035–2043. [https://doi.org/10.1016/S0017-9310\(96\)00283-9](https://doi.org/10.1016/S0017-9310(96)00283-9).

- [129] M. Kassemi, S. Barsi, J.I.D. Alexander, M. Banish, Contamination of microgravity liquid diffusivity measurements by void-generated thermocapillary convection, *J. Cryst. Growth*. 276 (2005) 621–634.
<https://doi.org/10.1016/j.jcrysgro.2004.11.426>.
- [130] G. Hansen, S. Liu, S.Z. Lu, A. Hellawell, Dendritic array growth in the systems NH₄Cl-H₂O and [CH₂CN]₂-H₂O: Steady state measurements and analysis, *J. Cryst. Growth*. 234 (2002) 731–739. [https://doi.org/10.1016/S0022-0248\(01\)01679-7](https://doi.org/10.1016/S0022-0248(01)01679-7).
- [131] A.B. COMSOL, Comsol multiphysics reference manual, version 5.0, COMSOL AB. (2018).
- [132] M. Kassemi, M. Kaforey, D. Matthiesen, Effect of Void-Generated Thermocapillary Convection on Dopant Segregation in Microgravity Solidification, *J. Thermophys. Heat Transf.* 15 (2001) 219–227.
<https://doi.org/10.2514/2.6597>.
- [133] S. Akamatsu, G. Faivre, Residual-Impurity Effects in Directional Solidification: Long-Lasting Recoil of the Front and Nucleation-Growth of Gas Bubbles, *J. Phys. I*. 6 (1996) 503–527. <https://doi.org/10.1051/JP1:1996227>.
- [134] J.D. Hunt, Steady state columnar and equiaxed growth of dendrites and eutectic, *Mater. Sci. Eng.* 65 (1984) 75–83. [https://doi.org/10.1016/0025-5416\(84\)90201-5](https://doi.org/10.1016/0025-5416(84)90201-5).
- [135] M. Gäumann, C. Bezençon, P. Canalis, W. Kurz, Single-crystal laser deposition of superalloys: Processing-microstructure maps, *Acta Mater.* 49 (2001) 1051–1062.
[https://doi.org/10.1016/S1359-6454\(00\)00367-0](https://doi.org/10.1016/S1359-6454(00)00367-0).
- [136] G.L. Knapp, N. Raghavan, A. Plotkowski, T. DebRoy, Experiments and simulations on solidification microstructure for Inconel 718 in powder bed fusion electron beam additive manufacturing, *Addit. Manuf.* 25 (2019) 511–521.
<https://doi.org/10.1016/j.addma.2018.12.001>.
- [137] M. Lamm, R.F. Singer, The effect of casting conditions on the high-cycle fatigue properties of the single-crystal nickel-base superalloy PWA 1483, *Metall. Mater. Trans. A Phys. Metall. Mater. Sci.* 38 (2007) 1177–1183.
<https://doi.org/10.1007/s11661-007-9188-4>.
- [138] B.C. Wilson, E.R. Cutler, G.E. Fuchs, Effect of solidification parameters on the microstructures and properties of CMSX-10, *Mater. Sci. Eng. A*. 479 (2008) 356–364. <https://doi.org/10.1016/j.msea.2007.07.030>.
- [139] S. Gurevich, A. Karma, M. Plapp, R. Trivedi, Phase-field study of three-dimensional steady-state growth shapes in directional solidification, *Phys. Rev. E - Stat. Nonlinear, Soft Matter Phys.* 81 (2010).

<https://doi.org/10.1103/PhysRevE.81.011603>.

- [140] W. Huang, M. Wang, Progress and development trends in the numerical modeling of solidification, *Chinese Sci. Bull.* 59 (2014) 1709–1718.
<https://doi.org/10.1007/s11434-013-0092-6>.
- [141] H. Weidong, G. Xingguo, Z. Yaohe, Primary spacing selection of constrained dendritic growth, *J. Cryst. Growth.* 134 (1993) 105–115.
[https://doi.org/10.1016/0022-0248\(93\)90015-O](https://doi.org/10.1016/0022-0248(93)90015-O).
- [142] L. Nastac, J.J. Valencia, M.L. Tims, F.R. Dax, Advances in the solidification of IN718 and RS5 alloys, in: *Proc. Int. Symp. Superalloys Var. Deriv.*, 2001: pp. 103–112. https://doi.org/10.7449/2001/superalloys_2001_103_112.
- [143] W. Kurz, D.J. Fisher, Dendrite growth at the limit of stability: tip radius and spacing, *Acta Metall.* 29 (1981) 11–20. [https://doi.org/10.1016/0001-6160\(81\)90082-1](https://doi.org/10.1016/0001-6160(81)90082-1).
- [144] R. TRIVEDI, Interdendritic Spacing: Part II. A Comparison of Theory and Experiment, in: *Dyn. Curved Front.*, 1988: pp. 353–358.
<https://doi.org/10.1016/b978-0-08-092523-3.50038-1>.
- [145] L. Nastac, D.M. Stefanescu, Stochastic modelling of microstructure formation in solidification processes, *Model. Simul. Mater. Sci. Eng.* 5 (1997) 391–420.
<https://doi.org/10.1088/0965-0393/5/4/008>.
- [146] L. Nastac, Numerical modeling of solidification morphologies and segregation patterns in cast dendritic alloys, *Acta Mater.* 47 (1999) 4253–4262.
[https://doi.org/10.1016/S1359-6454\(99\)00325-0](https://doi.org/10.1016/S1359-6454(99)00325-0).
- [147] S.A. Nabavizadeh, M. Eshraghi, S.D. Felicelli, Three-dimensional phase field modeling of columnar to equiaxed transition in directional solidification of Inconel 718 alloy, *J. Cryst. Growth.* 549 (2020) 125879.
<https://doi.org/10.1016/j.jcrysgr.2020.125879>.
- [148] F. Bachmann, R. Hielscher, H. Schaeben, Texture analysis with MTEX- Free and open source software toolbox, in: *Solid State Phenom.*, 2010: pp. 63–68.
<https://doi.org/10.4028/www.scientific.net/SSP.160.63>.
- [149] P. Nie, O.A. Ojo, Z. Li, Numerical modeling of microstructure evolution during laser additive manufacturing of a nickel-based superalloy, *Acta Mater.* 77 (2014) 85–95. <https://doi.org/10.1016/j.actamat.2014.05.039>.
- [150] X. Wang, P.W. Liu, Y. Ji, Y. Liu, M.H. Horstemeyer, L. Chen, Investigation on Microsegregation of IN718 Alloy During Additive Manufacturing via Integrated Phase-Field and Finite-Element Modeling, *J. Mater. Eng. Perform.* 28 (2019) 657–

665. <https://doi.org/10.1007/s11665-018-3620-3>.

- [151] G. Boussinot, M. Apel, J. Zielinski, U. Hecht, J.H. Schleifenbaum, Strongly Out-of-Equilibrium Columnar Solidification during Laser Powder-Bed Fusion in Additive Manufacturing, *Phys. Rev. Appl.* 11 (2019). <https://doi.org/10.1103/PhysRevApplied.11.014025>.
- [152] R. Lenart, M. Eshraghi, Modeling columnar to equiaxed transition in directional solidification of Inconel 718 alloy, *Comput. Mater. Sci.* 172 (2020) 109374. <https://doi.org/10.1016/j.commatsci.2019.109374>.
- [153] S.A. Nabavizadeh, H. Barua, M. Eshraghi, S.D. Felicelli, A multiple-grid lattice boltzmann method for natural convection under low and high prandtl numbers, *Fluids.* 6 (2021) 1–20. <https://doi.org/10.3390/FLUIDS6040148>.